Investigating self-mode-locking in VECSELs: Nonlinear lensing and frequency-modulated combs

Dissertation

zur
Erlangung des Doktorgrades
der Naturwissenschaften
(Dr. rer. nat.)

dem
Fachbereich Physik
der Philipps-Universität Marburg

vorgelegt von

Christian David Kriso

aus

Stuttgart

Marburg, 2021

Vom Fachbereich Physik der Philipps-Universität Marburg
als Dissertation angenommen am: 11.08.2021

Erstgutachter: Prof. Dr. Martin Koch
Zweitgutachter: Prof. Dr. Wolfgang Stolz

Tag der mündlichen Prüfung: 03.09.2021
Hochschulkennziffer: 1180

He has made everything beautiful in its time. He has also set eternity in the human heart; yet no one can fathom what God has done from beginning to end.

Ecclesiastes 3,11

Kurzfassung

Optisch gepumpte Halbleiterscheibenlaser, im Englischen als „vertical-external-cavity surface-emitting lasers“ oder VECSELs bezeichnet, zeichnen sich durch eine hohe Ausgangsleistung, exzellente Strahlqualität sowie eine Vielzahl von verfügbaren Emissionswellenlängen aus, die durch den Einsatz der modernen Halbleiterepitaxie ermöglicht werden [1, 2]. Dabei können diese Laser nicht nur im Dauerstrichbetrieb betrieben werden, sondern auch ultrakurze Pulse in der Größenordnung von einigen hundert Femtosekunden erzeugen. Dies wird als Modenkopplung bezeichnet, da dabei die longitudinalen Lasermoden über ein nichtlineares optisches Bauelement miteinander koppeln und so phasenstabil zueinander sind. Normalerweise ist dieses nichtlineare optische Bauelement ein sogenannter SESAM (englische Abkürzung für „semiconductor saturable absorber mirror“), der ähnlich wie der VECSEL Chip aus einem oder mehreren Quantentöpfen oder Lagen von Quantenpunkten und einen integrierten Bragg-Spiegel besteht, aber nicht optisch gepumpt wird. Durch die dadurch in die Laserkavität integrierte sättigbare Absorption erfahren kurze Pulse mit hohe Spitzenleistungen weniger Verlust als der Dauerstrichbetrieb was den gepulsten Betrieb begünstigt. Solche gepulsten Laser sind für eine Vielzahl von Anwendungen wie beispielsweise die Zweiphotonenmikroskopie oder die Frequenzkammspektroskopie interessant [3–5].

Neben der Pulserzeugung mit SESAMs wurden in den letzten Jahren von mehreren Gruppen auch spontane Pulsemission aus VECSELn beobachtet [6–10]. Dieses Phänomen wird Selbstmodenkopplung genannt. Bis heute ist jedoch umstritten, was die Ursache dahinter ist und ob es dabei wirklich zu einem stabilen modengekoppelten Zustand kommt [11, 12]. Eine vermutete Ursache der Selbstmodenkopplung ist, dass der intrinische nichtlineare Brechungsindex des VECSEL Chips zur Selbst(de-)fokussierung des intrakavitären Strahlprofils führt. Mit dem Einführen eines Spaltes in der Kavität oder des Verringerns der Pumpspotgröße auf dem Chip könnten so die Verluste im gepulsten Betrieb minimiert werden wie es auch bei der Kerr-Linsen Modenkopplung in Festkörperlasern der Fall ist. Im Gegensatz zu diesen hängt die nichtlineare Linse im VECSEL Chip allerdings im Allgemeinen sowohl von der optischen Anregung als auch von der Pulslänge ab. Deswegen befasst sich ein Teil dieser Arbeit mit der experimentellen Untersuchung des nichtlinearen Brechungsindex von VECSEL Chips in Abhängigkeit der Wellenlänge, der Anregungsdichte und der Pulslänge. Dabei werden die Messmethoden Z-scan und die ultraschnelle Strahlablenkung (engl. „beam deflection“) angewandt. Aus den Messungen wird ein nichtlinearer Brechungsindex in der Größenordnung von -10^{-16} m^2/W für Laserpulse kürzer als eine Pikosekunde bestimmt [13–15]. Für lange Pulslängen von einigen Pikosekunden und großen Anregungsdichten wird der nichtlineare Brechungsindex positiv und sein Wert nimmt stark zu ($\sim +10^{-15}$ m^2/W). Diese Messungen bestätigen einige Berichte von Selbstmodenkopplung in VECSELn bei denen aus der Kavitätsgeometrie das Vorzeichen und

die Größenordnung des nichtlinearen Brechungsindex abgeschätzt werden kann [8, 15, 16]. Dabei wird angenommen, dass für eine effiziente Kerr-Linsen Modenkopplung eine Veränderung der intrakavitären Strahlweite von einigen Prozent benötigt wird.

Weiterhin wird in dieser Arbeit die Möglichkeit untersucht, ob VECSEL sogenannte frequenzmodulierte Kämme erzeugen können. Dabei handelt es sich um eine spezielle Art der Modenkopplung, bei der die Lasermoden zwar gekoppelt sind, aber die Phasenbeziehung zwischen benachbarten Moden nicht annähernd null ist, sondern sich zwischen 0 und 2π über das Laserspektrum verteilt [17]. Das führt dazu, dass die emittierte Laserleistung quasi zeitlich konstant ist, aber die Frequenz periodisch mit der Zeit variiert. Diese Art von Modenkopplung wird durch resonante Vierwellenmischprozesse im Halbleiterlasermedium erzeugt und ist insbesondere bei Quantenkaskaden- und Diodenlasern ein fundamentaler Betriebszustand, der für Anwendungen wie die Zweikammspektroskopie genutzt werden kann [17–19]. Mittels der neuartigen Messmethode SWIFTS (engl. „shifted-wave-interference Fourier-transform spectroscopy“) kann dabei direkt die Phasenbeziehung zwischen benachbarten Moden gemessen und ein Maß für die Phasenstabilität erhalten werden [20]. Durch Einsatz von SWIFTS wird in dieser Arbeit gezeigt, dass auch VECSEL in einem frequenzmodulierten Kammzustand laufen können [21]. Das ist durchaus überraschend, da Elemente wie starkes räumliches Lochbrennen und große Auskoppelverluste wie sie für kantenemittierende Dioden- und Quantenkaskadenlaser typisch sind, und als wichtig für frequenzmodulierte Kammerzeugung angesehen worden sind, hier wegfallen [22, 23]. Jedoch zeigt es wie universell der Zustand des frequenzmodulierten Kammes in Halbleiterlasern ist und kann als Anreiz dienen dieses Phänomen auch von der theoretischen Seite her noch besser zu verstehen.

Abstract

Optically pumped semiconductor disk lasers, also known as vertical-external-cavity surface-emitting lasers (VECSELs), stand out by their high output power, excellent beam quality and a multitude of available emission wavelengths that can be obtained by advanced semiconductor epitaxy [1, 2]. Apart from running in continuous-wave operation, these lasers can also generate pulses with durations of only a few hundreds of femtoseconds. This is called mode-locking because the laser modes are coupled to each other by a nonlinear optical element and therefore become phase-stable. Usually, this intracavity element is a semiconductor saturable absorber mirror (SESAM), which, similar to a VECSEL, consists of one or more quantum wells, or quantum dot layers, and a distributed Bragg reflector (DBR), but is not optically pumped. Therefore, due to the added saturable absorption in the cavity, short pulses with high peak power experience less loss than continuous-wave operation which favors pulsed operation. Such kind of pulsed lasers are useful for many applications such as two-photon microscopy or frequency-comb spectroscopy [3–5].

Besides ultrashort-pulse generation with SESAMs, also spontaneous pulse emission from VECSELs was observed by several groups in the last years [6–10]. This phenomenon is called self-mode-locking. Up to now, it is controversial, what the origin of this phenomenon is and whether it really leads to a stably mode-locked state [11, 12]. One possible cause of self-mode-locking might be that the intrinsic nonlinear refractive index of the VECSEL chip leads to self(de-)focusing of the intracavity beam. By inserting a slit into the cavity or reducing the pump spot size on the chip, the losses in pulsed operation might be reduced as is the case for Kerr-lens mode-locking of solid-state lasers. However, in contrast to solid-state lasers, the nonlinear lens in a VECSEL chip generally depends on the optical excitation as well as the pulse length. Therefore, one part of this work deals with the experimental investigation of the nonlinear refractive index of VECSEL chips as a function of the wavelength, the excitation fluence and the pulse length. For this purpose, the measurement methods Z-scan and ultrafast beam deflection are used. A nonlinear refractive index in the order of magnitude of -10^{-16} m^2/W is obtained for laser pulses shorter than one picosecond [13–15]. For long pulse lengths of a few picoseconds and large excitation fluences, the nonlinear refractive index becomes positive and increases strongly in magnitude ($\sim +10^{-15}$ m^2/W). These measurements confirm some reports of self-mode-locking where the sign and the magnitude of the nonlinear refractive index can be estimated from the cavity geometry [8, 15, 16]. There, it is assumed that for efficient Kerr-lens mode-locking an intracavity beam width modulation of a few percents is required.

Furthermore, this thesis investigates whether so-called frequency-modulated combs can be generated by VECSELs. Thereby, the laser modes are locked. However, the phase relations between adjacent modes are not approximately zero but vary between 0 and

2π [17]. This leads to a situation where the emitted laser power is temporally nearly constant but the frequency varies periodically. Such kind of mode-locking is generated by resonant four-wave mixing processes in the semiconductor gain medium. Particularly for quantum cascade and diode lasers, it is a fundamental operation regime that can be used for applications such as dual comb spectroscopy [17–19]. With a novel measurement technique called shifted-wave-interference Fourier-transform spectroscopy (SWIFTS), the intermode phases can directly be measured and the phase stability can be assessed [20]. In this thesis, it is demonstrated by using SWIFTS that also VECSELs can run in a frequency-modulated comb state [21]. This is quite surprising as elements such as spatial hole burning and large outcoupling losses, that are characteristic for edge-emitting diode and quantum cascade lasers, and have been considered to be important for frequency-modulated comb generation, are lacking in VECSELs [22, 23]. However, it shows how universal the phenomenon of frequency-modulated combs is and it can serve as motivation to understand it also better from the theoretical side.

List of publications

Relevant publications (appended at the end of this thesis)

1. C. Kriso, S. Kress, T. Munshi, M. Grossmann, R. Bek, M. Jetter, P. Michler, W. Stolz, M. Koch, and A. Rahimi-Iman, "Microcavity-enhanced Kerr nonlinearity in a vertical-external-cavity surface-emitting laser", Optics Express 27, 11914-11929 (2019)

2. C. Kriso, S. Kress, T. Munshi, M. Grossmann, R. Bek, M. Jetter, P. Michler, W. Stolz, M. Koch, and A. Rahimi-Iman, "Microcavity-enhanced Kerr nonlinearity in a vertical-external-cavity surface-emitting laser: erratum", accepted in Optics Express (2021)

3. C. Kriso, S. Kress, T. Munshi, M. Grossmann, R. Bek, M. Jetter, P. Michler, W. Stolz, M. Koch, and A. Rahimi-Iman, "Wavelength- and Pump-Power Dependent Nonlinear Refraction and Absorption in a Semiconductor Disk Laser", IEEE Photonics Technology Letters 32, 85-88 (2020)

4. C. Kriso, T. Bergmeier, N. Giannini, A. R. Albrecht, M. Sheik-Bahae, S. Benis, S. Faryadras, E. W. Van Stryland, D. J. Hagan, M. Koch, G. Mette, and A. Rahimi-Iman, "Probing the ultrafast gain and refractive index dynamics of a VECSEL", submitted to Applied Physics Letters, arXiv:2106.13664 (2021)

5. C. Kriso, A. Barua, O. Mohiuddin, C. Möller, A. Ruiz-Perez, W. Stolz, M. Koch, and A. Rahimi-Iman, "Signatures of a frequency-modulated comb in a VECSEL", Optica 8, 458-463 (2021)

Additional publications

6. H. Guoyu, C. Kriso, F. Zhang, M. Wichmann, W. Stolz, K. A. Fedorova, and A. Rahimi-Iman, "Two-chip power-scalable THz-generating semiconductor disk laser", Optics Letters 44, 4000-4003 (2019)

7. C. Kriso, M. Stein, T. Haeger, N. Pourdavoud, M. Gerhard, A. Rahimi-Iman, T. Riedl, and M. Koch, "Nonlinear refraction in $CH_3NH_3PbBr_3$ single crystals", Optics Letters 45, 2431-2434 (2020)

8. K. A. Fedorova, H. Gouyu, M. Wichmann, C. Kriso, F. Zhang, W. Stolz, M. Scheller, M. Koch, and A. Rahimi-Iman "Widely Tunable Terahertz-Generating Semiconductor Disk Laser", Physica Status Solidi RRL 14, 2000204 (2020)

Contents

1 Introduction **1**

2 VECSELs and mode-locking **5**
2.1 VECSEL gain chip 5
2.2 Mode-locking of lasers 8
2.3 Quasi-soliton mode-locking of VECSELs 9
2.4 Group delay dispersion and its measurement 11
2.5 Ultrafast carrier dynamics in semiconductors and VECSEL gain chips . 17
2.6 Self-mode-locking of VECSELs 19

3 Nonlinear lensing in VECSELs **21**
3.1 Nonlinear refractive index measurements in semiconductor optical amplifiers and VECSELs 21
3.2 Matrix calculations of nonlinear lensing in VECSEL cavities 23
3.3 Z-scan and ultrafast beam deflection 26
3.3.1 Z-scan 27
3.3.2 Ultrafast beam deflection 30

4 Frequency-modulated combs and SWIFTS **33**
4.1 Frequency combs and frequency-modulated combs 33
4.2 Shifted-wave-interference Fourier-transform spectroscopy (SWIFTS) . . 37

5 Summary and outlook **41**

Bibliography **43**

Relevant publications **51**

List of abbreviations

AM	Amplitude modulation
CB	Conduction band
CW	Continous-wave
DBR	Distributed Bragg reflector
DOS	Density of states
FFT	Fast Fourier transform
FM	Frequency modulation
FROG	Frequency-resolved optical gating
FTIR	Fourier-transform infrared spectrometer
FWHM	Full width at half maximum
FWM	Four-wave mixing
GD	Group delay
GDD	Group delay dispersion
GTI	Gires-Tournois interferometer
GVD	Group velocity dispersion
LCF	Longitudinal confinement factor
LEF	Linewidth-enhancement factor
MBE	Molecular beam epitaxy
MOVPE	Metalorganic vapor-phase epitaxy
NLSE	Nonlinear Schrödinger equation
QCL	Quantum cascade laser
QW	Quantum well
RF	Radio frequency
SESAM	Semiconductor saturable absorber mirror
SNR	Signal-to-noise ratio
SVEA	Slowy varying envelope approximation
SWIFTS	Shifted-wave-interference Fourier-transform spectroscopy
VB	Valence band
VECSEL	Vertical-external-cavity surface-emitting laser

Chapter 1

Introduction

Generating states of light with precisely defined spatial, temporal and spectral properties has become a cornerstone of contemporary research in optics and photonics due to its importance for many fields of science and technology [24]. This implies that specifically designed light sources play an ever increasing role in our daily lives. From the internet, which is based on optical communications and soon might be driven by miniaturized laser frequency comb sources [25] over applications in medicine like eye surgery or dentistry [26] to the manifold use of ultrashort pulsed lasers in additive manufacturing and laser cutting [27], our modern society relies more and more on lasers that emit ultrashort pulses at well defined moments in time and/or at specific frequencies. The significance of such kind of laser sources has also been directly recognized by two Nobel prizes in physics. One, awarded in 2005 to John Hall and Theodor Hänsch, highlights the contributions to achieving very equidistant laser lines in the frequency domain, so-called optical frequency combs [28]. Its development had been motivated by the quest to achieve unprecedented precision in measurements of optical transition frequencies of atoms and molecules for fundamental research but has nowadays found many practical applications in communications, spectroscopy and sensing due to the development of small and compact comb sources. The second Nobel prizes in physics related to pulsed laser technology has been awarded to Amy Strickland and Gérard Mourou in 2018, recognizing their invention of the "chirped-pulsed amplification" technique that meant a breakthrough in generating high-irradiance laser emission in form of ultrashort pulses and provided the basis for the aforementioned applications in laser material processing and medicine [29].

There has been a continuous trend in reducing the complexity and size of such laser sources which is required so that they can be used outside the lab. One of the most promising approaches in this respect has been the development of the semiconductor laser. These lasers have been enabled by the invention of semiconductor heterostructures grown by molecular beam epitaxy (MBE) or metalorganic vapour-phase epitaxy (MOVPE). In 2019, the estimated global market volume of semiconductor lasers has been 7.12 billion USD and is predicted to increase to 14.53 billion USD in 2030 [30], which shows the tremendous impact that these lasers have nowadays. This success stems largely from the fact that semiconductor lasers can be produced cheaply, are very compact, mostly electrically pumped and can be designed for a variety of different wavelength ranges. Also, these lasers can generate ultrashort pulses quite easily by reverse-biasing a section of the gain region. However, compared to solid-state lasers they often suffer from a rather poor beam quality and relatively low output power.

These drawbacks are overcome by vertical-external-cavity surface-emitting lasers (VECSELs). Here, a semiconductor heterostructure, consisting of periodically arranged quantum wells (QWs) or quantum dot (QD) layers, usually grown on top of a distributed Bragg reflector (DBR) and emitting parallel to the wafer growth direction, is inserted into an open laser cavity and pumped optically with a fiber-coupled multimode laser diode. This, on the one hand, enables one to achieve record high output powers and excellent beam qualities, and, on the other hand, makes it possible to insert elements like optical filters, nonlinear crystals or saturable absorbers into the cavity in order to to achieve particular operation regimes such as single-frequency operation or mode-locking [1, 2].

Shortly after the first VECSEL had been demonstrated in 1997 [31], also mode-locking was achieved by means of adding a semiconductor saturable absorber mirror (SESAM) into the cavity, yielding a pulse with a length of 22 ps [32]. After nearly two decades of development, pulse lengths of less than 100 fs have now been achieved [33, 34] and it has been theoretically predicted that pulses with a duration of just a few tens of femtoseconds should be possible to obtain [35]. However, usually sub-ps pulse lengths go along with quite strongly reduced average/peak power and thus decreased efficiency of the laser. This has been attributed to fundamental non-equilibrium carrier dynamics in the gain chip such as kinetic hole burning [36]. Moreover, degradation of SESAMs during operation with high-irradiance and ultrashort pulses has been reported, preventing stable long-term operation and is an unsolved issue so far [37].

These drawbacks of SESAM-mode-locking of VECSELs motivate looking for alternative ways of achieving ultrashort pulse emission or frequency-comb emission from VECSELs. In this context, it is interesting to mention that several groups have observed spontaneous pulse formation in VECSELs where no SESAM was inserted into the cavity [6–10]. This phenomenon is referred to as self-mode-locking and so far there has been no community-wide consent on what mechanism causes it to occur. One hypothesis is that intensity-dependent refractive index changes in the gain chip cause a significant beam-width modulation at certain positions of the cavity which could be exploited for Kerr-lens mode-locking when inserting a slit into the cavity or adjusting the pump spot size on the gain chip. This has been supported by the fact that indeed in many VECSEL self-mode-locking demonstrations a slit was crucial for obtaining pulsed operation [3].

In order to investigate whether the refractive index changes in mode-locked VECSELs are strong enough to lead to a significant beam-width modulation in the cavity, there have been preliminary investigations of the nonlinear refractive index of VECSEL gain chips [38–40]. These investigations yielded a nonlinear refractive index in the order of 10^{-16} m^2/W. However, in these investigations either unrealistically short ($\sim$100 fs) or long ($\sim$10 ps) pulse lengths were used and the probe laser was not always in resonance with the gain chip. Therefore, an overall comprehensive picture of the excitation and pulse-length dependent refractive index changes was still lacking at the beginning of this thesis. Thus, one part of this thesis deals with the characterization of the dependence of the nonlinear refractive index of representative VECSEL chips on the probe wavelength, the excitation fluence, as well as resolving its temporal dynamics, which enables one to deduce a pulse-length dependent nonlinear refractive index [13–15].

Apart from assuming nonlinear lensing as driving mechanism for self-mode-locking, there have also been suggestions that locking of the modes due to a four-wave-mixing (FWM) nonlinearity in the gain medium might occur [12]. This hypothesis has so far been very little explored in VECSELs. However, for edge-emitting lasers, self-mode-locking is commonly attributed to FWM. In fact, there has been a surge of activities in recent years investigating such kind of mode-locking, particularly with respect to quantum-cascade lasers (QCLs) [18, 41, 42]. In these lasers, ultrashort pulse generation is difficult to achieve due to the short gain lifetime ($\sim$1 ps) of the intersubband transitions. This is significantly faster than the typical round-trip time of these lasers ($\sim$100 ps), leading to relaxation of the gain before a recurring pulse could deplete it.

Still, a more general form of mode-locking can happen in these lasers. While mode-locking is usually associated with the generation of ultrashort pulses, locking of longitudinal laser modes can occur without the emission of short pulses. Mode-locking in this sense means that the phase relation between laser modes is fixed and does not change with time. The generation of bandwidth-limited pulses requires that the phase relation between adjacent modes is zero. For chirped pulses, these phase relations are not all zero. In the most extreme case of chirped laser emission, the phase differences of adjacent modes, the so-called intermode phase, covers a multiple of 2π over the laser spectrum. In such a case, the laser emission over time consists of a nearly continuous-wave (cw) signal. This kind of laser operation has been termed frequency-modulated (FM) comb as the instantaneous frequency is periodically changing with the round-trip time. While the benefit of high peak powers is lacking for FM combs, unless the chirp is externally compensated, the comb spectrum can still be exploited for applications. A prototypical and very important example of such an application is dual-comb spectroscopy. Here, two combs with slightly detuned mode-spacings are sent through an absorbing sample and subsequently detected with a fast photodetector as illustrated in Fig. 1.1. The absorption spectrum in the optical domain will then be mapped into the radio-frequency (RF) domain. Thus, a simple absorption spectrometer can be realized which comes without any moving parts as is the case for Fourier-transform or grating-based spectrometers. With the availability of compact comb sources, dual-comb spectroscopy has the potential for wide-spread use in gas sensing, for example in industrial process monitoring [43].

While FM combs have been demonstrated in a variety of edge-emitting lasers, including interband (cascade) and quantum cascade lasers, they had never been observed in surface-emitters [17, 18, 41, 44, 45]. In fact, they were believed to form only in a Fabry-Pérot cavity with high mirror losses [22, 23, 46]. In this thesis, it is demonstrated that they can also occur in VECSELs. For this, a recently developed technique called shifted-wave-interference Fourier-transform spectroscopy (SWIFTS) is used, that makes it possible to measure the intermode phase relation of a laser without requiring high peak powers [20]. The retrieved intermode phase spans 2π over the whole laser spectrum and excellent coherence is witnessed for a certain part of the laser spectrum, while another part only shows partial coherence. These findings have the potential to realize simple, high-power dual comb sources based on VECSELs where the wavelength can be designed by the mature III-V semiconductor technology [21].

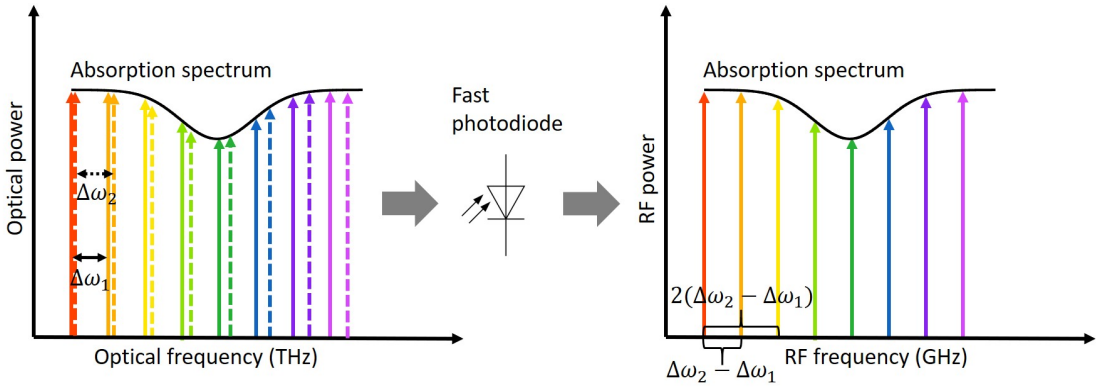

Figure 1.1: Principle of dual-comb spectroscopy, an important application of laser frequency combs. On the left side, the solid and dashed lines describe two optical frequency combs with mode spacing $\Delta\omega_1$ and $\Delta\omega_2$, respectively. The right side shows the resulting comb spectrum in the RF domain. Drawing inspired by Ref. [43]

Chapter 2 briefly provides some fundamental background information about the working principle of VECSELs and the structure of the gain chip. Furthermore, an overview about the general principles of mode-locking is given as well as some specific discussion of VECSEL mode-locking with SESAMs. This is followed by an introduction to the measurement of group delay dispersion of optical elements such as VECSELs as well as a discussion of the ultrafast carrier dynamics that occurs in semiconductors when excited optically. Finally, an overview of previous self-mode-locking reports of VECSELs is presented.

In Chapter 3, the possibility of Kerr-lens mode-locking of VECSELs is explored. After first giving an overview about previous measurements of the nonlinear refractive index in VECSELs chips, the effect of a Kerr-lens in the gain chip for two prototypical cavity geometries is theoretically investigated. Subsequently, the measurement methods Z-scan and ultrafast beam deflection are introduced, that are used for the investigation of nonlinear lensing of VECSEL samples.

Chapter 4 discusses in more detail the physics of FM combs and their previous demonstrations in edge-emitting lasers as well as the attempts to theoretically understand them. It proceeds to present the working principles and properties of the SWIFTS method that is required for characterizing the properties of FM combs.

Chapter 2

VECSELs and mode-locking

2.1 VECSEL gain chip

VECSELs can be employed in different resonator configurations depending on the desired mode of operation. Figure 2.1 displays a typical VECSEL in a linear cavity configuration. The semiconductor gain chip consists in most cases of periodically spaced quantum wells (QWs), the separation distance of which corresponds to half the lasing wavelength. However, particularly for gain chips designed for ultrashort mode-locking, an aperiodic design of the QW positions might be chosen [33, 34]. The QWs and spacer layers that form the active region are often grown on top of a distributed Bragg reflector (DBR). The DBR consists of alternating layers of two materials with different refractive index and an optical length of $\lambda/4$, respectively, and acts as a mirror. A typical and very mature material system for the near-infrared is $In_xGa_{1-x}As/Ga_xAs_{1-x}P$ for the QWs and AlAs/GaAs for the DBR. Both, record high output power in continuous-wave (cw) operation and shortest pulse lengths have been achieved with this material system, which can readily be grown by metalorganic vapor-phase epitaxy (MOVPE) [33, 34, 47]. Also, quantum dot (QD) layers can serve as gain material. In general, they have a broader gain bandwidth than QWs, which is beneficial for achieving a large tuning range or ultrashort pulse mode-locking [48, 49]. In most cases, the gain chip is optically pumped, often with a multi-mode fiber-coupled diode laser. For efficient laser operation, the thermal management of the gain chip is essential [50]. Therefore, it is bonded on a heatspreader, consisting of diamond or SiC and subsequently attached to a water cooled heat sink, which additionally can contain a Peltier-element and a temperature control circuit.

The spatial overlap of the standing wave electric field intensity at the lasing wavelength with the positions of the QWs in the gain chip is crucial for extracting maximum power of the VECSEL. The modal gain of the laser per unit time and unit volume, that takes this effect into account, is given by [51]

$$<G> = \frac{\Gamma_z G_0 f_{cv}}{V}, \tag{2.1}$$

where Γ_z is the so-called longitudinal confinement factor (LCF), G_0 a quantity that characterizes the intrinsic material gain of the QWs, $f_{cv} = f_c - f_v$ the population inversion, which is the difference of the occupation of conduction and valence band states, and V the intracavity volume of the lasing mode. The LCF contains the information

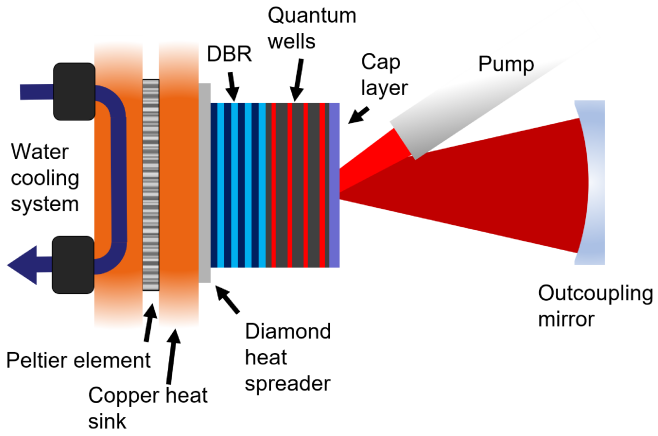

Figure 2.1: Illustration of a VECSEL chip in a linear cavity. Note that the VECSEL chip size with respect to the other cavity elements is not true to scale.

about the spatial overlap of the standing electric field intensity with the QWs and can be calculated according to [51, 52]

$$\Gamma_z = \frac{1}{N_{QW}} \frac{\sum_{q}^{N_{QW}} |E_q^+ \exp(ik_q z_q) + E_q^- \exp(-ik_q z_q)|^2}{E_0^{+2}}, \tag{2.2}$$

where N_{QW} is the number of QWs, E_q^+ and E_q^- are the electric field amplitudes of the forward- and backward-travelling optical wave at the position z_q of the qth QW and k_q is the associated wavenumber. E_0^+ is the incident electric field amplitude outside of the structure.

Figure 2.2(b) and (d) show the calculation of the wavelength-dependent LCF for a resonant and anti-resonant gain chip design, respectively. In the resonant case, the LCF exhibits a sharp resonance peak at around 1031 nm with a maximum value of 4. This means that the anti-nodes of the spectrally resonant standing wave electric field intensity in the chip structure overlap exactly with the positions of the QWs and have maximum amplitude, as can be seen in Fig. 2.2(a). To achieve maximum gain for the structure, the spectral position of the LCF peak has to be designed in a way that it overlaps exactly with the maximum of the material gain of the QWs when the power roll-over due to thermal overload occurs [50]. This requires that one takes into account the different temperature-dependent shift-rates of LCF and material gain (typical values are 0.08 nm/K and 0.34 nm/K, respectively [52]) and designs the initial detuning, i.e. the wavelength difference between LCF and material gain without pumping, accordingly. However, a resonant chip design comes with the drawback of limited spectral bandwidth of the laser output due to the narrow shape of the microcavity resonance. Therefore, for mode-locking, the chip structure is often modified in a way that there is no pronounced resonance of the microcavity at the lasing wavelength. Such a design is displayed in Fig. 2.2(c). It is usually obtained by changing the thickness of the cap layer of the chip in way that the effective optical length of the chip at the lasing wavelength λ is a multiple of $\lambda/4$ (instead of $\lambda/2$ for a resonant design). As a result, the amplitude of the LCF is significantly reduced

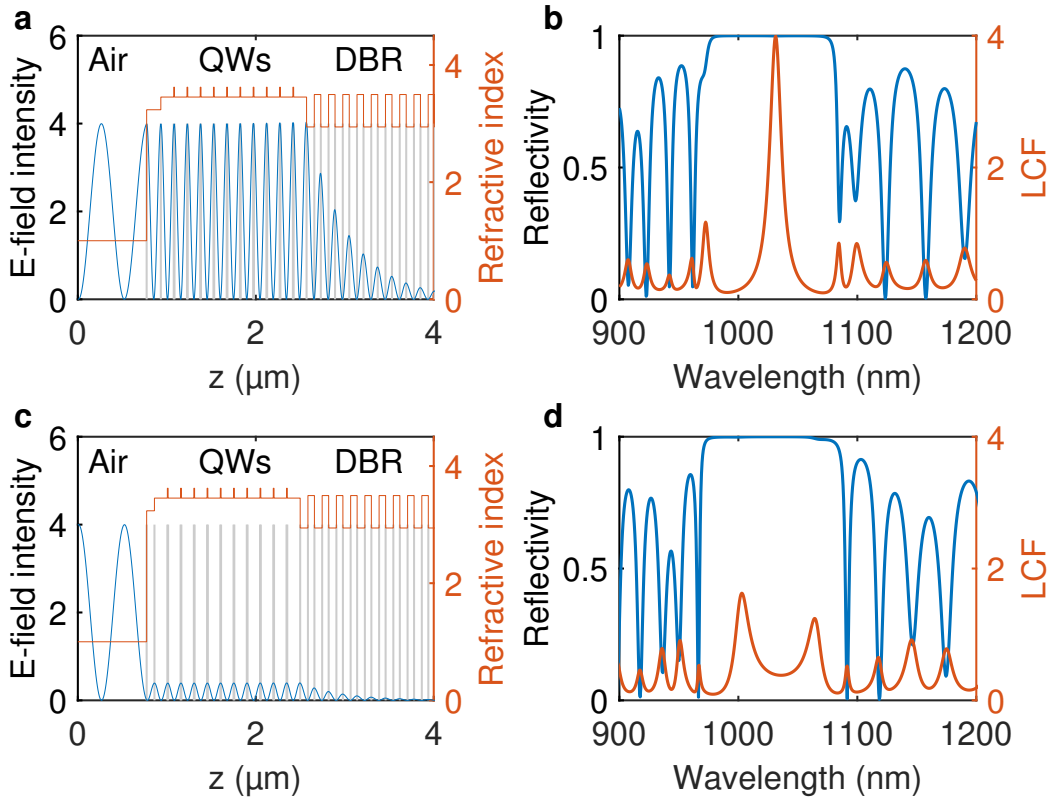

Figure 2.2: (a) and (c): Standing wave electric field intensity (blue) of a resonant and antiresonant chip design, respectively, calculated for a wavelength of 1031 nm, which corresponds to the position of the peak of the LCF in (b). The red line indicates the refractive index of the structure. The grey lines visualize the interface between materials of different composition. (b) and (d): Reflectivity (blue) and LCF (red) spectrum calculated for a resonant and antiresonant chip, respectively. Calculations were performed with a program developed within Ref. [52].

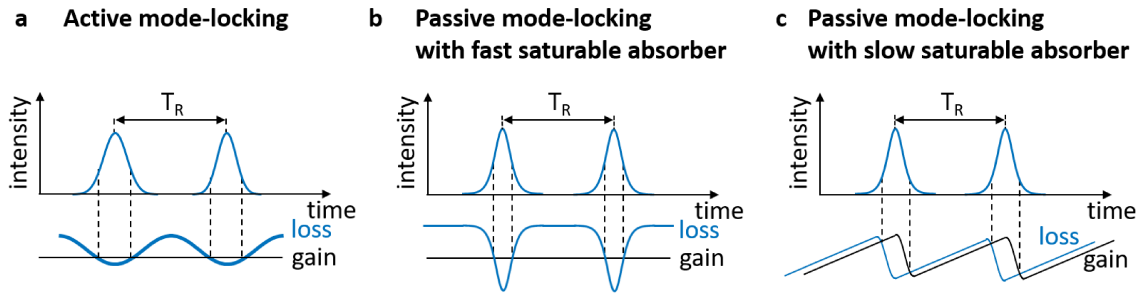

Figure 2.3: Overview of the qualitative form of the temporal loss and gain functions in (a) active mode-locking, (b) passive mode-locking with a fast saturable absorber and (c) passive mode-locking with a slow saturable absorber. Drawings created after Ref. [56]

and separated into two smaller peaks around the lasing wavelength as can be seen in Fig. 2.2(d). This leads to broadband operation of the laser, although with reduced gain compared to the resonant design. Additionally, the anti-resonant design provides a low and flat group-delay dispersion (GDD) which is crucial for obtaining ultrashort pulses. This will be discussed in more detail in section 2.4.

In addition to the LCF, Figs. 2.2(b) and (d) display the reflectivity spectrum of the respective VECSEL designs. Its characteristics are principally determined by the design of the DBR. Most importantly, it has to be designed in a way that the stopband, i.e. the wavelength region with a reflectivity very close to unity, covers the laser spectrum. Both, the number of layer pairs and the refractive index ratio of the DBR materials determine the exact reflectivity of the stopband while its width is determined by the refractive index difference of its two constituting materials [51, 52].

2.2 Mode-locking of lasers

Mode-locking refers to the synchronization of multiple mode oscillations in a laser cavity. Mode-locking is usually associated with the generation of short pulses, which is what this section is about. However, as is discussed in more detail in chapter 4, the synchronization of laser modes, i.e. establishing a fixed phase relation between them, can also lead to quasi-cw, frequency-modulated emission.

The first demonstrations of pulsed emission from lasers were based on active mode-locking, i.e. on inserting a modulator into the laser cavity that is driven with a signal the frequency of which corresponds to the inverse of the cavity round-trip time [53–55]. Due to the periodic occurrence of induced loss, the laser will preferentially emit at times without loss. Thus, pulses are formed as illustrated in Fig. 2.3(a). However, the achievable pulse duration is limited by the modulation speed of the modulator.

Shorter pulses can be produced by passive mode-locking. There, nonlinearities of a saturable absorber medium and/or the gain medium are exploited to modulate the loss of the cavity on an ultrafast time scale (femto- to picoseconds). This was first demonstrated with a saturable dye [57] and subsequently with semiconductor saturable absorbers [58, 59]. Such kind of absorber media have a finite response time with respect

to an ultrashort optical pulse, which requires a significant saturation of the gain medium in order to open an ultrashort window with reduced loss in the laser cavity as shown in Fig. 2.3(c) [56].

Eventually, the discovery of self-mode-locked Ti:sapphire lasers [60] provided a realization of a fast saturable absorber, which describes a loss mechanism that reacts instantaneously (on a femtosecond time scale) on changes of the intracavity laser irradiance (Fig. 2.3(b)). In the self-mode-locked Ti:sapphire laser, this is achieved by the optical Kerr effect, which leads to self-focusing of an high-intensity laser beam. This can be exploited as a saturable-absorber mechanism by inserting a slit into the cavity at a position where the self-focusing leads to a beam-width reduction.

In any of these scenarios, mode-locking is usually modeled by a so-called master equation, which is a differential equation that describes how the pulse envelope is affected by the various elements in the cavity like gain, loss, dispersion, etc. It is based on the slowly varying amplitude approximation (SVEA) which assumes that the pulse shape does only change slowly compared to the fast optical oscillations, on the time scale of the cavity round trip time. In the case of a fast saturable absorber, such a master equation can be written as [56],

$$\frac{1}{T_R}\frac{\partial}{\partial T}a(t) = (g-l)a(t) + \left(\frac{1}{\Omega} + iD_2\right)\frac{\partial^2}{\partial t^2}a(t) + (\gamma - i\delta)|a(t)|^2 a(t). \tag{2.3}$$

Here, T_R is the cavity round trip time, T the "slow" time in the order of T_R, $a(t)$ the electric field pulse envelope, g and l denote gain and loss, respectively, Ω is the gain bandwidth, D_2 the group delay dispersion (GDD) parameter and t the "fast" time. γ and δ describe the effect of saturable loss and self-phase modulation, respectively. In the steady state, the pulse envelope $a(t)$ will not change over multiple round-trip times. Therefore, the left side of Eq. 2.3 will be zero. In order to reach this stable state, all the effects acting on the pulse envelope have to balance each other over one round-trip time. When neglecting the GDD and self-phase modulation, a simple analytical solution can be obtained which is [56]

$$a(t) = A_0 \operatorname{sech}(t/\tau), \tag{2.4}$$

where A_0 is the pulse peak amplitude and $\tau = \sqrt{\frac{2g}{\gamma A_0^2 \Omega^2}}$ characterizes the pulse width.

While the solution for active mode-locking results in a Gaussian-shaped pulse, the Master equation for a slow saturable absorber cannot be solved analytically. In the next section, the results of a numerical mode-locking model for a laser with strong gain saturation, which corresponds to the case of semiconductor laser (VECSEL) mode-locking, will be discussed in more detail.

2.3 Quasi-soliton mode-locking of VECSELs

Mode-locking of VECSELs with SESAMs was first investigated theoretically in Ref. [61]. The strong gain and saturable absorber saturation are characteristic for this mode-

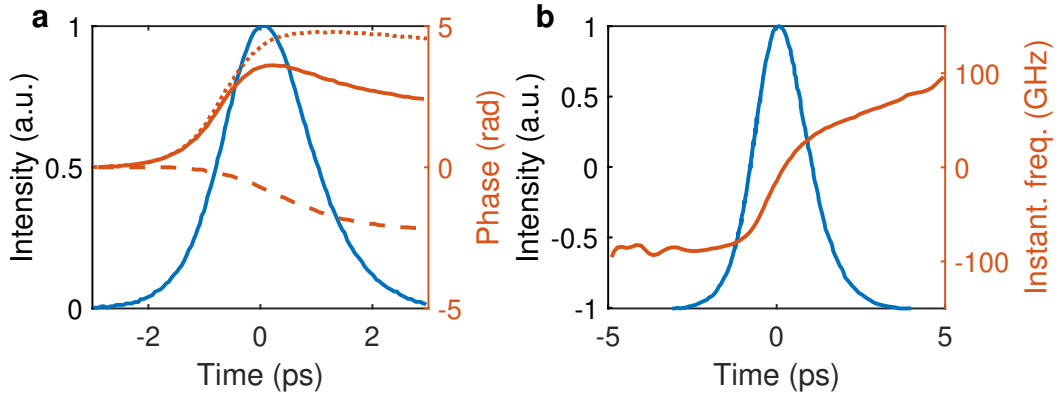

Figure 2.4: (a) Calculated pulse intensity envelope (blue solid line) and phase changes due to gain (dotted orange line) and absorber (dashed orange line), as well as the combined phase change (solid orange line), and (b) calculated pulse intensity envelope (blue) and instantaneous frequency (orange) of a quasi-soliton mode-locked VECSEL. Figures recreated from Ref. [61]

locking scenario. The gain saturation can be described by [61, 62]

$$\frac{dg(t)}{dt} = -\frac{g(t) - g_0}{\tau_g} - g(t) \cdot \frac{P(t)}{E_{sat,g}}, \tag{2.5}$$

where $g(t)$ is the power gain, g_0 the small-signal gain, τ_g the gain lifetime, $P(t)$ the time-dependent intracavity power of the laser which describes the pulse envelope, and $E_{sat,g}$ the saturation energy of the gain medium.

Similarly, the absorber saturation is described by [62]

$$\frac{dq(t)}{dt} = -\frac{q(t) - \Delta R}{\tau_a} - q(t) \cdot \frac{P(t)}{E_{sat,a}}, \tag{2.6}$$

with $q(t)$ being the power loss induced by the saturable absorber, ΔR the modulation depth, τ_a the recovery time and $E_{sat,a}$ the saturation energy. Both, gain and absorber saturation induce a phase shift onto the pulse which is commonly described by the linewidth-enhancement factor (LEF) α and is defined as [61, 62]

$$\Delta\varphi_g = -\frac{\alpha_g}{2} \cdot g(t) \tag{2.7}$$

for the gain and equivalently for the absorber (α_a). As the gain and absorption losses occur with opposite sign in the mode-locking master equation or numerical model, the respective phase shifts will partially cancel each other out. Thereby, the absorber induces a negative phase shift while the gain induces a positive one. Exemplary phase shifts obtained by solving the numerical model described in Ref. [61] are shown in Fig. 2.4(a) together with the pulse envelope. It can be seen that the combined phase shift of saturable absorption and the gain do not cancel each other out exactly. For stable mode-locking and shortest pulses, the remaining phase shift has to be compensated by an appropriate amount of group delay dispersion (GDD) in the cavity. This means that a slightly positive GDD of a few 1000 fs^2 will result in shortest pulses as has also been verified experimentally [63].

Due to the fact that the pulse shape and intensity will adapt in way that nonlinear phase changes induced by absorber and gain medium are, at least partially, compensated by the GDD of the cavity, this kind of mode-locking has been termed quasi-soliton mode-locking. Fig. 2.3(b) shows the moderate frequency chirp as well as the slightly asymmetric pulse shape that is characteristic for this mode-locking scenario.

Two things should be mentioned here. First, in self-mode-locking of VECSELs, the nonlinear phase shift induced by the absorber falls away. Therefore, a self-mode-locked VECSEL will most likely have a different optimal requirement of optimal GDD for achieving shortest pulses.
Second, the concept of the LEF is just an approximation and assumes that the dynamics of the gain (or absorber) translates linearly to a refractive index change that causes the phase shift to occur. However, this is not true in general as gain/absorption changes are related by Kramers-Kronig relations to refractive index changes and vice versa. In Ref. [15], it is shown that the refractive index dynamics of the gain chip differs significantly in, both, shape and dominating time scales, from the gain dynamics. This should be taken into account in future modeling efforts of VECSEL mode-locking.

Furthermore, for very short pulses in the sub-100 fs regime, the master equation approach based on the SVEA is not applicable anymore. Instead, fully microscopic models based on the semiconductor Bloch equations should be used to adequately capture the complex physics of the light-matter interaction, including many-body effects, at these ultrashort time scales [35, 36].

2.4 Group delay dispersion and its measurement

As pointed out in the previous section, the group delay dispersion (GDD) plays a crucial role in VECSEL mode-locking. Therefore, it is of great importance to be able to precisely measure and potentially compensate it. In general, all cavity elements can contribute to the total GDD that a pulse will experience during its round-trip through the cavity.

In order to better understand the concept of the GDD as well as the related group velocity dispersion (GVD), an optical pulse in the SVEA is written at the point $z = 0$, directly before it propagates through a dispersive medium, as [64, 65]

$$a_{in}(t) = A(t)e^{i\omega_0 t}, \tag{2.8}$$

where $A(t)$ is the pulse envelope at $z = 0$ and ω_0 is the optical carrier frequency of the pulse. The effect of dispersion is most easily applied in the frequency domain. Thus, Eq. 2.8 is Fourier-transformed and multiplied by a propagation term,

$$\tilde{a}(\omega) = \tilde{A}_{in}(\omega - \omega_0)e^{-i\beta(\omega)L}, \tag{2.9}$$

where $\beta(\omega)$ is the frequency-dependent propagation constant of the pulse in the dispersive medium of length L. $\beta(\omega)$ can be expanded into a Taylor series around ω_0,

$$\beta(\omega) \approx \beta^{(0)} + (\omega - \omega_0)\beta^{(1)} + \frac{(\omega - \omega_0)^2}{2!}\beta^{(2)} + \frac{(\omega - \omega_0)^3}{3!}\beta^{(3)} + \dots, \tag{2.10}$$

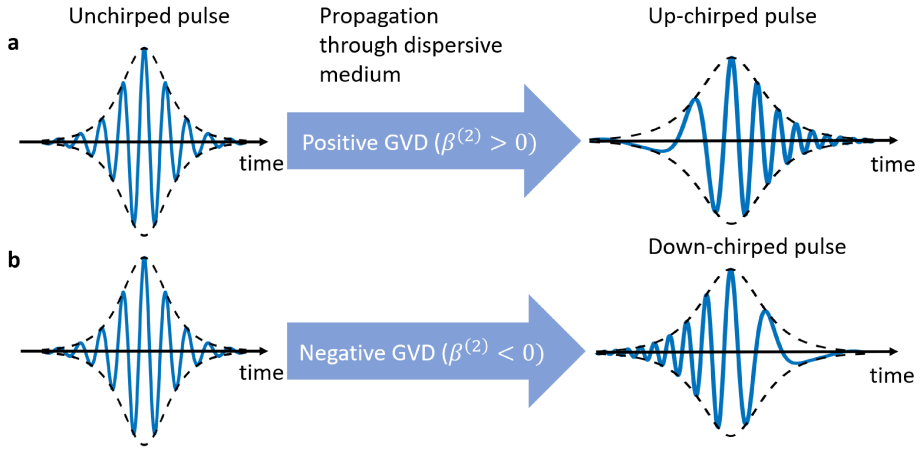

Figure 2.5: Illustration of pulse broadening and chirp for (a) positive GVD and (b) negative GVD. Figure inspired by Ref. [65]

with

$$\beta^{(n)} = \frac{\partial^n}{\partial \omega^n} \beta(\omega)\Big|_{\omega=\omega_0}. \tag{2.11}$$

Here, $\beta^{(2)}$ is the second-order GVD while $\beta^{(2)}L$ represents the second-order GDD (with a sign ambiguity depending on its definition, see the remark after Eq. 2.22). Thus, the GVD characterizes the length-independent second-order dispersion of a medium while the GDD provides an absolute value of the accumulated dispersion.

Eventually, the pulse after propagation through the dispersive medium is obtained by Fourier-transforming Eq. 2.9 back into the time domain [64, 65],

$$a_{out}(t) = \frac{1}{2\pi} \int_{-\infty}^{+\infty} \tilde{A}_{in}(\omega - \omega_0) e^{-i\beta(\omega)L} e^{i\omega t} d\omega. \tag{2.12}$$

For an intuitive understanding of the effect of dispersion on an optical pulse, it is useful to write down the expression of the frequency-dependent group delay (GD),

$$\tau(\omega) = \frac{d\beta(\omega)}{d\omega} L = \beta^{(1)}L + \beta^{(2)}(\omega - \omega_0)L, \tag{2.13}$$

where only expansion terms of $\beta(\omega)$ up to second order were kept. Equation 2.13 describes in what amount of time a signal component of the pulse at frequency ω propagates through the dispersive medium of length L. The first term is independent of frequency and therefore characterizes the propagation time of the pulse envelope, with $\beta^{(1)}$ corresponding to the inverse of the group velocity. The second term depends linearly on frequency and therefore leads to different propagation times for different frequency components of the pulse. This will lead to a broadening of the pulse envelope. Depending on the sign of $\beta^{(2)}$, the pulse will either exhibit an up-chirp ($\beta^{(2)} > 0$) or a down-chirp ($\beta^{(2)} < 0$), which means that high-frequency components appear at the trailing or leading edge of the pulse, respectively, as illustrated in Fig. 2.5.

There are several ways that an optical pulse can experience a frequency-dependent propagation constant. The most basic one is the case where the refractive index of

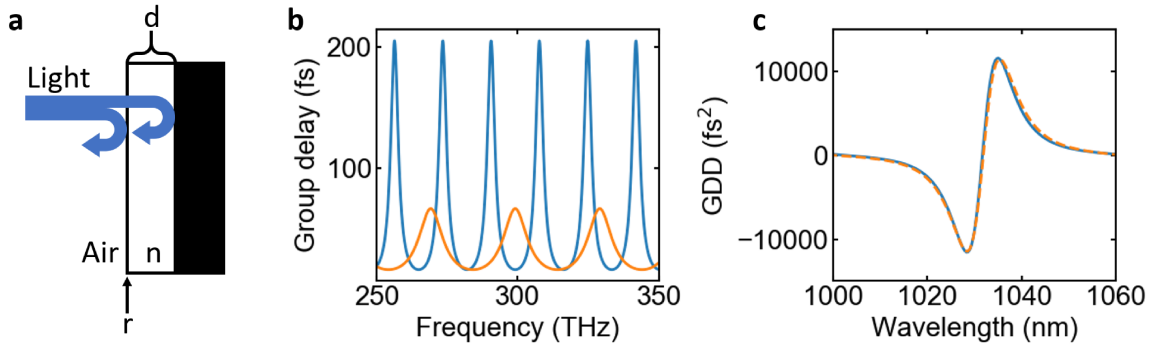

Figure 2.6: (a) Illustration of a Gires-Tournois interferometer (GTI) of thickness d, refractive index n and reflectivity r of the air–material interface. (b) Calculated group delay of a GTI with a thickness of approx. 2.5 µm and a refractive index of 3.5 (blue line) and 2 (orange line). (c) Group delay dispersion (GDD) calculated from the blue curve of (b) (blue solid line) and from the matrix calculation of the VECSEL chip design displayed in Fig. 2.2(a) (orange dashed line).

the propagation material is frequency-dependent ($\beta(\omega) = \frac{\omega}{c_0} n(\omega)$). This is referred to as material dispersion and it usually plays a significant role for long propagation lengths of the pulse through the medium. For VECSELs, with a thickness of only a few micrometers, the effect of material dispersion is tiny and can usually be neglected. The main contributor to GDD in a VECSEL is the interference effect of the microcavity composed of the air–VECSEL interface and the DBR. For a better understanding of this effect, one can look at the properties of a simplified structure consisting of a layer of a lossless material with a refractive index n on top of a perfectly reflecting mirror as displayed in Fig. 2.6(a). Such a structure is also referred to as Gires-Tournois interferometer (GTI). The complex field reflectivity Γ of such a device can be calculated as [64]

$$\Gamma = \frac{r + e^{-i\phi(\omega)}}{1 + re^{-i\phi(\omega)}}, \tag{2.14}$$

where $r = \frac{1-n}{1+n}$ is the field amplitude reflectivity and the round-trip phase shift $\phi(\omega)$ is given by

$$\phi(\omega) = \frac{2dn\omega}{c_0} - \phi_0, \tag{2.15}$$

with d being the thickness of the material layer with refractive index n, ω the angular frequency, c_0 the vacuum speed of light and ϕ_0 the phase shift due to the reflection at the perfectly reflecting interface which is neglected in the following.

The phase accumulated due to propagation through the reflecting structure is defined by [64]

$$\tan \Psi(\omega) = \frac{-(1 - r^2)\sin(\phi(\omega))}{2r + (1 + r^2)\cos(\phi(\omega))}. \tag{2.16}$$

Now, the frequency-dependent GD is obtained by [64]

$$\tau(\omega) = -\frac{\partial \Psi(\omega)}{\partial \omega} = \frac{(1 - r^2)t_0}{1 + r^2 + 2r\cos(\phi(\omega))}, \tag{2.17}$$

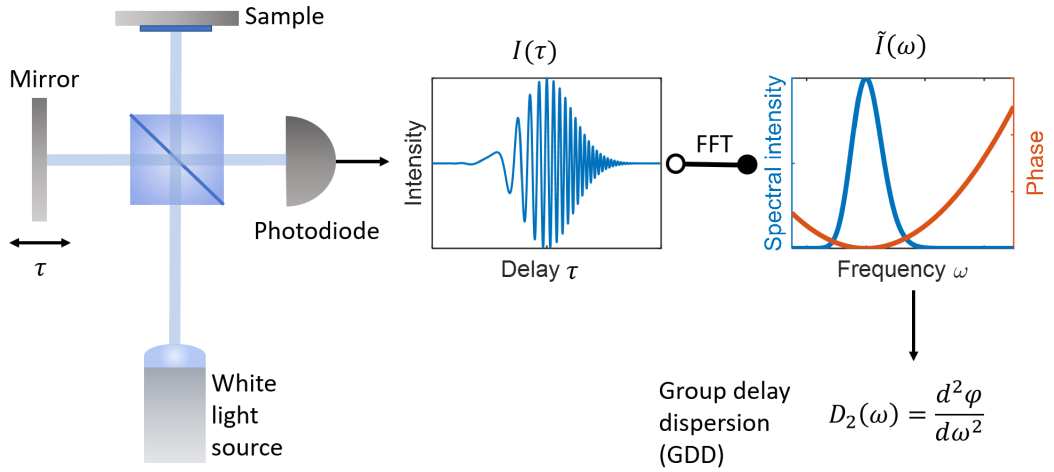

Figure 2.7: Principle of GDD measurement. A Michelson interferometer driven by a white-light source with the sample (VECSEL) inserted in one arm yields an interferogram as a function of the optical delay induced by translating the movable mirror. When Fourier-transformed to the frequency-domain, this interferogram yields a spectral phase that delivers the GDD from its second derivative with respect to angular frequency.

with $t_0 = \frac{2dn}{c_0}$ being the round-trip time through the microcavity. $\tau(\omega)$ is plotted in Fig. 2.6(b) for a layer of thickness of 2.5 µm and for two values of the refractive index (3.5 and 2). The periodically appearing peaks in the spectrum correspond to cases where $\phi(\omega) = 2m\pi$ with m being an integer. This means that the initially reflected light and the light that gets reflected after one round-trip through the structure interfere destructively, having reflection amplitudes of r and $(1-r)e^{-i\phi}$, respectively (with r being negative and $|r| < 1$). Therefore, light at the resonance frequencies can escape less "easily" and gets trapped longer. In this context, the GD can be understood intuitively as characteristic time that photons at a particular frequency stay in the structure before leaving it. As shown in Fig. 2.6(b), this time also depends on the reflectivity (or refractive index of the layer).

The GDD can now be obtained by taking the derivative of the GD with respect to the angular frequency [64],

$$\frac{\partial\tau(\omega)}{\partial\omega} = \frac{(1-r^2)t_0^2\sin(\phi(\omega))}{(1+r^2+2r\cos(\phi(\omega)))^2}, \tag{2.18}$$

where any frequency dependence of t_0 is neglected. Figure 2.6(c) shows the GDD calculated with this formula for a structure with a thickness of approx. 2.5 µm and a refractive index of 3.5. Also shown in the figure is the calculation of the GDD obtained from the matrix calculations that have been used to calculate the electric field of the resonant VECSEL design in Fig. 2.2(a). It can be seen that both calculations match very well. Thus, the dispersion induced by the microcavity of the VECSEL can be well understood by considering it as a GTI interferometer.

In order to measure the GDD of a VECSEL gain chip, a Michelson interferometer is used which is driven by a white-light source that covers the relevant spectral range of the VECSEL laser operation. The mirror of one arm is replaced by the reflecting VECSEL

chip (gain mirror) while the other arm is constituted by a metal mirror mounted on a translation stage or mechanical shaker as illustrated in Fig. 2.7. When this arm is scanned, an interferogram can be recorded at the output of the interferometer with a photodetector. This interferogram can be described by [66]

$$I(\tau) \propto \langle E_1^2(t-\tau)\rangle + \langle E_2^2(t)\rangle + \langle E_1(t-\tau)E_2^*(t)\rangle + \langle E_1^*(t-\tau)E_2(t)\rangle, \tag{2.19}$$

where $\tau = \frac{2\Delta z}{c_0}$ and Δz is the mirror displacement. Angle brackets denote temporal averaging of the slow photodetector. Here, the electric field of the two arms written in complex notation is referred to as $E_1(t)$ and $E_2(t)$, respectively. The first two terms of Eq. 2.19 are constant with respect to τ and indicate the average intensity while the last two terms in Eq. 2.19 are the interferometric terms. When Fourier-transforming the interferometric terms of Eq. 2.19 one obtains the transmission spectrum of an interferometer with a sample inserted in one of the arms as [66]

$$\tilde{I}(\omega) \propto r_{12}(\omega)|E(\omega)|^2 T(\omega) e^{i(\varphi_{sample}(\omega)+\varphi_{12}(\omega))}. \tag{2.20}$$

Here, $r_{12}(\omega)e^{i\varphi_{12}}$ is the complex transmission spectrum of the Michelson interferometer without a sample inserted while $T(\omega)e^{i\varphi_{sample}(\omega)}$ is the complex transmission spectrum of the sample. It is $E_1(t) = r_{12}(\omega)e^{i\varphi_{12}}E_2(t)$ and the index for the respective arm of the interferometer has been omitted for the electric field in Eq. 2.20. $r_{12}(\omega)e^{i\varphi_{12}}$ represents the intrinsic mismatch of the two arms of the interferometer and has to be calibrated out of the experimental data with an additional measurement. Subsequently, $\varphi_{sample}(\omega)$ can be retrieved that is required for the calculation of the sample dispersion via

$$D_2(\omega) = \frac{\partial^2 \varphi_{sample}(\omega)}{\partial \omega^2}. \tag{2.21}$$

For the numerical calculation of $D_2(\omega)$ with a Fast-Fourier-Transform (FFT) algorithm, the interferogram of Eq. 2.19 should be filtered with a window function (e.g. a triangular or Gaussian function) to suppress noise due to the finite scanning range and subsequently left-circularly shifted so that the linear slope, which appears in the phase of the Fourier-transform when the function to be Fourier-transformed is translated, is minimized. The GDD is then obtained numerically by calculating [67]

$$D_2[\omega] = \frac{\varphi_{sample}[\omega+\delta\omega] - 2\varphi_{sample}[\omega] + \varphi_{sample}[\omega-\delta\omega]}{\delta\omega^2}. \tag{2.22}$$

According to its definition in Ref. [67], $D_2(\omega) = -\frac{\partial^2\beta(\omega)}{\partial\omega^2}L$. It is worth mentioning that there exists a trade-off between spectral resolution and noise of the GDD measurement. This is due to the fact that increasing spectral resolution means that one has to include a larger delay window which contains the interferogram. Particularly, when this delay exceeds the width of the interferogram, only additional noise is included in the data. Therefore, the noise of the GDD measurement increases strongly with enhanced resolution. A quantitative estimate of this effect has been provided in Ref. [67] by the standard deviation $\sigma_{D2}(\omega)$ of the GDD for a flat-top-like spectrum of width $\Delta\omega$,

$$\sigma_{D2}(\omega) = \left[\frac{3}{I_n^2(\omega)}\frac{\Delta\omega^2}{\mathrm{SNR}\, pM(\delta\omega)^6}\right]^{1/2}, \tag{2.23}$$

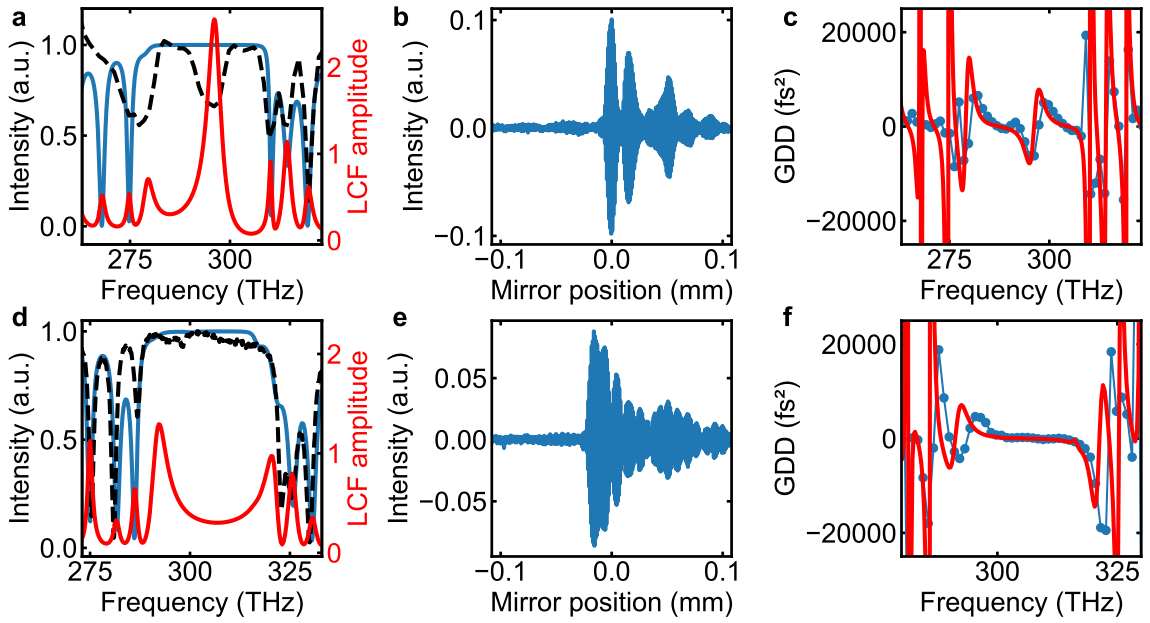

Figure 2.8: Overview of GDD-relevant data for a resonant (upper row) and an anti-resonant (lower row) VECSEL chip. (a) and (d) show the calculated (blue solid line) and measured (black dashed line) reflectivity spectrum (left axis), as well as the calculated LCF (red, right axis) for a resonant and anti-resonant VECSEL chip, respectively. (b) and (e) show exemplary white-light interferograms when the resonant or anti-resonant VECSEL chip is inserted in one arm of the interferometer, respectively. (c) and (f) display the calculated (red solid line) and measured GDD (blue dots) for the resonant and anti-resonant chip, respectively. The measured GDD has been averaged over approximately 1000 subsequent measurements. Figures (d), (e) and (f) have been adapted from the supplementary material of Ref. [21].

where $I_n(\omega)$ is the normalized source spectrum, SNR the signal-to-noise ratio in the time-domain, p the number of data points, M the number of averages and $\delta\omega$ the spectral resolution. This shows that one has to drastically increase either the intensity of the source or the number of averages to compensate for the noise increase due to improved resolution.

Figure 2.8 gives an overview of calculated and measured VECSEL chip properties including the GDD for a rather resonant and an anti-resonant chip design. Figures 2.8(a) and (d) show the measured reflectivity spectra of the two chips as well as the calculated one and the LCF obtained from the matrix calculations in analogy to the results of Fig. 2.2. Figures 2.8(b) and (e) show the envelope of exemplary white-light interferograms obtained for the two chips when they are inserted in one arm of the Michelson interferometer. Finally, Figs. 2.8(c) and (f) display the GDD measured with the white-light interferometer of both chips as well as the calculated GDD obtained from the matrix simulations. It can be seen that the agreement of calculation and measurement is quite good. The resonant chip in Fig. 2.8(c) exhibits the characteristic strong slope of the GDD at the spectral position of the resonance of the LCF (as seen in Fig. 2.8(a)) while the anti-resonant chip in (f) displays a very flat and small GDD at the spectral center of the stopband.

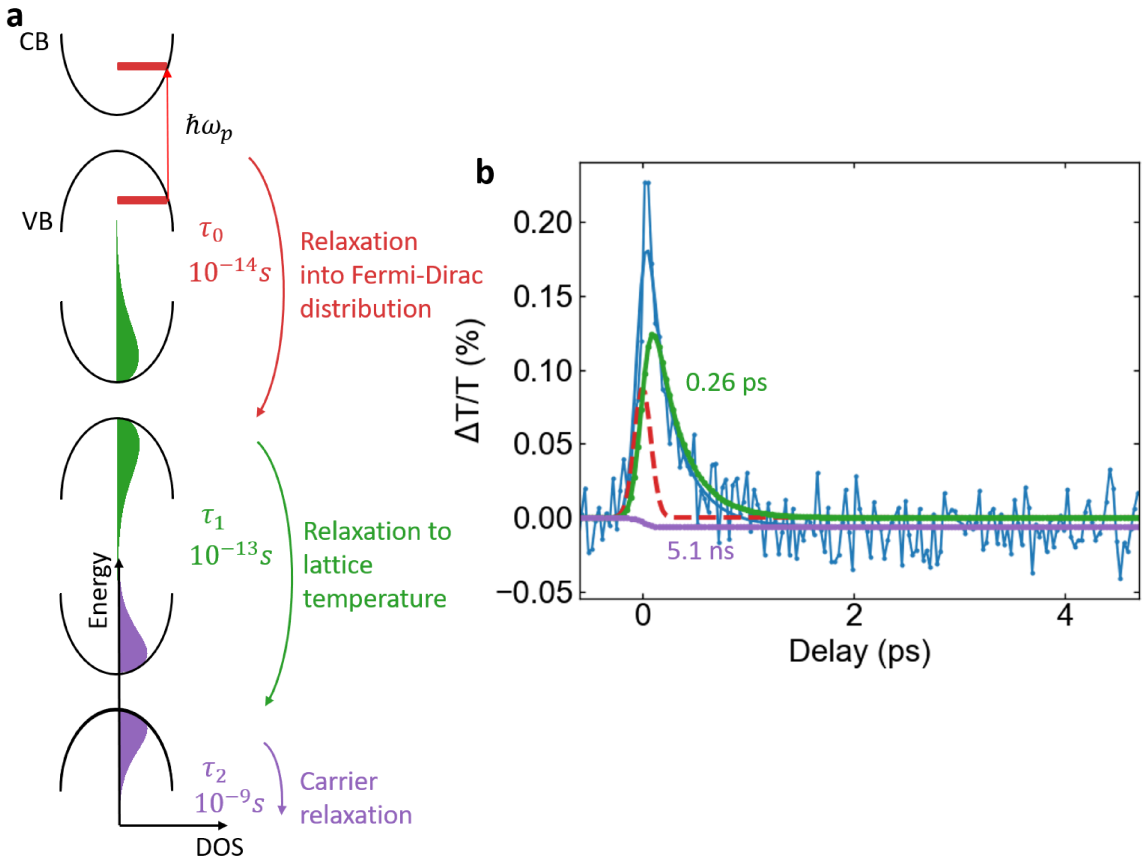

Figure 2.9: (a) Illustration of different carrier processes with their characteristic time scales occurring after excitation of a semiconductor with a laser pulse at frequency ω_p in the absorption regime. Figure inspired by Ref. [68]. (b) Pump-probe transmission measurement of a VECSEL in the absorption regime (blue line with dots) with fit function (blue solid line) and its contributions with their respective time constants displayed and their colors representing the different processes shown in (a). CB: conduction band, VB: valence band, DOS: density of states

2.5 Ultrafast carrier dynamics in semiconductors and VECSEL gain chips

As has been discussed in Section 2.3, the dynamics of the gain and saturable absorber medium strongly influence the mode-locking properties of VECSELs. In this section, a brief overview is given over the different processes and their time scales that occur after a direct band-gap semiconductor is optically excited with an ultrashort laser pulse. It also will be discussed how these different processes occur in a pump–probe measurement on a VECSEL chip.

Figure 2.9(a) shows schematically the different carrier processes that happen after a semiconductor is excited with an optical pulse, the photon energy $\hbar\omega_p$ of which is larger than the band gap. The optical pulse first creates a Dirac-function-like distribution of "hot" carriers in the conduction/valence band (CB/VB). In a degenerate pump-probe measurement, this results in a sudden increase of probe transmission as most of the states that can be excited at the pulse photon energy have been occupied due excitation

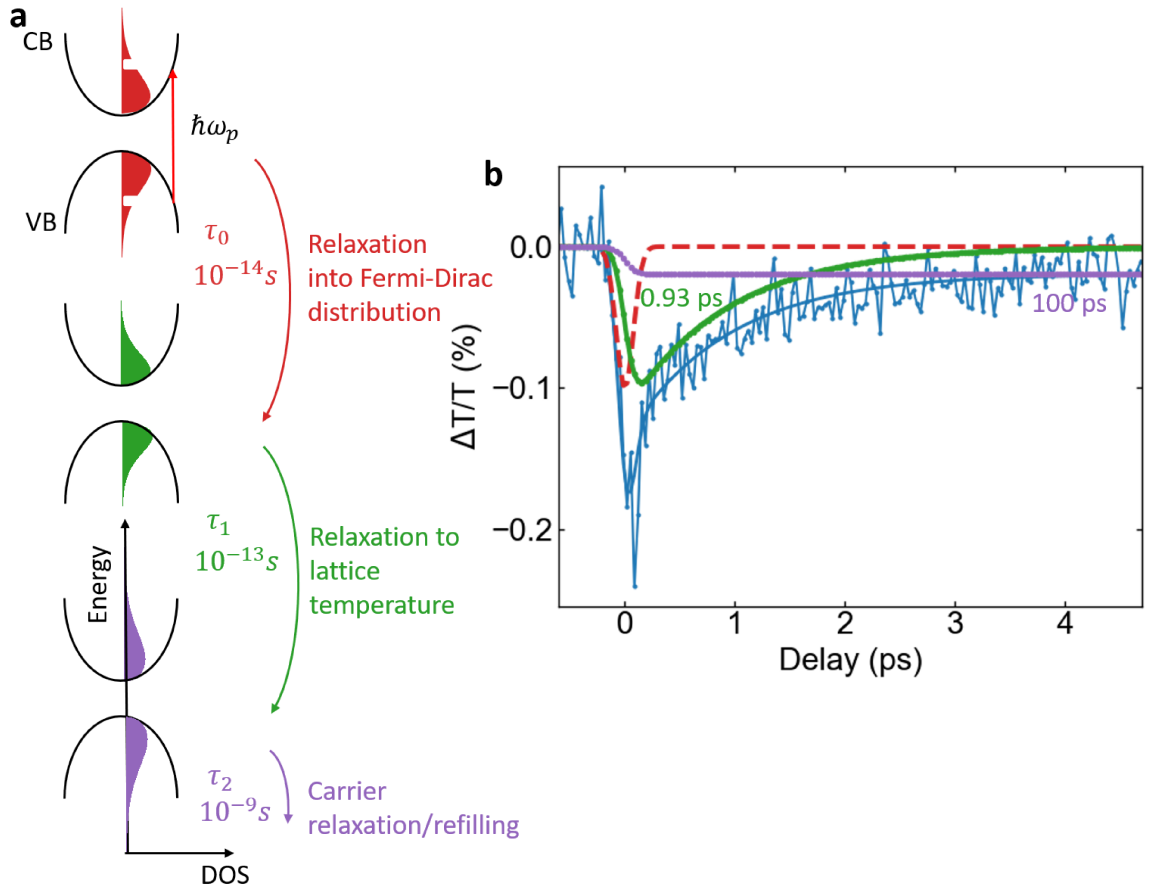

Figure 2.10: (a) Illustration of different carrier processes with their characteristic time scales occurring after an already excited semiconductor is hit with a laser pulse at frequency ω_p in the gain regime. Figure inspired by Ref. [68]. (b) Pump-probe transmission measurement of a VECSEL in the gain regime (blue line with dots) with fit function (blue solid line) and its contributions with their respective time constants displayed and their colors representing the different processes shown in (a). CB: conduction band, VB: valence band, DOS: density of states

with the pump pulse (saturable absorption/Pauli blocking) as shown in Fig. 2.9(b). Subsequently, this Dirac-function-like distribution will relax into a Fermi-Dirac distribution on a time-scale of few tens of femtoseconds, mostly due to carrier–carrier interactions [68]. This process can only be resolved with very short laser pulses and appears as an instantaneous process if pump/probe pulses with longer duration are used, as is the case for the measurement in Fig. 2.9(b) of a VECSEL.

Subsequently, the still elevated temperature of the Fermi-Dirac distribution will adjust to the lattice temperature by electron–phonon scattering [68]. This occurs on a characteristic time scale of hundreds of femtoseconds and results in an exponential decay of the probe transmission in a pump–probe measurement (Fig. 2.9(b)). Finally, the excited carriers will relax back to their ground state, which occurs over hundreds of picoseconds or a few nanoseconds [68]. The time constant of this process cannot be very precisely determined in the measurement shown in Fig. 2.9(b) due to a total delay range of only a few picoseconds and appears rather as a constant offset at longer delay. Furthermore, if only carrier relaxation takes place, one would expect that the

long time-constant contribution in Fig. 2.9(b) is positive. The fact that it is (slightly) negative might stem from additional processes such as free-carrier absorption (see e.g. Ref. [69]) that have been neglected in the above discussion.

Similar processes happen when an optical pulses hits a semiconductor that is already excited as shown in Fig. 2.10(a) and which corresponds to the situation during laser operation. The pulse will burn a "spectral hole" into the carrier distribution due to stimulated emission. Subsequently, a Fermi-Dirac distribution of the carrier occupations will be reestablished by carrier–carrier scattering, which is followed by the adjustment of the carrier temperature to the lattice temperature, happening on a time-scale of tens and hundreds of femtoseconds, respectively. Afterwards, the relaxation of carriers to their ground-state, or refilling of the carriers when the system is pumped, will occur over a time scale of hundreds of picoseconds or a few nanoseconds. Figure 2.10(b) shows the probe transmission of a pump-probe measurement of an initially excited VECSEL. As this measurement has been conducted with a laser with a pulse length of around 130 fs, only processes slower than this pulse length will appear as non-instantaneous contributions in the measurement. Note that here the probe pulse experiences decreased transmission when the pump pulse experiences gain. In Ref. [15], which is part of this thesis, both pump–probe transmission measurements and deflection measurements, corresponding to refractive index changes, are presented for various excitation levels of the VECSEL chip and discussed in detail.

2.6 Self-mode-locking of VECSELs

Here, a brief review over past VECSEL self-mode-locking claims is given. The first report of this kind was given by Chen and coworkers in Ref. [6]. There, a gain chip designed for the near-infrared emitted spontaneously pulses as short as 645 fs in a linear cavity configuration without any slit inserted into the cavity. From the same group, mode-locking with higher-order modes was reported in a V-cavity, yielding pulses of 2.1 ps length [70], and, in a linear cavity with slit, pulses of 2.35 ps length [71]. Kornaszewski et al. found self-mode-locking of a similar QW gain chip in a long cavity of approximately 70 cm, where a slit was inserted in front of one of the end mirrors [7]. There, pulses of 930 fs with a calculated peak power of 6.8 kW were obtained. However, this result was disputed because of measurement data which hinted to unstable mode-locking such as a long-span RF spectrum that showed a reduced signal-to-noise ratio (SNR) of lines at multiples of the fundmental repetition frequency [11, 72]. Furthermore, Albrecht et al. showed self-mode-locking in a V-cavity with a slit inserted and provided a theoretical calculation of the beam-width modulation that supported Kerr-lens mode-locking [8]. Pulse durations down to 482 fs were measured. Gaafar et al. obtained excellent self-mode-locking properties in a Z-cavity with a QW gain chip and a slit inserted in front of one end mirror. Both fundamental and harmonic mode-locking was reported as well as significant second-harmonic generation with a nonlinear crystal due to the pulsed laser emission outside of the cavity [9, 73]. Peak powers up to 950 W and pulse lengths down to 860 fs were obtained and both RF spectrum and autocorrelation indicated clean and stable mode-locking. Also, with the same gain chip, self-mode-locking in a linear cavity with a slit, inserted at the

outcoupling mirror, was achieved, with 3.5 ps pulse duration and 55 W peak power [16]. Furthermore, self-mode-locking of a QD gain chip in a linear cavity with inserted slit was reported by Gaafar et al. [74]. Here, pulses of 830 fs length and a peak power of 460 W were obtained, the latter being a record for QD VECSELs at the time of the report.

While the previous reports were all obtained for emission wavelengths in the near-infrared, Bek et al. reported self-mode-locking of a VECSEL of the AlGaInP system emitting in the visible at 666.5 nm in a linear cavity without slit. However, the pulse autocorrelation indicated a rather long pulse length (22 ps), and a coherence peak on top of the autocorrelation trace pointed to not perfectly clean pulses. Table 2.1 gives an overview of the reported self-mode-locking demonstrations including measured pulse lengths and peak powers.

Year	Gain medium	Wavelength	Pulse length	Peak power	Ref.
2011	InGaAs/GaAsP QWs	1064 nm	654 fs	283 W	[6]
2012	InGaAs/GaAsP QWs	985 nm	930 fs	6.8 kW	[7]
2012	InGaAs/GaAsP QWs	1064 nm	2.1 ps	1.7 kW	[70]
2013	InGaAs/GaAsP QWs	1025 nm	482 fs	1.8 kW	[8]
2014	InGaAs/GaAsP QWs	1014 nm	860 fs	950 W	[9, 73]
2014	InGaAs/GaAsP QDs	1040 nm	830 fs	460 W	[74]
2015	InGaAs/GaAsP QWs	1059 nm	2.35 ps	60 W	[71]
2016	InGaAs/GaAsP QWs	1040 nm	3.5 ps	55 W	[16]
2017	GaInP/AlGaInP QWs	666.5 nm	22 ps	0.34 W	[10]

Table 2.1: Overview of VECSEL self-mode-locking reports.

Chapter 3

Nonlinear lensing in VECSELs

3.1 Nonlinear refractive index measurements in semiconductor optical amplifiers and VECSELs

Since the first demonstration of spontaneous pulse formation in VECSELs [6], the possibility of Kerr-lens mode-locking has been conjectured as being a possible driving mechanism of self-mode-locking [7, 8], among other hypotheses such as four-wave-mixing in the gain region [12] and saturable absorption due to unpumped quantum wells [6]. The Kerr-lens hypothesis has been particularly supported by self-mode-locking reports of VECSELs where a slit, inserted into the cavity, seemed to be crucial for obtaining the mode-locked state (see the discussion in the previous section) [7–9, 74] . However, it has not been known exactly what the nonlinear refractive index of a VECSEL chip, which leads to self-induced nonlinear lensing, under typical operation conditions is. It should be noted that the effective nonlinear refractive index not only depends on the design of the gain chip, i.e. on how many quantum wells are arranged in a resonant or anti-resonant fashion, but also depends on the excitation due to optical pumping as well as the pulse length of the probe beam. Additionally, the filter function of the microcavity affects the total, measured nonlinear refractive index of the device. Investigations on semiconductor optical amplifiers (SOAs) yielded an effective nonlinear refractive index in the order of 10^{-16} m^2/W for both the AlGaAs and the InGaAsP material system and using pulses with durations ranging from 100 to 200 fs [75, 76]. Typically, in these devices, the refractive index change is composed of an ultrafast component stemming from the ultrafast Kerr effect and components related to slower processes such as carrier heating and changes of the total carrier occupation due to net gain or net absorption which leads to refractive index changes for longer time spans and which are related by Kramers–Kronig relations.

While the investigations on SOAs provide some reference of what strength of an effective nonlinear refractive index to expect in VECSELs, there are differences between the two systems. In particular, SOAs are typically spatially extended over a few hundreds of micrometers and in waveguide geometry. This renders so-called spectral effects important, which refers to amplitude–phase coupling due to the finite gain curvature [77]. While these effects can probably be neglected in VECSELs due to the very thin gain region of a few microns, stronger pump irradiances and the effect of the microcavity have to be considered in VECSELs. Therefore, for a precise estimate of how strong a nonlinear Kerr lens would occur in a typical VECSEL mode-locking scenario, the nonlinear refractive index of a VECSEL should directly be measured.

The first investigation of this kind was performed in Ref. [38]. There, a nonlinear refractive index of $-1.5 \cdot 10^{-16}$ m^2/W was measured by Z-scan without excitation on an anti-resonant VECSEL chip. The nonlinear refractive index became positive when optical pumping was applied, increasing to around $+1.5 \cdot 10^{-16}$ m^2/W. However, the probe laser was more than 10 nm red-detuned from the lasing wavelength and the pulse length of 10 ps was quite long compared to typical pulse durations of around 1 ps and below for most self-mode-locking results [6, 8, 9]. Subsequent work probing a VECSEL chip closer to the lasing wavelength found a lower nonlinear refractive index in the order of -10^{-17} m^2/W and little effect of optical pumping of the gain chip for a pulse length of only a few hundreds of femtoseconds [39, 40].

n_2 [w/o exc.]($\cdot 10^{-16}$ m^2/W)	n_2 [max. exc.]($\cdot 10^{-16}$ m^2/W)	Pulse length	Ref.
-1.5 ± 0.2	$+1.4 \pm 0.1$	10 ps	[38]
-0.44 ± 0.13	-	230 fs	[39]
-0.65 ± 0.03	-0.6 ± 0.04	340 fs	[40]
-5 ± 1.3	-	150 fs	[13]
-0.83 ± 0.36	-0.26 ± 0.36	150 fs	[14]
-1.2	-	121 fs	[15]

Table 3.1: Overview of the measured nonlinear refractive index of a VECSEL, without and with maximum excitation fluence, respectively, and the applied pulse length.

In this thesis, these investigations are extended to spectrally- and time-resolved measurements of the nonlinear refractive index of a VECSEL chip. In Ref. [13], it is shown that the microcavity strongly affects the measured nonlinear refractive index of the unpumped gain chip, with a maximum magnitude of around $-5 \cdot 10^{-16}$ m^2/W for a probe pulse length of 150 fs. Ref. [14] shows that optical pumping leads to a decrease of the magnitude of the nonlinear refractive index for 150 fs-pulses when accounting for the thermal shift of the lasing wavelength. Finally, Ref. [15] provides the most comprehensive overview of the nonlinear optical properties of a VECSEL chip by measuring the time-resolved refractive index response of a gain chip as a function of different excitation fluences. This allows one to calculate the pulse-length as well as excitation-dependent effective nonlinear refractive index which becomes positive for high excitation fluences and pulse lengths larger than 1 ps. It is in the order of 10^{-16} m^2/W for a DBR-free VECSEL structure that does not exhibit any pronounced microcavity effect at the lasing wavelength. Table 3.1 gives an overview of the values of the nonlinear refractive index measured on VECSEL chips so far.

In the following section, it is investigated whether a nonlinear refractive index of such an order of magnitude can lead to significant beam width modulation in representative VECSEL cavities and therefore make Kerr-lens mode-locking plausible for VECSELs. Subsequently, a short overview of the two measurement techniques that are used for the

characterization of the nonlinear refractive index (Z-scan and ultrafast beam deflection) is provided.

3.2 Matrix calculations of nonlinear lensing in VECSEL cavities

A first assessment of how strong a laser beam will be perturbed when propagating through a medium with a nonzero nonlinear refractive index can be obtained by comparing the radial phase shift that is induced by a Gaussian beam in a Kerr-medium to the phase shift induced by a thin lens. The nonlinear refractive index n_2 is defined as

$$\Delta n = n_2 I, \tag{3.1}$$

where Δn is the refractive index change induced by a laser beam of irradiance I. If the nonlinear refractive index is instantaneous, i.e. the nonlinear medium has a response time faster than the pulse length, as it is usually the case for the ultrafast (bound-electronic) Kerr effect, both, the temporal and the spatial dependence of $\Delta n(r,t)$, will correspond to that of the intensity profile of the laser beam $I(r,t)$. For a Gaussian beam, this means that the induced refractive index change has a radial dependence according to [78]

$$\Delta n(r) = \Delta n(0) e^{-\frac{2r^2}{w^2}} \approx \Delta n(0)\left(1 - \frac{2r^2}{w^2}\right) = \Delta n(0) - \Delta n'(r), \tag{3.2}$$

where w is the half-width (HW)/e^2 of the laser beam. Now, with the radial phase shift of a thin lens of focal length f, and for a wavelength λ, being [79]

$$\Delta\varphi(r) = \frac{\pi r^2}{\lambda f}, \tag{3.3}$$

one can deduce the focal length of the nonlinear lens by comparing Eq. 3.3 to the phase shift induced by the radially-dependent refractive index change of Eq. 3.2, which is

$$\Delta\varphi(r) = k\Delta n'(r) d = \frac{2\pi}{\lambda}\frac{2r^2}{w^2}\Delta n(0) d, \tag{3.4}$$

where d is the propagation length through the nonlinear medium. The focal length of the nonlinear lens can then be written as

$$f = \frac{w^2}{4\Delta n(0) d} = \frac{w^2}{4 n_2 I_0 d} = \frac{\pi w^4}{8 n_2 d P}. \tag{3.5}$$

Here, I_0 is the peak irradiance of the Gaussian beam and $P = I_0 \pi w^2/2$ the spatially averaged power. Remarkably, the focal length of the Kerr lens scales with the power of four as a function of the beam width in the medium, the length of which has been assumed to be thin compared to the Rayleigh length of the Gaussian beam.

Equation 3.5 assumes that in the Kerr medium the curvature of the wavefront of the Gaussian beam is negligible. However, in general, this is not the case when considering a VECSEL chip placed somewhere in an external cavity. To get a more accurate picture

of the effect of a Kerr lens in a VECSEL cavity, one should perform calculations of the beam propagation through the cavity. For this, one uses the ABCD matrix formalism [80]. There, the complex beam parameter q is defined as

$$\frac{1}{q} = \frac{1}{R} - i\frac{\lambda}{\pi w^2}, \tag{3.6}$$

where R is the radius of curvature of the wavefront of the Gaussian beam. Then, the modification of the beam (parameter) caused by an optical element is calculated by

$$q_2 = \frac{Aq_1 + B}{Cq_1 + D}, \tag{3.7}$$

where q_1 and q_2 are the beam parameters before and after propagation through the optical element, respectively, and A, B, C and D are the matrix elements of the ray matrix arranged in the form

$$\begin{pmatrix} A & B \\ C & D \end{pmatrix}. \tag{3.8}$$

The ABCD-matrix of a combination of optical elements is obtained by matrix-multiplying the ABCD-matrices of the individual components in the order of propagation. For a thin lens, this matrix is

$$\begin{pmatrix} 1 & 0 \\ -\frac{1}{f} & 1 \end{pmatrix}, \tag{3.9}$$

where f is the focal length, and for propagation in free space along a distance L, the ABCD-matrix is

$$\begin{pmatrix} 1 & L \\ 0 & 1 \end{pmatrix}. \tag{3.10}$$

According to Ref. [81], the ABCD-matrix of a Kerr-lens is

$$\sqrt{1-\gamma}\begin{pmatrix} 1 & d_e \\ -\frac{\gamma}{(1-\gamma)d_e} & 1 \end{pmatrix}, \tag{3.11}$$

where $d_e = d/n_0$ is the optical length of the Kerr medium and

$$\gamma = \left[1 + \frac{1}{4}\left(\frac{2\pi w_c^2}{\lambda d_e} - \frac{\lambda d_e}{2\pi w_0^2}\right)^2\right]^{-1}\frac{P}{P_c}. \tag{3.12}$$

Here, w_c is the spot size in the center of the Kerr medium and w_0 is the beam waist of the unperturbed beam. P is the intracavity peak power and P_c is the critical self-focusing power defined as

$$P_c = \frac{\lambda^2}{2\pi n_0 n_2}, \tag{3.13}$$

with n_0 being the refractive index of the medium.

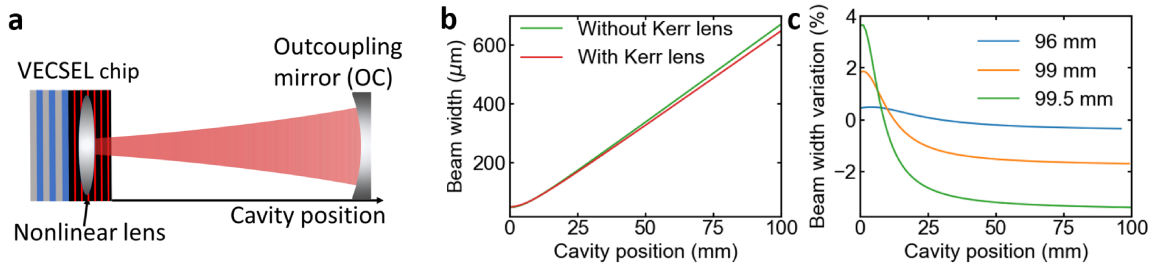

Figure 3.1: Effect of a nonlinear lens in a linear VECSEL cavity as displayed in (a) with an outcoupling mirror of radius of curvature of 100 mm. (b) Gaussian beam width as a function of the cavity position for a cavity length of 99.5 mm without a Kerr lens (green line) and with a Kerr lens at the VECSEL chip position due to a nonlinear refractive index of $+10{\cdot}10^{-16}$ m^2/W of the gain chip (red line). 0 mm corresponds to the chip position. (c) Beam-width variation due to a nonlinear refractive index of $+10{\cdot}10^{-16}$ m^2/W of the gain chip for different cavity lengths.

To calculate the beam profile of a given laser cavity, one has to propagate the Gaussian beam one round trip through the cavity and apply self-consistency, i.e. impose the condition that the beam profile is identical after one round trip through the cavity.

Figure 3.1(b) displays the beam width profile of the linear cavity shown in Fig. 3.1(a)) with a length of 99.5 mm and a curved outcoupling mirror with a radius of curvature of 100 mm. Once, it is calculated with no nonlinear lens assumed in the gain chip, and once it is calculated assuming a nonlinear refractive index of $+10{\cdot}10^{-16}$ m^2/W being present in the gain chip. It can be seen that the presence of a nonlinear lens leads to a reduction of the beam width at the outcoupling mirror. Thus, inserting a slit close to the end mirror and slightly cutting the intracavity laser beam there might favour pulsed laser operation. Furthermore, Fig. 3.1(c) plots the beam-width variation for the aforementioned nonlinear refractive index for several cavity lengths. The beam-width variation $\Delta w(z)$ as a function of the cavity position z is defined as

$$\Delta w(z) = \frac{w_{Kerr}(z) - w_{up}(z)}{w_{up}(z)}, \tag{3.14}$$

where $w_{Kerr}(z)$ and $w_{up}(z)$ are the beam width of the cavity perturbed by the Kerr lens and without it (unperturbed), respectively. It can be seen that the beam-width variation is largest at the edge of the stability range of the cavity, i.e. with a cavity length close to 100 mm. For smaller cavities, like for a cavity length of 96 mm, the beam-width modulation due to the Kerr lens reduces significantly.

The choice of sign and magnitude of the nonlinear refractive index used here for the calculation of the intracavity beam profile has been motivated by the measurements in Ref. [15], which is part of this thesis. It shows that for high excitation fluences and pulse lengths of a few picoseconds the effective nonlinear refractive index is positive and in the order of $+10{\cdot}10^{-16}$ m^2/W. Therefore, such a linear cavity might be well suited for Kerr-lens mode-locking of VECSELs with pulses of a length of a few picoseconds. Mode-locking in such a cavity configuration has indeed been reported in Ref. [16] from which the value of the intracavity peak power (5500 W) has been taken here to calculate the effect of nonlinear lensing. It should be noted that in the case of a negative nonlinear refractive index, the beam width variation changes sign compared to the case with a

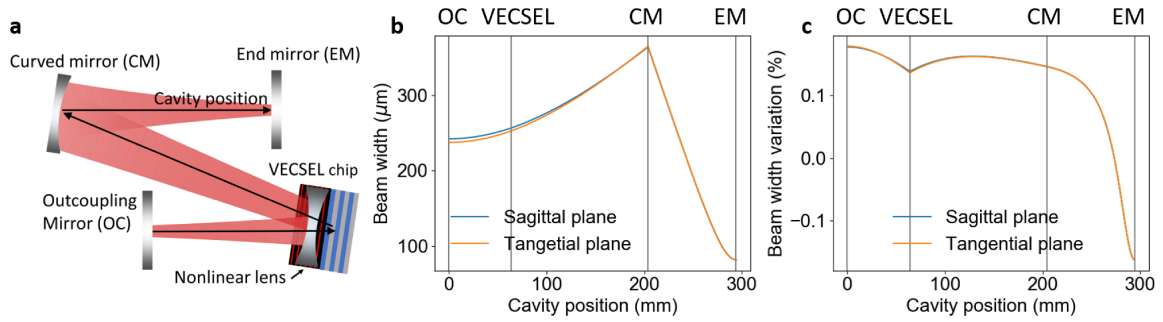

Figure 3.2: Effect of a nonlinear lens in a Z-cavity as displayed in (a) with a curved mirror of radius of curvature of 150 mm. (b) Gaussian beam width as a function of the cavity position with a Kerr lens at the VECSEL chip position due to a nonlinear refractive index of $-5{\cdot}10^{-16}$ m^2/W of the gain chip for the sagittal and tangential plane. (c) Beam width variation due to a nonlinear refractive index of $-5{\cdot}10^{-16}$ m^2/W of the gain chip for the sagittal and tangential plane.

positive nonlinear refractive index. This means that for the case of the linear cavity a beam-width narrowing would occur at the position of the gain chip and a beam-width widening at the position of the outcoupling mirror. Then, hard aperture mode-locking with a slit at the position of the gain chip is not feasible, due to optical pumping of the gain chip. However, when making the pump spot size smaller than the spot size of the fundamental mode on the chip, so-called soft-aperture mode-locking may become achievable instead.

Furthermore, in the following, it is investigated whether self-mode-locking of a VECSEL in a Z-cavity, as has been reported experimentally in Ref. [9], can be explained by a nonlinear lens in the gain chip. Such a Z-cavity is displayed in Fig. 3.2(a). Assuming a negative nonlinear refractive index of $-5{\cdot}10^{-16}$ m^2/W, which corresponds to the maximum value measured in Ref. [13], a beam-width reduction of about 0.16 % is obtained at the position of the end mirror as can be seen in Fig. 3.2(c). This is a significantly less strong beam-width modulation than obtained in the case of the linear cavity of Fig. 3.1. Changing the relative mirror position in the cavity to operate it closer to the stability limit does not affect the beam-width modulation as strongly as in the case of the linear cavity. This is due to the fact that the mode spot size on the VECSEL is quite large (200−300 µm) as can bee seen in Fig. 3.2(b). Recalling that the focal length of a nonlinear lens as defined in Eq. 3.5 scales with the power of four as a function of the spot size, explains the smaller beam-width perturbation in this Z-cavity. Therefore, it can be concluded that Kerr-lens mode-locking in such a Z-cavity should be more difficult to achieve or less stable than in a linear cavity operated at the edge of its stability range.

3.3 Z-scan and ultrafast beam deflection

In order to characterize the effective nonlinear refractive index of VECSEL gain chips, two measurement methods are used in this work. The first one, Z-scan, is a single-beam technique that does not resolve the temporal dynamics of the refractive index change, but provides a value for the effective nonlinear refractive index averaged over the pulse

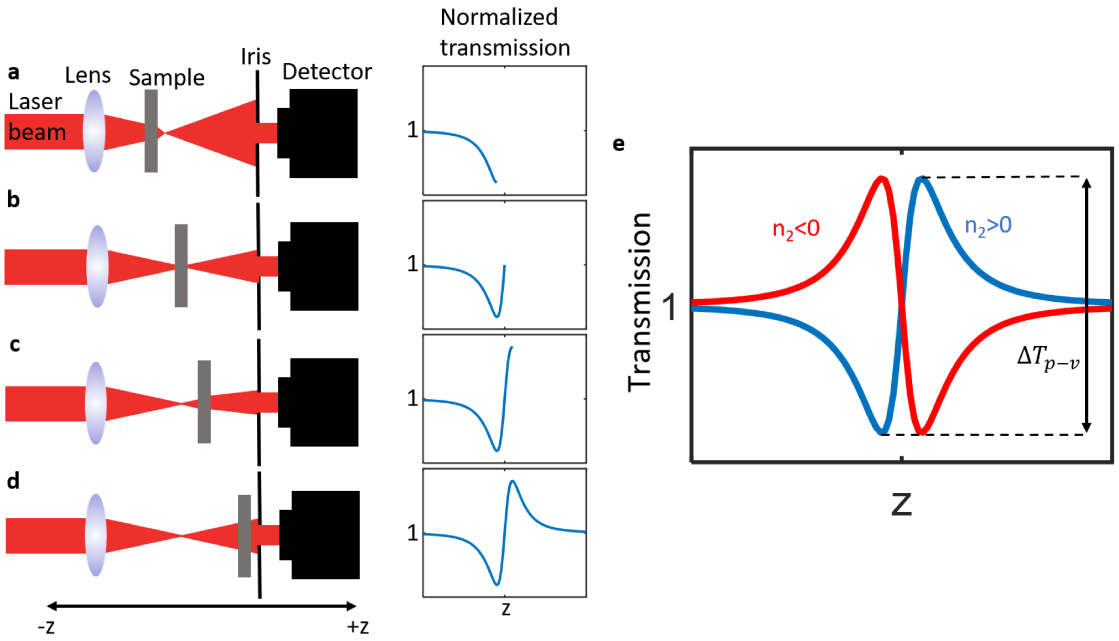

Figure 3.3: Principle of Z-scan: (a)-(d) Subsequent movement of a sample through a Z-scan setup and the corresponding transmission of light through the iris for a positive nonlinear refractive index measured as a function of the sample position z. (e) Visualization of Z-scan measurements with different signs of the nonlinear refractive index n_2.

length. The second method, ultrafast beam deflection, is based on two pulsed laser beams and probes the temporal response of the refractive index change by performing a pump–probe measurement.

3.3.1 Z-scan

The Z-scan technique was invented in 1990 and quickly became very popular due to its simplicity and the fact that the sign of the nonlinear refractive index can be unambiguously retrieved from the measurement [82]. In this section, an overview of the working principle of Z-scan is given, based on Ref. [82].

Z-scan exploits the spatial distortion of a single laser beam that propagates through a medium with a nonlinear refractive index n_2. Figures 3.3(a)-(d) display the basic principle of the Z-scan method. There, a sample with a positive nonlinear refractive index is moved through a focused and pulsed laser beam. Usually, pulse durations in the pico- or femtosecond regime are used to provide high irradiance and reduce the effect of thermal lensing. The transmitted beam is recorded as time-averaged signal by a detector placed in the far field of the beam, in front of which an iris is placed which is aligned centrally with respect to the probe's Gaussian beam profile. When the sample is far from the focus of the beam, the irradiance, i.e. the peak power per unit area, is low and thus the self-focusing of the laser beam that occurs due to the nonlinear refractive index in the sample is negligible. Therefore, the normalized transmission, which is the transmission with sample inserted divided by the transmission without sample inserted, is close to unity. However, when the sample is moved closer to the

focus of the laser beam, the irradiance increases and self-focusing of the beam occurs. This will move the position of the initial focus closer to the lens. Thus, the beam will have diverged stronger when reaching the iris and less power is measured by the detector. Consequently, the normalized transmission decreases. When reaching the focus (Fig. 3.3(b)), the normalized transmission returns to unity and no beam distortion occurs. When moving out of the focus towards the detector, the beam divergence at the iris decreases and more power reaches the detector, leading to an increase in normalized transmission (Fig. 3.3(c)). Finally, the normalized transmission returns to unity when the sample is moved even further away from the detector (Fig. 3.3(d)). The transmission measurement, recorded as a function of the sample position z, therefore exhibits a minimum (valley) and a maximum (peak) around the position of the focus of the lens. The transmission difference between peak and valley, ΔT_{p-v}, indicates the magnitude of the nonlinear refractive index. Furthermore, the respective position of peak and valley around the focus position is determined by the sign of the nonlinear refractive index as illustrated in Fig. 3.3(e).

For a quantitative modeling of Z-scan measurements, the phase shift experienced by a Gaussian beam when propagating through the sample can be written as [82]

$$\Delta\phi(z,r,t) = \frac{\Delta\Phi_0(t)}{1+z^2/z_0^2} e^{-\frac{2r^2}{w^2(z)}}. \tag{3.15}$$

Here, $z_0 = \frac{\pi w_0^2}{\lambda}$ is the Rayleigh range of the Gaussian beam, with w_0 being its beam waist, $w(z) = w_0^2\left(1+\frac{z^2}{z_0^2}\right)$, and $\Delta\Phi_0(t)$ is the on-axis phase shift at the focus given by

$$\Delta\Phi_0(t) = k\Delta n_0(t) L_{eff}. \tag{3.16}$$

Here, $L_{eff} = \left(1-e^{-\alpha L}\right)$, with L being the sample length and α the linear absorption coefficient. $\Delta n_0(t) = n_2 I_0(t)$, with n_2 being the nonlinear refractive index and I_0 being the on-axis peak irradiance at focus. Note that, with this definition, the n_2 used here corresponds to γ in Ref. [82]. The complex electric field of the laser beam, after just having propagated through the sample, can now be written as

$$E_e(r,z,t) = E(z,r,t) e^{-\alpha L} e^{i\Delta\phi(z,r,t)}. \tag{3.17}$$

Here, $E(z,r,t)$ is the initial optical beam that is assumed to be a Gaussian beam and therefore can be written as

$$E(z,r,t) = E_0(t)\frac{w_0}{w(z)} \exp\left(-\frac{r^2}{w^2(z)} - \frac{ikr^2}{2R(z)}\right), \tag{3.18}$$

where $R(z) = z\left(1+\frac{z_0^2}{z^2}\right)$ is the radius of curvature of the wavefront at position z and $E_0(t)$ is the electric field envelope of the laser pulse at focus in the SVEA. The Guoy phase shift has been neglected in Eq. 3.18 [82].

Now, one has to calculate from Eq. 3.17 the far field at the position of the iris, E_a. For this, one can use a certain kind of modal decomposition method ("Gaussian decomposition") as detailed in Ref. [82]. The transmitted power through the iris is then calculated as

$$P_T(z) = c_0\epsilon_0 n_0 \pi \int_0^{r_i} |E_a(z,r,t)|^2 r dr, \tag{3.19}$$

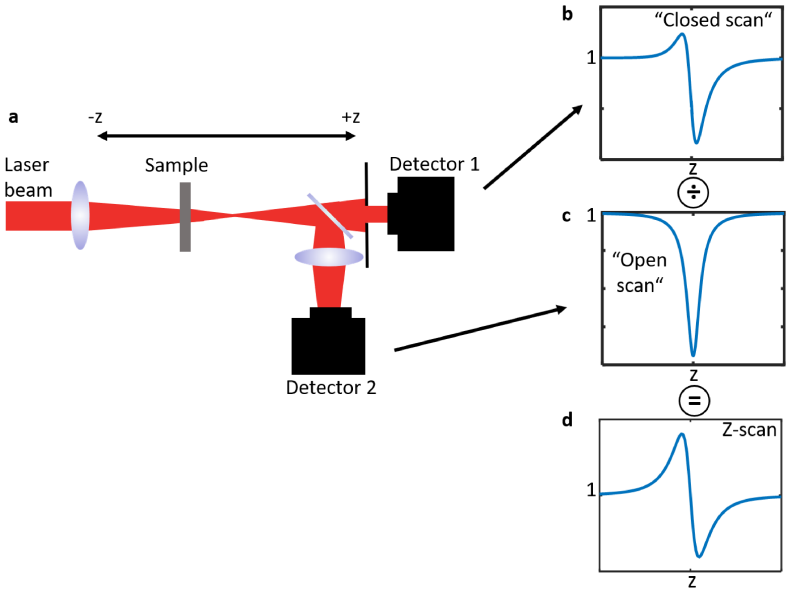

Figure 3.4: (a) Z-scan setup for simultaneous measurement of nonlinear refraction and nonlinear absorption. (b) Measurement of the detector with an iris placed in front of it ("Closed scan"). (c) Measurement of the detector which captures the full beam cross section ("Open scan"). (d) Z-scan measurement of nonlinear refraction obtained by dividing the "Closed scan" in (b) by the "Open scan" in (c).

with c_0 and ϵ_0 being the vacuum speed of light and the vacuum permittivity, respectively, and r_i being the radius of the iris opening. Note that also here z is the sample position. The normalized transmission as a function of the sample position z is obtained by calculating

$$T(z) = \frac{\int_{-\infty}^{+\infty} P_T(z)dt}{S\int_{-\infty}^{+\infty} P_i(t)dt}, \tag{3.20}$$

where $P_i(t)$ is the initial, instantaneous power and $S = 1 - \exp\left(-\frac{2r_i^2}{w_i^2}\right)$ the ratio of the transmitted power through the iris, with w_i being the beam radius at the iris without sample inserted. Eq. 3.20 can be used to fit experimental Z-scan measurements and extract the nonlinear refractive index of the sample. However, for small phase changes, a simple relation can be established between the nonlinear phase shift $<\Delta\Phi_0(t)>$, averaged over the probe pulse length (denoted by the brackets), and the peak–valley difference of the Z-scan trace,

$$\Delta T_{p-v} \approx 0.406(1-S)^{0.25}|\ <\Delta\Phi_0(t)>\ |. \tag{3.21}$$

This relation is valid with a $\pm 2\%$ accuracy if $|\ <\Delta\Phi_0(t)>\ | \leq \pi$ [82]. Eq. 3.21 allows to estimate the sensitivity of Z-scan. For example, with a measurement resolution of $\Delta T_{p-v} = 1\%$ and $S = 0.05$, the Z-scan measurement resolves wavefront distortions of less than $\lambda/250$, provided the sample exhibits a good optical quality.

The time-averaged nonlinear phase shift is $<\Delta\Phi_0(t)> = k<\Delta n_0(t)>L_{eff}$, with $<\Delta n_0(t)>$

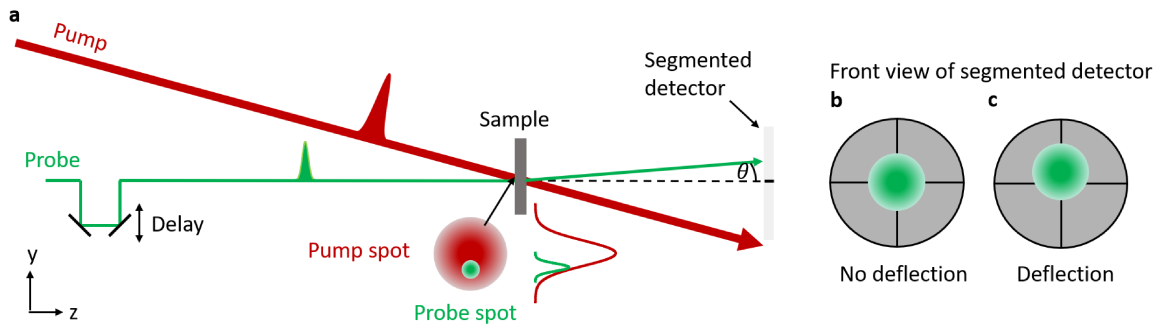

Figure 3.5: (a) Setup of the ultrafast beam deflection method. (b),(c) Front view of the segmented detector without and with deflection of the probe beam, respectively. Figure recreated after Ref. [83]

being the time-averaged refractive index change according to

$$<\Delta n_0(t)> = \frac{\int_{-\infty}^{\infty} \Delta n_0(t) I_0(t) dt}{\int_{-\infty}^{\infty} I_0(t) dt}. \tag{3.22}$$

So far, it has been assumed that the sample exhibits no significant nonlinear absorption such as two-photon absorption. However, if this is the case, the above-mentioned procedure for the extraction of the nonlinear refractive index can still be applied in most cases. For this, one has to normalize the Z-scan measurement, performed with an iris in front of the detector, by a Z-scan measurement performed with a detector that captures the whole beam cross section. These two measurements can be done simultaneously if a beam splitter and a second detector are available, as shown in Fig. 3.4(a). The measurement performed with an iris will be sensitive to both nonlinear refraction and nonlinear absorption (Fig. 3.4(b)) while the measurement without iris will only be sensitive to nonlinear absorption (Fig. 3.4(c)). When dividing the former by the latter measurement, one obtains a Z-scan measurement that only contains the effect of nonlinear refraction, provided that nonlinear absorption is not too strong, i.e., in the case of two-photon absorption, $\beta I_0 L_{eff} \leq 1$ and $\beta/(2kn_2) \leq 1$, with β being the two-photon absorption coefficient [82]. β is defined according to its contribution to the total absorption

$$\alpha(I) = \alpha_0 + \beta I, \tag{3.23}$$

where α_0 is the linear absorption coefficient and I the laser irradiance. For Gaussian-shaped pulses, β can be obtained by fitting the Z-scan measurement, for which the detector captures the whole beam cross section, with [82]

$$T(z) = \frac{1}{\sqrt{\pi} q_0(z)} \int_{-\infty}^{\infty} \ln\left(1 + q_0(z) e^{-\tau^2}\right) d\tau, \tag{3.24}$$

where $q_0(z) = \beta I_0 L_{eff} / \left(1 + z^2/z_0^2\right)$.

3.3.2 Ultrafast beam deflection

Z-scan only contains implicit information about the temporal dynamics of the nonlinear refractive index via the pulse length of the probe laser. To get a comprehensive picture

of the temporal response of nonlinear refraction, one would have to vary systematically the pulse length which is quite tedious. The beam deflection method solves this issue by performing a pump–probe measurement of nonlinear refraction [84]. The corresponding setup and principle are depicted in Fig. 3.5. Here, a strong pump pulse induces a refractive index profile in the sample that follows the spatial profile of that incident laser beam. If the probe beam spot size on the sample is made significantly smaller than the spot size of the pump beam, the probe will see a refractive index gradient if positioned off-center with respect to the pump spot on the sample. If the sample is optically thin, i.e. $L << z_0$ and the nonlinear phase shift is small, $\Delta\Phi << 1$, the deflection angle of the probe can be written as [84]

$$\theta(x,y,t) = \int_0^L \nabla n(x,y,t) dz, \tag{3.25}$$

where $n(x,y,t)$ is the spatially and time-dependent refractive index as experienced by the probe beam that initially propagates along the z-direction. For a small angle ($< 5°$) between pump and probe, this expression can be approximated by $\theta \approx \nabla n(x,y,t)L$ [84]. For the case of a Gaussian beam, the spatial and temporal profile of the induced refractive index change is

$$\Delta n(x,y,t) = \Delta n_0(t) \exp\left(-\frac{2(x^2+y^2)}{w_{0,pu}^2}\right), \tag{3.26}$$

with $\Delta n_0(t)$ being the time-dependent, on-axis nonlinear refractive index change and $w_{0,pu}$ the Gaussian beam width of the pump. When positioning the probe spot on the sample in a way that it experiences the largest refractive index gradient, which corresponds to $x = 0$ and $y = w_{0,pu}/2$ assuming the pump spot center is at $x = 0$ and $y = 0$, the deflection angle of the probe is [84]

$$\theta(t) = \frac{2L}{w_{0,pu}\sqrt{e}} \Delta n_0(t). \tag{3.27}$$

The deflection of the probe beam can be detected by a segmented detector as shown in Fig. 3.5(b) and (c). The instantaneous power change on the segmented detector can be calculated as [84]

$$\Delta P(t-\tau) \approx P(t-\tau) k_{0,pr} L \sqrt{\frac{2}{e}} \frac{w_{pr}}{w_{pu}} \frac{2}{\sqrt{\pi}} \Delta n_0(t), \tag{3.28}$$

where $k_{0,pr}$ and $w_{0,pr}$ are the wavenumber and the Gaussian beam width of the probe, respectively, and τ is the delay between pump and probe pulse. The segmented photodiode will only detect the time-integrated signal as a function of τ which is [84]

$$\frac{\Delta E(\tau)}{E} = \frac{\int_{-\infty}^{\infty} \Delta P(t-\tau) dt}{\int_{-\infty}^{\infty} P(t) dt} = k_{0,pr} L \sqrt{\frac{2}{e}} \frac{w_{pr}}{w_{pu}} \frac{2}{\sqrt{\pi}} <\Delta n_0(\tau)>. \tag{3.29}$$

$<\Delta n_0(\tau)>$ contains the information about the refractive index response function $R(t)$ of the sample according to [83]

$$<\Delta n_0(\tau)> = \frac{\int_{-\infty}^{\infty} \Delta n_0(t) I_{pr}(t-\tau) dt}{\int_{-\infty}^{\infty} I_{pr}(t) dt} = \frac{\int_{-\infty}^{\infty} \int_{-\infty}^{\infty} R(t-t') I_{pu}(t') dt' I_{pr}(t-\tau) dt}{\int_{-\infty}^{\infty} I_{pr}(t) dt}. \tag{3.30}$$

$I_{pu}(t)$ and $I_{pr}(t)$ are the peak irradiances of pump and probe pulses at the sample position, respectively. If processes contribute to the nonlinear refractive index that do not occur instantaneously on the time scale of the laser pulse, an effective nonlinear refractive index $n_{2,eff}$, that is temporally averaged over the pulse length of a single probe beam, with its envelope of the on-axis irradiance being $I_0(t)$, can be calculated as [83],

$$n_{2,eff} = \frac{\int_{-\infty}^{\infty}\int_{-\infty}^{\infty} R(t-t')I_0(t')dt' I_0(t)dt}{\int_{-\infty}^{\infty} I_0^2(t)dt}. \tag{3.31}$$

Equation 3.31 can be used to compare the results of beam deflection measurements to Z-scan measurements (Eq. 3.31), with $<\Delta n_0(t)> = n_{2,eff} I_0$ and I_0 being the peak on-axis irradiance of the pulse.

It should be noted that the beam deflection method is even more sensitive to nonlinear wavefront distortions than Z-scan, particularly because lock-in detection can be applied by chopping the pump beam and detecting the probe beam. In Ref. [84], a sensitivity of around $\lambda/20,000$ has been reported. Furthermore, if nonlinear absorption changes are present in the sample, the nonlinear refraction can still be obtained by recording simultaneously the sum signal of the segmented detector and normalizing the deflection signal as described in Ref. [15].

Chapter 4

Frequency-modulated combs and SWIFTS

4.1 Frequency combs and frequency-modulated combs

In a laser, the resonator and the gain medium impose the frequencies at which it can lase. While the gain medium alone emits spontaneously into a broad continuous spectrum, the resonator splits the spectrum into a series of lines with approximately equidistant frequency spacing. This longitudinal frequency spacing is given by the inverse of the round-trip time T_R according to

$$\Delta f_L = \frac{1}{T_R} = \frac{c_0}{2L}, \tag{4.1}$$

where L is the optical cavity length. Due to dispersion, L is, in general, frequency-dependent which results in non-equidistance of the longitudinal modes as illustrated in Fig. 4.1(a).

While the cavity length dictates the frequency spacing of the laser emission, the cavity loss determines the spectral width of the resonances. This is characterized by the finesse defined as [79]

$$\mathcal{F} = \frac{\Delta f_L}{\delta f}, \tag{4.2}$$

with δf being the full width at half maximum (FWHM) of the cavity mode resonance. The finesse can be calculated from the cavity losses by [79]

$$\mathcal{F} = \frac{\pi R}{1 - R^2}, \tag{4.3}$$

where R is the combined power reflectivity of the mirrors and all other losses are neglected. For a typical VECSEL cavity with a length of about 10 cm and a reflectivity of 99%, one obtains a finesse of about 156 and consequently a FWHM of the cavity mode of around 9.6 MHz with a longitudinal mode spacing $\Delta f_L \approx 1.5$ GHz.

If the intracavity dispersion is not too large, the laser spectrum already resembles a comb, the spacing of which is imposed by Eq. 4.1. However, in order to achieve truly equidistant laser lines, it is necessary that the different longitudinal laser modes are phase-locked with respect to each other. This requires a coupling mechanism which can be realized by a saturable absorber or a four-wave-mixing (FWM) nonlinearity in the gain medium. The coupling will lead to the longitudinal laser modes being pulled away from the maximum of the cavity mode resonance where they would emit in the free-running case. This scenario is depicted in Fig. 4.1(b).

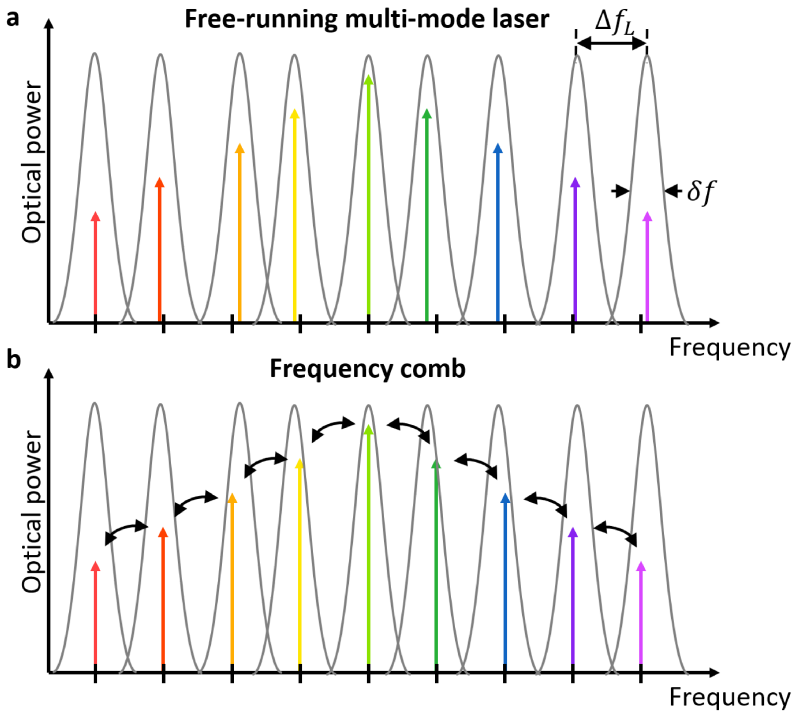

Figure 4.1: (a) Free-running multi-mode laser for which the mode spacing is not equidistant. The grey envelopes around the laser modes illustrate the cavity resonances with a FWHM of δf. (b) Frequency comb with equidistant laser modes achieved through coupling of the laser modes. The equidistance is visualized by the alignement of the laser modes with respect to the equidistant grid on the x-axis. Figure inspired by Ref. [85]

Historically, frequency combs were based on ultrashort-pulsed lasers. Particularly, the active stabilization of offset and repetition frequency of such lasers enabled unprecedented measurement abilities and control of optical frequencies [86]. In ultrashort-pulsed lasers, the comb-like spectrum can be understood by considering that the Fourier transform of a regularly spaced, short time signal, which, in the idealized case, corresponds to an infinite sequence of equally spaced Dirac delta functions, also in the frequency domain leads to an infinite sequence of equally spaced Dirac delta functions, i.e. a comb [87].

The paradigm that a frequency comb intrinsically requires a short-pulsed laser was overthrown by the demonstration of frequency comb generation in an ultra-high-Q microresonator in 2007 [88]. There, the Kerr nonlinearity of the material leads to parametric side band generation of the initially injected pump signal at a single frequency. The phase-locking due to FWM is sufficiently strong to overcome the dispersion of the resonator. In general, no short pulses are emitted. However, if the cavity dispersion is appropriately engineered and an appropriate pump laser detuning is chosen, the formation of temporal solitons can occur. [89].

In 2012, frequency comb formation was also demonstrated in a mid-infrared quantum cascade laser (QCL) [18]. Also here, comb formation was attributed to FWM. However, in this case, FWM is based on resonant intersubband transitions, which leads to a very large third-order nonlinearity while in the above-mentioned microresonators, FWM is based on the ultrafast bound-electronic Kerr effect of the resonator material.

The coupling mechanism in resonant FWM can be understood by considering the intermode beating of adjacent modes. The intermode beating will lead to a modulation of the instantaneous intensity in the laser cavity at the intermode frequency which corresponds to Δf_L in the case of nearest neighbors. This will make the population inversion of the gain medium oscillate with frequency f_L [90]. Subsequently, the oscillation of the gain medium will affect all mode pairs. Therefore, it provides a coupling mechanism between different modes. Mode pairs with an initially slightly different frequency spacing will thus synchronize. This corresponds to the situation of multiple coupled oscillators which will synchronize even if they have slightly different eigenfrequencies [17].

The resonant nature of the FWM in semiconductor lasers leads to a non-negligible delay of the coupling mechanism. As a consequence, the phase relation between adjacent modes will be constant over time but not zero. More specifically, it turns out that in most cases of frequency comb formation by FWM in semiconductor lasers the phase difference between adjacent modes (intermode phase) varies linearly over 2π over the laser spectrum [17, 42]. Consequently, the phase profile will be parabolic over the laser spectrum leading to a linearly chirped or frequency-modulated (FM) output in the time domain while the intensity will not vary significantly. In fact, in such kind of FM regime, intensity fluctuations are suppressed while, in the amplitude-modulated (AM) regime, intensity fluctuations are maximized, with the intermode phase being close to zero. The properties of the AM and FM regime are thus simply a result of different intermode phases between adjacent modes. This can be visualized, in the spirit of a

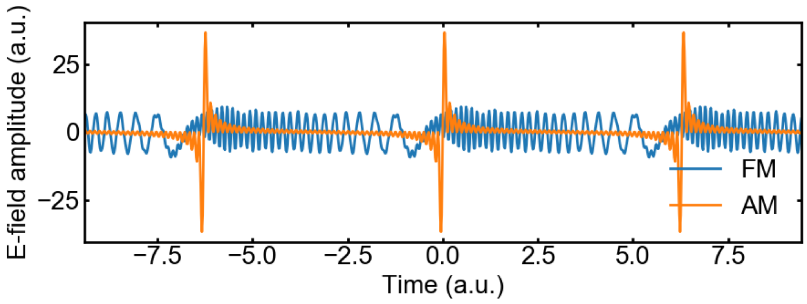

Figure 4.2: Visualization of frequency-modulated (FM) and amplitude-modulated (AM) output of a laser by adding up numerically 50 sine functions with equal amplitude according to Eq. 4.4.

Fourier series, by adding up sine functions with increasing frequency according to

$$\sum_{n=1}^{N} \sin(n\omega_0 + \varphi_n). \tag{4.4}$$

In the AM regime, $\varphi_n = 0$, and, in the FM regime, $\varphi_n = \sum_j^n j2\pi/N$.

Figure 4.2 shows the result of numerically adding up $N = 50$ sine functions according to Eq. 4.4 for both the AM and the FM regime. The envelope of the FM waveform is nearly constant while the instantaneous frequency of the fast oscillation varies strongly. In the AM regime, the behavior reverses, with the instantaneous frequency being nearly constant while the envelope periodically exhibits a strong peak.

There is significant and on-going activity in modeling FM comb formation in semiconductor lasers to obtain a better understanding of what are the key ingredients that enable it to form [22, 23, 46, 91]. These modeling efforts usually depart from the optical Bloch equations with the laser medium being modeled as a two-level system. This leads to a system of coupled differential equations which correctly reproduces the experimental behavior including the non-zero intermode phase being linearly spread over 2π [22]. For a more intuitive understanding of the physics behind FM comb formation, this system of coupled differential equations has been reduced to a master equation for the phase and electric field amplitude, respectively [22]. From this analysis, it has been concluded that the essential ingredients for FM comb formation are the existence of spatial hole burning that enables multi-mode operation, as well as a GDD, the value of which should not completely compensate the resonant Kerr nonlinearity to enable the build-up of the linear chirp.

Even more interestingly, it has been shown that, for a Fabry-Pérot cavity with large mirror losses, the whole physics of comb generation can be captured by a single equation analogous to the nonlinear Schrödinger equation (NLSE) that describes soliton formation [23]. However, in contrast to the conventional NLSE , the Kerr nonlinearity is replaced by a term proportional to the phase of the electric field. This leads to an analytical steady state solution the amplitude of which is constant while the phase depends quadratically on time, resulting in a linear frequency chirp. Such results show that FM combs constitute a similar universal operation regime in semiconductor lasers than solitons do in conventionally mode-locked lasers or high-Q microresonators.

While FM combs have initially only been observed in edge-emitting Fabry-Pérot lasers, recently also FM comb formation in QCL ring lasers has been observed [92, 93]. With ring lasers lacking both high mirror losses as well as efficient spatial hole burning, its cause has been attributed to the interplay of a strong linewidth enhancement factor (LEF) and group velocity dispersion which can be described by the complex Ginzburg-Landau equation [93]. Even more intriguingly, comb formation in QCL ring lasers offers the prospect to generate ultrashort pulses in form of dissipative Kerr solitons in the mid-infrared, which has been elusive for decades [94]. Very recently, this has been demonstrated experimentally [95].

In this context, it is exciting to consider the possibility of generating FM combs in VECSELs, considering that they are quite distinct from QCLs and diode lasers in that they are optically pumped, have a high-Q cavity and an external cavity. As demonstrated in Ref. [21], and as part of this thesis, it is indeed possible to observe FM comb behavior in VECSELs. Future research should investigate how the coherent comb spectrum can be made broader as well as potentially investigate whether dissipative Kerr solitons could also be generated in appropriately dispersion-engineered VECSELs, which would constitute a new and innovative way of self-mode-locking.

The advances in understanding and improving the properties of FM combs have largely been made possible by the invention of a new measurement technique, called shifted-wave-interference Fourier-transform spectroscopy (SWIFTS), that measures the intermode phase, even in the absence of short pulses [20]. This is the subject of the next section.

4.2 Shifted-wave-interference Fourier-transform spectroscopy (SWIFTS)

Traditionally, the investigation of coherent laser emission relies on nonlinear optical processes such as second harmonic generation in autocorrelation or frequency-resolved optical gating (FROG) [64]. There, it is exploited that a small or zero intermode phase leads to pulsed emission with high peak powers that can be efficiently converted into a second-harmonic signal. However, in general, these nonlinear methods cannot be applied to FM combs that have nearly constant intensity over time. Therefore, techniques with a linear detection scheme have to be used. In the first demonstration of a FM comb in a QCL, beatnote spectroscopy based on a Fourier-transform infrared spectrometer (FTIR) has been used to demonstrate phase stability of the laser modes [18]. In this approach, the fundamental beatnote is detected by a fast photodetector and spectrally resolved by scanning one arm of the FTIR and Fourier-transforming the resulting interferogram. When the resulting spectrum matches exactly the normal laser spectrum obtained with a slow photodiode and a FTIR, the laser emits phase-stable (coherent) light. A characteristic signature of FM combs is that the interferogram obtained with the fast photodetector exhibits a minimum at zero delay while the interferogram recorded with a slow detector always shows a maximum at zero delay.

It is possible to go even further and also spectrally resolve the intermode phases from a similar kind of measurement that is called shifted-wave-interference Fourier-transform

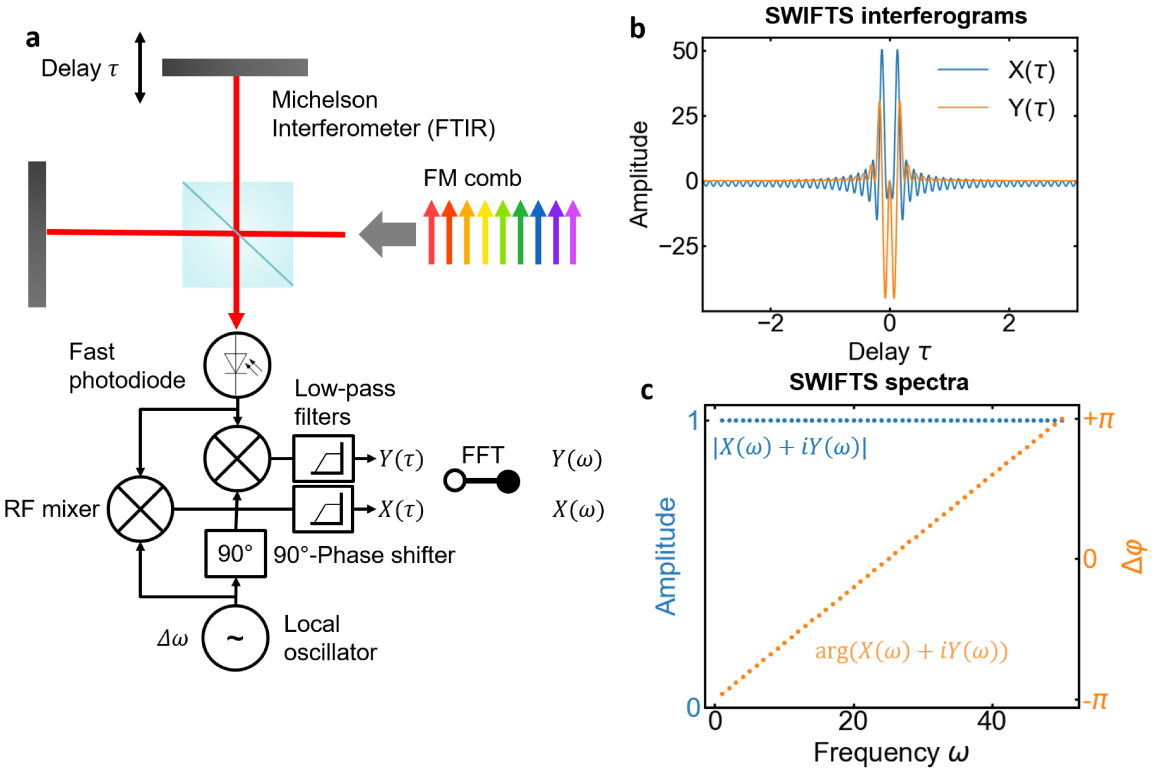

Figure 4.3: Principle of SWIFTS measurement. (a) SWIFTS setup consisting of a Michelson interferometer and an electronic phase sensitive detection unit yielding the two interferograms $X(\tau)$ and $Y(\tau)$ as shown in (b). These are the two SWIFTS interferograms calculated from the FM signal of Fig. 4.2. (c) Amplitude and intermode phase spectrum of combined and Fourier-transformed SWIFTS interferograms of (b). Note that the local oscillator operates at the frequency $\Delta\omega$ which corresponds to the mode-spacing of adjacent modes and can be retrieved by an additional beatnote measurement in front of the interferometer as done in Ref. [21].

spectroscopy (SWIFTS) [20]. Its principle is displayed in Fig. 4.3. Here, one performs phase sensitive detection of the laser signal recorded with a fast photodiode at the output of the Michelson interferometer. To understand the working principle, one writes the electric field of the comb-like laser emission as [21]

$$E(t) = \sum_n E_n e^{i(\omega_n t + \varphi_n)} + c.c, \tag{4.5}$$

with E_n being the electric field amplitude, φ_n the phase and ω_n the frequency of mode n. It can be shown that the two interferograms recorded as a function of the interferometer delay τ at the output of the signal processing chain are [21][1]

$$X(\tau) = \sum_n E_{n+1} E_n \cos(\varphi_{n+1} - \varphi_n) \left(1 + \cos(\omega_0 \tau) + 2\cos(\omega_n \tau)\right), \tag{4.6a}$$

$$Y(\tau) = \sum_n E_{n+1} E_n \sin(\varphi_{n+1} - \varphi_n) \left(1 + \cos(\omega_0 \tau) + 2\cos(\omega_n \tau)\right). \tag{4.6b}$$

Here, ω_0 is the frequency of the local oscillator used to mix down the beat signal at $\omega_{n+1} - \omega_n$ and, for the case of a comb, is (chosen) equal to it. In Fig. 4.3(b) these functions are plotted for the FM signal of Fig. 4.2, i.e. with 50 modes of unity amplitude and an intermode phase that is linearly distributed over 2π over the laser spectrum as shown in Fig. 4.3(c). One sees that both interferograms go to zero at zero delay, which can be intuitively understood by considering that at $\tau = 0$ one sums up phasors that are equally spread over the unit circle in the complex plane, thus canceling each other out (see also Eq. 4.7). In order to retrieve the intermode phase, one adds up the two interferograms in Eqs. 4.6 and obtains

$$X(\tau) + iY(\tau) = \sum_n E_{n+1} E_n e^{i(\varphi_{n+1} - \varphi_n)} \left(1 + \cos(\omega_0 \tau) + 2\cos(\omega_n \tau)\right). \tag{4.7}$$

It can be easily seen now that the argument of the Fourier transform of Eq. 4.7 yields the spectrally resolved intermode phase $\Delta\varphi_n = \varphi_{n+1} - \varphi_n$. Its absolute value corresponds to the normal intensity spectrum if it is a perfect equidistant comb as can be seen by comparing Eq. 4.7 to the normal intensity interferogram, [21]

$$I(\tau) = \sum_n 2E_n^2 \left(1 + \cos(\omega_n \tau)\right), \tag{4.8}$$

and considering only the term proportional to $\cos(\omega_n \tau)$.

Furthermore, it is interesting to consider what happens when the SWIFTS measurement is confronted with an incoherent comb, i.e. a laser whose modes are not equidistant and phase stable. It can be shown that the coherence amplitude, which is the absolute value of the Fourier transform of Eq. 4.7 divided by the absolute value of the Fourier transform of the intensity interferogram, can approximately be written as [96]

$$g(\omega_n) = \frac{|X(\omega_n) + iY(\omega_n)|}{I(\omega_n)} = \mathrm{sinc}\left(\frac{T}{2}(\omega_{n+1} - \omega_n - \omega_0)\right). \tag{4.9}$$

[1] Note that Eqs. (S6a) and (S6b) in the supplement of Ref. [21] contain an error. Eqs. 4.6 are the correct expressions for the SWIFTS interferograms.

Here, T is the total measurement time, assuming that the arm of the Michelson interferometer is scanned with an approximately constant velocity. One sees that Eq. 4.9 is unity for perfect equidistance, $\omega_{n+1} - \omega_n = \omega_0$. Eq. 4.9 becomes zero when $f_{n+1} - f_n - f_0 = \frac{m}{T}$, where m is an integer but not zero. This means that when $g(\omega_n)$ is close to one, equidistance of the comb lines in the order of the inverse of the measurement time is guaranteed. For a measurement time of one minute, this only allows possible equidistance variations of less than 1 Hz.

In principle, SWIFTS can also be used to measure the pulse width and chirp of ultrashort pulses. However, as is shown in Ref. [96], the SNR of the measurement usually reduces for very short pulses lengths (< 1 ps) and small repetition rates (MHz). Therefore, SWIFTS is best suited for characterization of laser sources with GHz repetition rates and emission of FM combs or long pulses.

Chapter 5

Summary and outlook

In this thesis, two aspects of self-mode-locking of VECSELs are investigated. Here, self-mode-locking refers to the emergence of phase stability (coherence) of longitudinal laser modes due to intrinsic nonlinear optical processes in the gain chip, in contrast to conventional mode-locking which uses an additional device (SESAM) to obtain such kind of coherence.

The first aspect concerns the investigation of nonlinear lensing in the gain chip that has been assumed to be responsible for manifold self-mode-locking demonstrations in VECSELs, particularly when a slit inserted into the cavity appeared to be important. In chapter 3, a review of previous and ongoing investigations of nonlinear refractive index changes, that determine the strength of nonlinear lensing, is provided, both for VECSELs and SOAs, with the physics of the latter devices being comparable to VECSELs. Consequently, in chapter 3, the intracavity beam width modulation for two kind of VECSEL cavities is theoretically examined. It is shown that in a linear cavity operated close to its stability limit a beam-width modulation of a few percents can be achieved, with a nonlinear refractive index in the order of 10^{-15} m^2/W. In contrast, in a Z-cavity similar to how it is used in Ref. [9] the beam width-modulation only amounts to a few permille which makes a Kerr-lens mode-locking scenario less plausible.

The main contribution of this thesis towards a better understanding of whether Kerr-lens mode-locking of VECSELs is possible, is to provide a comprehensive characterization of the effective nonlinear refractive index of a VECSEL chip. For this purpose, two measurement techniques, Z-scan and ultrafast beam deflection, described in chapter 3, are employed.

As part of this thesis, Refs. [13–15] present nonlinear refractive index characterizations of VECSEL gain chips as a function of the probe wavelength, the excitation fluence and the pulse width (which is calculated from time-resolved measurements). The main results are that the effective nonlinear refractive index is negative and in the order of 10^{-16} m^2/W for low excitation fluences and short (sub-ps) pulse lengths but increases strongly and becomes positive for large pulse lengths (>1 ps) and large excitation fluences. As detailed in Ref. [15], these findings are consistent with some self-mode-locking demonstrations. However, while the effect of nonlinear lensing probably can trigger spontaneous pulse formation in VECSELs when the cavity is designed appropriately, it remains to be seen whether such kind of mode-locking is competitive compared to conventional SESAM mode-locking, both with respect to stability and pulse properties.

The second aspect of self-mode-locking in VECSELs that has been explored in this thesis is the generation of FM combs. These states of light have first been observed in QCLs and have been shown to be a fundamental operation regime of semiconductor lasers, similar to solitons in mode-locked lasers and microresonators. They are characterized by a linear frequency chirp that originates from the intermode phases being splayed over 2π. The invention of SWIFTS has been crucial for the detection and investigation of FM combs. It allows the direct measurement of the intermode phases and provides a measure of coherence. In Ref. [21], which is part of this thesis, SWIFTS is used to investigate the FM comb properties of a VECSEL. It is shown that comb-like light is emitted the intermode phases of which span exactly 2π over the laser spectrum as expected for a FM comb. These findings challenge previous assumptions that FM combs can only be generated in Fabry-Pérot cavities with strong spatial hole burning and high mirror losses. However, also the recent discovery of FM comb generation in QCL ring lasers has shown that this does not necessarily have to be the case and the quest for a better theoretical understanding of this complex spatiotemporal phenomenon is still ongoing. The most exciting development in this context is probably to go from a FM comb regime to a regime where dissipative Kerr solitons are generated which has recently been demonstrated in a ring QCL [95]. Such schemes might also open up new avenues for ultrashort pulse generation in VECSELs.

From an application point of view, FM combs in VECSELs might prove useful for dual-comb spectroscopy. Indeed, dual-comb spectroscopy with a single mode-locked VECSEL has already been demonstrated (see Ref. [5]) and it can be expected that this works also well for VECSEL FM combs. Thus, the future looks bright for comb applications which require high-power, compact and wavelength-flexible laser sources that VECSELs are.

Bibliography

[1] A. Rahimi-Iman. "Recent advances in VECSELs". *Journal of Optics* 18 (2016), p. 093003.

[2] M. Guina, A. Rantamäki, and A. Härkönen. "Optically pumped VECSELs : review of technology and progress". *Journal of Physics D: Applied Physics* 50 (2017), p. 383001.

[3] M. A. Gaafar, A. Rahimi-Iman, K. A. Fedorova, W. Stolz, E. U. Rafailov, and M. Koch. "Mode-locked Semiconductor Disk Lasers". *Advances in Optics and Photonics* 8 (3) (2016), pp. 370–400.

[4] F. F. Voigt, F. Emaury, P. Bethge, D. Waldburger, S. M. Link, S. Carta, A. van der Bourg, F. Helmchen, and U. Keller. "Multiphoton in vivo imaging with a femtosecond semiconductor disk laser". *Biomedical Optics Express* 8 (7) (2017), pp. 3213–3231.

[5] S. M. Link, D. J. H. C. Maas, D. Waldburger, and U. Keller. "Dual-comb spectroscopy of water vapor with a free-running semiconductor disk laser". *Science* 356 (6343) (2017), pp. 1164–1168.

[6] Y. F. Chen, Y. C. Lee, H. C. Liang, K. Y. Lin, K. W. Su, and K. F. Huang. "Femtosecond high-power spontaneous mode-locked operation in vertical-external cavity surface-emitting laser with gigahertz oscillation". *Optics Letters* 36 (23) (2011), pp. 4581–4583.

[7] L. Kornaszewski, G. Maker, G. P. Malcolm, M. Butkus, E. Rafailov, and C. J. Hamilton. "SESAM-free mode-locked semiconductor disk laser". *Laser and Photonics Review* 6 (2012), pp. 20–23.

[8] A. R. Albrecht, Y. Wang, M. Ghasemkhani, D. V. Seletskiy, J. G. Cederberg, and M. Sheik-Bahae. "Exploring ultrafast negative Kerr effect for mode-locking vertical external-cavity surface-emitting lasers". *Optics Express* 21 (23) (2013), pp. 28801–28808.

[9] M. Gaafar, P. Richter, H. Keskin, C. Möller, M. Wichmann, W. Stolz, A. Rahimi-Iman, and M. Koch. "Self-mode-locking semiconductor disk laser". *Optics Express* 22 (23) (2014), pp. 28390–28399.

[10] R Bek, M Großmann, H Kahle, M Koch, A Rahimi-Iman, M Jetter, and P Michler. "Self-mode-locked AlGaInP-VECSEL". *Applied Physics Letters* 111 (2017), p. 182105.

[11] K. G. Wilcox and A. C. Tropper. "Comment on SESAM-free mode-locked semiconductor disk laser". *Laser and Photonics Reviews* 423 (3) (2013), pp. 422–423.

[12] E. Escoto and G. Steinmeyer. “Pseudo Mode-Locking”. *Proc. SPIE 11263, Vertical External Cavity Surface Emitting Lasers (VECSELs) X* 11263 (2020), pp. 1–3.

[13] C. Kriso, S. Kress, T. Munshi, M. Großmann, R. Bek, M. Jetter, P. Michler, W. Stolz, M. Koch, and A. Rahimi-Iman. “Microcavity-enhanced Kerr nonlinearity in a vertical-external-cavity surface-emitting laser”. *Optics Express* 27 (9) (2019), pp. 11914–11929.

[14] C. Kriso, S. Kress, T. Munshi, M. Grossmann, R. Bek, M. Jetter, P. Michler, W. Stolz, M. Koch, and A. Rahimi-Iman. “Wavelength and Pump-Power Dependent Nonlinear Refraction and Absorption in a Semiconductor Disk Laser”. *IEEE Photonics Technology Letters* 32 (2) (2020), pp. 85–88.

[15] C. Kriso, T. Bergmeier, N. Giannin, A. R. Albrecht, M. Sheik-Bahae, S. Benis, S. Faryadras, E. W. Van Stryland, D. J. Hagan, M. Koch, G. Mette, and A. Rahimi-Iman. “Probing the ultrafast gain and refractive index dynamics of a VECSEL”. *arXiv:2106.13664* (2021).

[16] A. Rahimi-Iman, M. Gaafar, C. Möller, M. Vaupel, F. Zhang, D. Al-nakdali, K. A. Fedorova, W. Stolz, E. U. Rafailov, and M. Koch. “Self-Mode-Locked Vertical-External-Cavity Surface-Emitting Laser”. *Proc. SPIE 9734, Vertical External Cavity Surface Emitting Lasers (VECSELs) VI, 97340M.* 2016.

[17] J. Hillbrand, D. Auth, M. Piccardo, N. Opacak, G. Strasser, F. Capasso, S. Breuer, and B. Schwarz. “In-phase and anti-phase synchronization in a laser frequency comb”. *Physical Review Letters* 124 (2019), p. 023901.

[18] A. Hugi, G. Villares, S. Blaser, H. C. Liu, and J. Faist. “Mid-infrared frequency comb based on a quantum cascade laser”. *Nature* 492 (7428) (2012), pp. 229–233.

[19] G. Villares, A. Hugi, S. Blaser, and J. Faist. “Dual-comb spectroscopy based on quantum-cascade-laser frequency combs”. *Nature Communications* 5 (2014), p. 5192.

[20] D. Burghoff, Y. Yang, D. J. Hayton, J.-R. Gao, J. L. Reno, and Q. Hu. “Evaluating the coherence and time-domain profile of quantum cascade laser frequency combs”. *Optics Express* 23 (2) (2015), pp. 1190–1202.

[21] C. Kriso, A. Barua, O. Mohiuddin, C. Möller, A. Ruiz-Perez, W. Stolz, M. Koch, and A. Rahimi-Iman. “Signatures of a frequency-modulated comb in a VECSEL”. *Optica* 8 (4) (2021), pp. 458–463.

[22] N. Opačak and B. Schwarz. “Theory of frequency modulated combs in lasers with spatial hole burning, dispersion and Kerr nonlinearity”. *Physical Review Letters* 123 (2019), p. 243902.

[23] D. Burghoff. “Unraveling the origin of frequency modulated combs using active mean-field theory”. *Optica* 7 (12) (2020), pp. 1781–1787.

[24] M. Piccardo et al. “Roadmap on multimode light shaping”. *arXiv:2104.03550* (2021).

[25] V. Torres-Company, J. Schröder, A. Fülöp, M. Mazur, L. Lundberg, B. Helgason, Óskar, M. Karlsson, and P. A. Andrekson. "Laser Frequency Combs for Coherent Optical Communications". *Journal of Lightwave Technology* 37 (7) (2019), pp. 1163–1670.

[26] C. L. Hoy, O. Ferhanoğlu, M. Yildirim, K. H. Kim, S. S. Karajanagi, K. M. C. Chan, J. B. Kobler, S. M. Zeitels, and A. Ben-Yakar. "Clinical ultrafast laser surgery: Recent advances and future directions". *IEEE Journal on Selected Topics in Quantum Electronics* 20 (2) (2014).

[27] K. Sugioka and Y. Cheng. "Ultrafast lasers-reliable tools for advanced materials processing". *Light: Science and Applications* 3 (390) (2014), pp. 1–12.

[28] *The Nobel Prize in Physics 2005. NobelPrize.org. Nobel Media AB 2021. Wed. 19 May 2021.*

[29] *The Nobel Prize in Physics 2018. NobelPrize.org. Nobel Media AB 2021. Tue. 18 May 2021.*

[30] *https://www.businesswire.com/news/home/20210301005392/en/14.53-Billion-Semiconductor-Lasers-Market—Global-Opportunity-Analysis-and-Industry-Forecast-to-2030—ResearchAndMarkets.com (accessed 19.05.2021).*

[31] M. Kuznetsov, F. Hakimi, R. Sprague, and A. Mooradian. "High-power (>0.5-W CW) diode-pumped vertical-external-cavity surface-emitting semiconductor lasers with circular TEM_{00} beams". *IEEE Photonics Technology Letters* 9 (8) (1997), pp. 1063–1065.

[32] S Hoogland, S Dhanjal, A. C. Tropper, J. S. Roberts, R Häring, R Paschotta, and U Keller. "Passively Mode-Locked Diode-Pumped Surface-Emitting Semiconductor Laser". *IEEE Photonics Technology Letters* 12 (9) (2000), pp. 1135–1137.

[33] D. Waldburger, S. M. Link, M. Mangold, C. G. E. Alfieri, E. Gini, M. Golling, B. W. Tilma, and U. Keller. "High-power 100 fs semiconductor disk lasers". *Optica* 3 (8) (2016), pp. 844–852.

[34] A. Laurain, I. Kilen, J. Hader, A. R. Perez, P. Ludewig, W. Stolz, G. Balakrishnan, S. W. Koch, and J. V. Moloney. "Modeling and experimental realization of modelocked VECSEL producing high power sub-100 fs pulses". *Applied Physics Letters* 113 (2018), p. 121113.

[35] I. Kilen, S. W. Koch, J. Hader, and J. Moloney. "Non-equilibrium ultrashort pulse generation strategies in VECSELs". *Optica* 4 (4) (2017), pp. 412–417.

[36] I. Kilen, J. Hader, J. V. Moloney, and S. W. Koch. "Ultrafast nonequilibrium carrier dynamics in semiconductor laser mode locking". *Optica* 1 (4) (2014), pp. 192–197.

[37] S. Addamane, D. Shima, A. Laurain, H.-T. Chan, G. Balakrishnan, and J. V. Moloney. "Degradation mechanism of SESAMs". *Proc. SPIE 10515, Vertical External Cavity Surface Emitting Lasers (VECSELs) VIII* (2018).

[38] A. H. Quarterman, M. A. Tyrk, and K. G. Wilcox. "Z-scan measurements of the nonlinear refractive index of a pumped semiconductor disk laser gain medium". *Applied Physics Letters* 106 (2015), p. 011105.

[39] E. A. Shaw, A. H. Quarterman, A. P. Turnbull, T. Chen Sverre, C. R. Head, A. C. Tropper, and K. G. Wilcox. "Nonlinear Lensing in an Unpumped Antiresonant Semiconductor Disk Laser Gain Structure". *IEEE Photonics Technology Letters* 28 (13) (2016), pp. 1395–1398.

[40] A. H. Quarterman, S. Mirkhanov, C. J. Smyth, and K. G. Wilcox. "Measurements of nonlinear lensing in a semiconductor disk laser gain sample under optical pumping and using a resonant femtosecond probe laser". *Applied Physics Letters* 109 (2016), p. 121113.

[41] D. Burghoff, T. Y. Kao, N. Han, C. W. I. Chan, X. Cai, Y. Yang, D. J. Hayton, J. R. Gao, J. L. Reno, and Q. Hu. "Terahertz laser frequency combs". *Nature Photonics* 8 (6) (2014), pp. 462–467.

[42] M. Singleton, P. Jouy, M. Beck, and J. Faist. "Evidence of linear chirp in mid-infrared quantum cascade lasers". *Optica* 5 (8) (2018), pp. 948–953.

[43] I. Coddington, N. Newbury, and W. Swann. "Dual-comb spectroscopy". *Optica* 3 (4) (2016), pp. 414–426.

[44] J. Hillbrand, M. Beiser, A. M. Andrews, H. Detz, R. Weih, A. Schade, S. Höfling, G. Strasser, and B. Schwarz. "Picosecond pulses from a mid-infrared interband cascade laser". *Optica* 6 (10) (2019), pp. 1334–1337.

[45] L. A. Sterczewski, C. Frez, S. Forouhar, and D. Burghoff. "Frequency-modulated diode laser frequency combs at 2 m wavelength Frequency-modulated diode laser frequency combs at 2 μ m wavelength". *APL Photonics* 5 (2020), p. 076111.

[46] M. Dong, S. T. Cundiff, and H. G. Winful. "Physics of frequency-modulated comb generation in quantum-well diode lasers". *Physical Review A* 97 (2018), p. 053822.

[47] B. Heinen, T.-L. Wang, M. Sparenberg, A. Weber, B. Kunert, J. Hader, S. Koch, J. Moloney, M. Koch, and W. Stolz. "106 W continuous-wave output power from vertical-external-cavity surface-emitting laser". *Electronics Letters* 48 (2012), pp. 516–517.

[48] T. Germann, A. Strittmatter, J. Pohl, U. W. Pohl, D. Bimberg, J Rautiainen, M. Guina, and O. G. Okhotnikov. "Temperature-stable operation of a quantum dot semiconductor disk laser". *Applied Physics Letters* 051104 (2008), pp. 1–4.

[49] M. Butkus, K. G. Wilcox, J. Rautiainen, O. G. Okhotnikov, S. S. Mikhrin, I. L. Krestnikov, A. R. Kovsh, M. Hoffmann, T. Südmeyer, U. Keller, and E. U. Rafailov. "High-power quantum-dot-based semiconductor disk laser". *Optics Letters* 34 (11) (2009), pp. 1672–1674.

[50] B. Heinen, F. Zhang, M. Sparenberg, B. Kunert, M. Koch, and W. Stolz. "On the Measurement of the Thermal Resistance of Vertical-External-Cavity Surface-Emitting Lasers (VECSELs)". *IEEE Journal of Quantum Electronics* 48 (7) (2012), pp. 934–940.

[51] A. C. Tropper and S Hoogland. "Extended cavity surface-emitting semiconductor lasers". *Progress in Quantum Electronics* 30 (2006), pp. 1–43.

[52] C. Möller. “Fundamental analysis and optimization of barrier-pumped GaAs-based VECSELs”. Dissertation. Philipps-Universität Marburg, 2016.

[53] M. DiDomenico. “Small-Signal Analysis of Internal (Coupling-Type) Modulation of Lasers”. *Journal of Applied Physics* 35 (10) (1964), pp. 2870–2876.

[54] L. E. Hargrove, R. L. Fork, and M. A. Pollack. “Locking of HeNe laser modes induced by synchronous intracavity modulation”. *Applied Physics Letters* 5 (1) (1964), pp. 4–5.

[55] A. Yariv. “Internal Modulation in Multimode Laser Oscillations”. *Journal of Applied Physics* 36 (2) (1965), pp. 388–391.

[56] H. A. Haus. “Mode-Locking of Lasers”. *IEEE Journal of Selected Topics in Quantum Electronics* 6 (6) (2000), pp. 1173–1185.

[57] E. Ippen, C. V. Shank, and A. Dienes. “Passive mode locking of the cw dye laser”. *Applied Physics Letters* 21 (8) (1972), pp. 348–350.

[58] U. Keller, D. A. B. Miller, G. D. Boyd, T. H. Chiu, J. F. Ferguson, and M. T. Asom. “Solid-state low-loss intracavity saturable absorber for Nd:YLF lasers: an antiresonant semiconductor Fabry–Perot saturable absorber”. *Optics Letters* 17 (7) (1992), pp. 505–507.

[59] U. Keller, K. J. Weingarten, F. X. Kärtner, D. Kopf, B. Braun, I. D. Jung, R. Fluck, C. Hönninger, N. Matuschek, and J. Aus Der Au. “Semiconductor saturable absorber mirrors (SESAM’s) for femtosecond to nanosecond pulse generation in solid-state lasers”. *IEEE Journal on Selected Topics in Quantum Electronics* 2 (3) (1996), pp. 435–451.

[60] D. E. Spence, P. N. Kean, and W. Sibbett. “60-fsec pulse generation from a self-mode-locked Ti:sapphire laser”. *Optics Letters* 16 (1) (1991), pp. 42–44.

[61] R. Paschotta, R. Häring, A. Garnache, S. Hoogland, A. C. Tropper, and U. Keller. “Soliton-like pulse-shaping mechanism in passively mode-locked surface-emitting semiconductor lasers”. *Applied Physics B: Lasers and Optics* 75 (4-5) (2002), pp. 445–451.

[62] O. D. Sieber, M. Hoffmann, V. J. Wittwer, M. Mangold, M. Golling, B. W. Tilma, T. Südmeyer, and U. Keller. “Experimentally verified pulse formation model for high-power femtosecond VECSELs”. *Applied Physics B: Lasers and Optics* 113 (1) (2013), pp. 133–145.

[63] M. Hoffmann, O. D. Sieber, D. J. H. C. Maas, V. J. Wittwer, M. Golling, T. Südmeyer, and U. Keller. “Experimental verification of soliton-like pulse-shaping mechanisms in passively mode-locked VECSELs”. 18 (10) (2010), pp. 10143–10153.

[64] A. M. Weiner. *Ultrafast Optics*. Ed. by G. Boreman. John Wiley & Sons, Inc., 2009.

[65] C. Koos and W. Freude. “Lecture Notes: Optical Waveguides and Fibers”. 2016.

[66] S. Diddams and J.-C. Diels. “Dispersion measurements with white-light interferometry”. *Journal of the Optical Society of America B* 13 (6) (1996), pp. 1120–1129.

[67] A. Gosteva, M. Haiml, R. Paschotta, and U. Keller. "Noise-related resolution limit of dispersion measurements with white-light interferometers". *Journal of the Optical Society of America B* 22 (9) (2005), pp. 1868–1874.

[68] A. Othonos. "Probing ultrafast carrier and phonon dynamics in semiconductors". *Journal of Applied Physics* 83 (4) (1998), pp. 1789–1830.

[69] D. N. Christodoulides, I. C. Khoo, G. J. Salamo, G. I. Stegeman, and E. W. Van Stryland. "Nonlinear refraction and absorption: mechanisms and magnitudes". *Advances in Optics and Photonics* 2 (2010), pp. 60–200.

[70] H.-C. Liang, Y.-C. Lee, J.-C. Tung, K.-W. Su, K.-F. Huang, and Y.-F. Chen. "Exploring the spatio-temporal dynamics of an optically pumped semiconductor laser with intracavity second harmonic generation". *Optics Letters* 37 (22) (2012), pp. 4609–4611.

[71] C. H. Tsou, H. C. Liang, C. P. Wen, K. W. Su, K. F. Huang, and Y. F. Chen. "Exploring the influence of high order transverse modes on the temporal dynamics in an optically pumped mode-locked semiconductor disk laser". *Optics Express* 23 (12) (2015), pp. 16339–16347.

[72] L. Kornaszewski, G. Maker, G. Malcolm, M. Butkus, E. U. Rafailov, and C. Hamilton. "Reply to comment on SESAM-free mode-locked semiconductor disk laser". *Laser and Photonics Reviews* 7 (4) (2013), pp. 555–556.

[73] M. Gaafar, C. Möller, M. Wichmann, B. Heinen, B. Kunert, A. Rahimi-Iman, W Stolz, and M. Koch. "Harmonic self-mode-locking of optically pumped semiconductor disc laser". *Electronics Letters* 50 (7) (2014), pp. 542–543.

[74] M. Gaafar, D. A. Nakdali, C. Möller, K. A. Fedorova, M. Wichmann, M. K. Shakfa, F. Zhang, A. Rahimi-iman, E. U. Rafailov, and M. Koch. "Self-mode-locked quantum-dot vertical-external-cavity-surface-emitting laser". *Optics Letters* 39 (15) (2014), pp. 4623–4626.

[75] C. T. Hultgren and E. P. Ippen. "Ultrafast refractive index dynamics in AlGaAs diode laser amplifiers". *Applied Physics Letters* 59 (6) (1991), pp. 635–637.

[76] K. L. Hall, A. M. Darwish, E. P. Ippen, U. Koren, and G. Raybon. "Femtosecond index nonlinearities in InGaAsP optical amplifiers". *Applied Physics Letters* 62 (12) (1993), pp. 1320–1322.

[77] J. Mork, A. Mecozzi, and C. Hultgren. "Spectral effects in short pulse pump-probe measurements". *Applied Physics Letters* 68 (4) (1995), pp. 449–451.

[78] M. Sheik-Bahae, A. A. Said, D. Hagan, M. Soileau, and E. W. Van Stryland. "Nonlinear refraction and optical limiting in thick media". *Optical Engineering* 30 (8) (1991), pp. 1228–1235.

[79] B. E. Saleh and M. C. Teich. *Fundamentals of Photonics*. John Wiley & Sons, Inc., 1991.

[80] H. Kogelnik and T. Li. "Laser Beams and Resonators". *Applied Optics* 54 (10) (1966), pp. 1312–1329.

[81] V. Magni, G. Cerullo, and S. De Silvestri. "ABCD matrix analysis of propagation of gaussian beams through Kerr media". *Optics Communications* 96 (4-6) (1993), pp. 348–355.

[82] M. Sheik-Bahae, A. A. Said, T. H. Wei, D. J. Hagan, and E. W. Van Stryland. "Sensitive Measurement of Optical Nonlinearities Using a Single Beam". *IEEE Journal of Quantum Electronics* 26 (4) (1990), pp. 760–769.

[83] M. Reichert, H. Honghua, M. R. Ferdinandus, M. Seidel, P. Zhao, T. R. Ensley, D. Peceli, J. M. Reed, D. A. Fishman, S. Webster, D. J. Hagan, and E. W. Van Stryland. "Temporal, spectral, and polarization dependence of the nonlinear optical response of carbon disulfide". *Optica* 1 (2014), pp. 436–445.

[84] M. R. Ferdinandus, H. Hu, M. Reichert, Z. Wang, D. J. Hagan, and E. W. Stryland. "Beam deflection measurement of time and polarization resolved nonlinear refraction". *Optics Letters* 38 (18) (2013), pp. 3518–3521.

[85] D. Burghoff. *Chip-scale terahertz frequency combs and multiheterodyne spectroscopy*. OSA Laser Systems Technical Group (https://www.youtube.com/watch?v=wCcYzjQDpyI), 2017.

[86] S. T. Cundiff and J. Ye. "Colloquium: Femtosecond optical frequency combs". *Reviews of Modern Physics* 75 (2003), pp. 325–342.

[87] U. Keller. "Recent developments in compact ultrafast lasers". *Nature* 424 (6950) (2003), pp. 831–838.

[88] P. D. Haye, A Schliesser, O Arcizet, T Wilken, R Holzwarth, and T. J. Kippenberg. "Optical frequency comb generation from a monolithic microresonator". *Nature* 450 (20) (2007), pp. 1214–1217.

[89] T Herr, V Brasch, J. D. Jost, C. Y. Wang, N. M. Kondratiev, M. L. Gorodetsky, and T. J. Kippenberg. "Temporal solitons in optical microresonators". *Nature Photonics* 8 (2) (2013), pp. 145–152.

[90] G. P. Agrawal, T. B. Laboratories, and M. Hill. "Population pulsations and nondegenerate four-wave mixing in semiconductor lasers and amplifiers". *Journal of the Optical Society of America B* 5 (1) (1988), pp. 147–159.

[91] J. B. Khurgin, Y. Dikmelik, A. Hugi, and J. Faist. "Coherent frequency combs produced by self frequency modulation in quantum cascade lasers". *Applied Physics Letters* 104 (2014), p. 081118.

[92] B. Meng, M. Singleton, M. Shahmohammadi, F. Kapsalidis, R. Wang, M. Beck, and J. Faist. "Mid-Infrared Frequency Comb from a Ring Quantum Cascade Laser". *Optica* 7 (2) (2020), pp. 162–167.

[93] M. Piccardo, B. Schwarz, D. Kazakov, M. Beiser, N. Opačak, Y. Wang, S. Jha, J. Hillbrand, M. Tamagnone, W. T. Chen, A. Y. Zhu, L. L. Columbo, A. Belyanin, and F. Capasso. "Frequency combs induced by phase turbulence". *Nature* 582 (7812) (2020), pp. 360–364.

[94] L Columbo, M Piccardo, F Prati, L. A. Lugiato, M Brambilla, A Gatti, C Silvestri, M Gioannini, N Opa, B Schwarz, F Capasso, and P. Torino. "Unifying Frequency Combs in Active and Passive Cavities : Temporal Solitons in Externally Driven Ring Lasers". *Physical Review Letters* 126 (173903) (2021).

[95] M. Bo, M. Singleton, J. Hillbrand, M. Franckié, M. Beck, and J. Faist. "Dissipative Kerr solitons in semiconductor ring lasers". *arxiv:2106.05078v1* (2021).

[96] Z. Han, D. Ren, and D. Burghoff. "Sensitivity of SWIFT spectroscopy". *Optics Express* 28 (5) (2020), pp. 6002–6017.

Relevant publications

Microcavity-enhanced Kerr nonlinearity in a vertical-external-cavity surface-emitting laser

C. Kriso, S. Kress, T. Munshi, M. Grossmann, R. Bek, M. Jetter, P. Michler, W. Stolz, M. Koch, and A. Rahimi-Iman, Optics Express 27, 11914-11929 (2019)

Abstract Self-mode-locking has become an emerging path to the generation of ultrashort pulses with vertical-external-cavity surface-emitting lasers. In our work, a strong Kerr nonlinearity that is so far assumed to give rise to mode-locked operation is evidenced and a strong nonlinearity enhancement by the microcavity is revealed. We present wavelength-dependent measurements of the nonlinear absorption and nonlinear refractive index change in a gain chip using the Z-scan technique. We report negative nonlinear refraction up to $5x10^{12}$ cm^2/W in magnitude in the (InGa)As/Ga(AsP) material system close to the laser design wavelength, which can lead to Kerr lensing. We show that by changing the angle of incidence of the probe beam with respect to the gain chip, the Kerr nonlinearity can be wavelength-tuned, shifting with the microcavity resonance. Such findings may ultimately lead to novel concepts with regard to tailored self-mode-locking behavior achievable by peculiar Kerr-lens chip designs for cost-effective, robust and compact fs-pulsed semiconductor lasers

DOI: 10.1364/OE.27.011914
URL: `https://doi.org/10.1364/OE.27.011914`

Author's contributions:

A. Rahimi-Iman initiated the investigation of nonlinear lensing in VECSELs. S. Kress built the first version of the Z-scan setup. I extended and improved the setup with the help of T. Munshi. W. Stolz provided a sample that was used to extensively test and improve the setup. M. Grossmann, R. Bek, M. Jetter and P. Michler provided the sample that was used for the measurements presented in this paper. I performed the measurements and analyzed the data. The manuscript was mainly written by me, with contributions from A. Rahimi-Iman, and was revised by the other coauthors. M. Koch and A. Rahimi-Iman supervised the work.

Research Article | Vol. 27, No. 9 | 29 Apr 2019 | OPTICS EXPRESS 11914
Optics EXPRESS

Microcavity-enhanced Kerr nonlinearity in a vertical-external-cavity surface-emitting laser

CHRISTIAN KRISO,[1] SASCHA KRESS,[1] TASNIM MUNSHI,[1] MARIUS GROSSMANN,[2] ROMAN BEK,[2] MICHAEL JETTER,[2] PETER MICHLER,[2] WOLFGANG STOLZ,[1] MARTIN KOCH,[1] AND ARASH RAHIMI-IMAN[1,*]

[1]*Faculty of Physics and Materials Sciences Center, Philipps-Universität Marburg, D-35032 Marburg, Germany*
[2]*Institut für Halbleiteroptik und Funktionelle Grenzflächen, Center for Integrated Quantum Science and Technology (IQST) and SCoPE, University of Stuttgart, Allmandring 3, D-70569 Stuttgart, Germany*
**a.r-i@physik.uni-marburg.de*

Abstract: Self-mode-locking has become an emerging path to the generation of ultrashort pulses with vertical-external-cavity surface-emitting lasers. In our work, a strong Kerr nonlinearity that is so far assumed to give rise to mode-locked operation is evidenced and a strong nonlinearity enhancement by the microcavity is revealed. We present wavelength-dependent measurements of the nonlinear absorption and nonlinear refractive index change in a gain chip using the Z-scan technique. We report negative nonlinear refraction up to $5x10^{-12}$ cm^2/W in magnitude in the (InGa)As/Ga(AsP) material system close to the laser design wavelength, which can lead to Kerr lensing. We show that by changing the angle of incidence of the probe beam with respect to the gain chip, the Kerr nonlinearity can be wavelength-tuned, shifting with the microcavity resonance. Such findings may ultimately lead to novel concepts with regard to tailored self-mode-locking behavior achievable by peculiar Kerr-lens chip designs for cost-effective, robust and compact fs-pulsed semiconductor lasers.

1. Introduction

The Kerr effect is at the basis of many important device concepts like all-optical switching [1], optical limiting [2] and soliton mode-locking of lasers and microresonators [3,4]. The capability to accurately measure and model the nonlinear refractive index changes associated with the Kerr effect is crucial for improved device operation, where a specifically tailored nonlinear refractive index is required, e.g. for the intensity-dependent Kerr lensing. Several measurement schemes have been developed in the past for the characterization of the nonlinear refractive index [5–7], with the Z-scan technique [8] being undoubtedly the most prominent one due to its simplicity and high sensitivity. This method continues to be of high experimental value with the rise of novel material classes like graphene and other two-dimensional semiconductors, which often exhibit a very strong refractive nonlinearity [9–11].

Kerr-lens mode-locked Ti:Sapphire lasers have dominated the field of ultra-short high-power mode-locked lasers since their initial discovery nearly three decades ago [12,13]. In these lasers, the intensity-dependent refractive index of the gain crystal leads to self-focusing of the laser beam for high intensities. When part of the continuous-wave (cw) beam profile is suppressed by inserting a slit into the cavity or reducing the pump spot on the crystal, an artificial ultrafast saturable absorber can be formed and can lead to very short pulse emission down to a few fs in duration [14,15].

In recent years, a similar behavior has been observed in saturable-absorber-free mode-locked vertical-external-cavity surface-emitting lasers (VECSELs) [16–20] with very good mode-locking properties being reported for quantum-well-based (QW) [21] as well as for quantum-dot-based VECSELs [22]. These “self-mode-locked” VECSELs could lead to cheap and compact, high-power pulsed sources with sub-GHz to multi-GHz repetition rates for

#355045 https://doi.org/10.1364/OE.27.011914
Journal © 2019 Received 10 Dec 2018; revised 16 Mar 2019; accepted 17 Mar 2019; published 15 Apr 2019

Optics EXPRESS

frequency metrology, spectroscopy and nonlinear imaging, rendering expenses for and limitations of saturable-absorber mirrors obsolete. Thus, one can expect self-mode-locking to open up new application scenarios for these techniques. However, there has been a controversy in this field whether self-mode-locking in VECSELs has been properly demonstrated, particularly addressed by [23], and whether it represents a technique capable of delivering stable mode-locking, as evidenced in the history of this field [24]. The lack of understanding concerning its possible driving mechanisms remains the key motivation behind ongoing attempts to identify and quantify intrinsic VECSEL-chip related nonlinearities that could promote self-mode-locking, in particular the nonlinear refractive index properties, which are essential for Kerr-lens mode-locking.

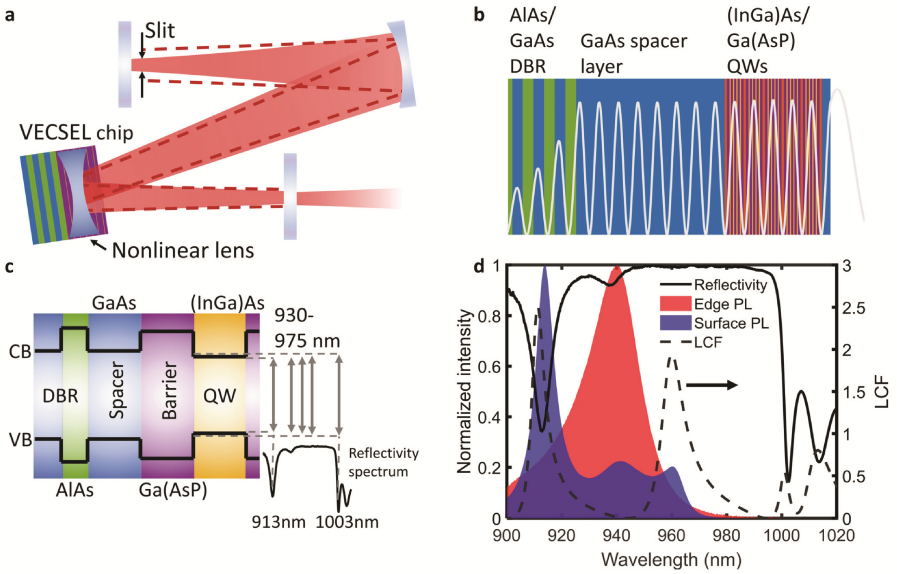

Fig. 1. VECSEL chip characteristics: (a) Illustration of a Kerr-lens mode-locked VECSEL with the dashed lines indicating the cw beam profile while the shaded area traces the beam profile when altered by the nonlinear defocusing lens in the VECSEL chip. Such an intensity-dependent lens can lead to beam narrowing at the end mirror of the cavity and possibly favor mode-locking when a slit inserted there adds losses to the cw beam by truncating it laterally. (b) Chip structure with standing-wave electric field at the design wavelength of 960 nm. (c) Band-gap configuration of the different materials used in the gain chip compared to the stopband of the chip and the investigated wavelength range (930 – 975 nm). (d) Measured reflectivity spectrum, surface and edge photoluminescence (PL), and calculated longitudinal confinement factor (LCF) of the investigated VECSEL chip.

Here, we present wavelength-dependent measurements of the nonlinear refractive index around the resonance of a multi-quantum-well VECSEL gain structure designed for lasing at around 960 nm. We perform Z-scan measurements in the range of 930 nm to 975 nm in order to reveal the interplay of nonlinear refraction and absorption in this spectral range. Changing the angle of incidence allows us to discuss the role of the longitudinal confinement factor, i.e. the cavity resonance, in the observed enhancement of the nonlinearity. We report a negative nonlinear refraction up to $5\text{x}10^{-12}$ cm^2/W in magnitude close to the laser design wavelength. This leads to a defocusing lens which is sufficient to perturb the cavity beam and possibly give rise to Kerr-lens mode-locking. Figure 1(a) displays a possible cavity configuration to exploit this measured Kerr-lens for mode-locking where the defocusing lens in the gain chip leads to beam narrowing at the end mirror, thus, favoring mode-locking when a slit is inserted there. A similar cavity has been used in [21] to obtain self-mode-locking and has been

Optics EXPRESS

investigated numerically in [25] to support in principle Kerr-lens mode-locking for a defocusing nonlinear lens in the gain chip.

2. Investigations on the self-mode-locking effects in VECSELs

The claim of the observed "self-mode-locking" behavior being governed by Kerr-lens mode-locking [17] has been supported by investigations of the nonlinear refractive index in VECSEL gain structures [26–28], reporting refractive index changes sufficiently strong to be able to perturb the cavity beam profile strongly. Although not being a definite proof that self-mode-locking is indeed caused by Kerr-lensing these results are suggestive and call for a more detailed understanding of the nonlinear lensing properties in VECSELs. In particular, prior measurements were exclusively performed at arbitrarily selected (experimentally available) single wavelengths. Such experiments were not taking into account the microcavity resonance as well as the strong dispersion of the nonlinear refractive index around the band edge, which is characteristic for contributions to the nonlinear refractive index, both, from the bound-electronic Kerr effect (BEKE) existing below the bandgap [29] and from free-carrier-related nonlinearities (FCN) existing above the band edge [30].

While the nonlinear optical properties of semiconductors below the band gap have been extensively studied and modeled using the Z-scan method [29,31,32], nonlinear optical processes above and around the band gap have mostly been investigated by pump-probe techniques [30,33] or linear absorption measurements [34]. These methods cannot access the nonlinear refractive index directly but use nonlinear Kramers-Kronig relations to calculate it from nonlinear absorption spectra. Very few reports on direct measurements of the nonlinear refractive index properties of QW structures exist so far, which solely can account fully for nonlinear pulse propagation of a single pulse through the medium [35,36].

Although giving a rough estimate of the strength of the resonant nonlinearity in multiple-quantum-well structures, these measurement results [33–36] cannot arbitrarily be transferred to other sample designs as the nonlinear refractive index constitutes an effective one, composed of different material nonlinearities and their respective interaction containing both BEKE and FCN. Thus, the direct determination of the nonlinear refractive index by Z-scan measurements becomes inevitable whenever its precise value for a particular semiconductor heterostructure is of interest. We define the effective nonlinear refractive index n_2 as

$$n(I_0) = n_0 + n_2 I_0, \tag{1a}$$

with $n(I_0)$ being the total refractive index, n_0 the intensity independent refractive index and I_0 the optical peak power density. It is important to note that this definition of n_2 comprises both non-instantaneous contributions induced by FCN and instantaneous contributions from BEKE. To distinguish the relative contributions from FCN and BEKE, time-resolved measurements would be required.

Complementary to the definition of the intensity dependent refractive index n_2 the nonlinear absorption coefficient β can be defined as

$$\alpha(I_0) = \alpha_0 + \beta I_0, \tag{1b}$$

with α_0 being the linear absorption coefficient and $\alpha(I_0)$ the total absorption coefficient. It is important to point out that β compared to n_2 only comprises ultrafast $\chi^{(3)}$ effects, as carrier-related absorption would lead to saturation and thus to a more complex relation on incident intensity as detailed in Appendix C.

The goal of this work is the determination of the effective n_2 of a VECSEL chip as well as of the nonlinear absorption coefficient β acting as possible loss mechanism.

Optics EXPRESS

3. VECSEL chip design and Z-scan measurements

The investigated VECSEL chip sketched in Fig. 1(b) consists of 20 (InGa)As/Ga(AsP) quantum wells embedded within GaAs spacer layers to provide partial overlap of the antinodes of the standing wave electric field in the microcavity with the quantum wells. Subsequent 30 GaAs/AlAs distributed Bragg reflector (DBR) pairs provide the high reflectivity needed for efficient laser operation together with external mirrors. After the DBR a thick GaAs spacer layer is grown with the intention of achieving a double-resonance for both the laser wavelength at normal incidence and an 888-nm pump under an incident angle of 30°. Since at this wavelength only the QWs are pumped, the absorption length is drastically reduced compared to a barrier pumping scheme. To compensate for this, the DBR stopband is designed to cover also the pump wavelength, and the field enhancement due to the resonance leads to an increased pump absorption. The chip is designed for lasing operation at around 960 nm. Figure 1(c) shows the band gap alignment of the various materials composing the gain chip. It can be seen that the probe wavelengths, which range from 930 nm to 975 nm, are scanning across the quantum-well band gap, thus, our measurements are particularly sensitive to the nonlinear refractive index changes which are characteristic for near-resonance probing. The wavelength-dependent longitudinal confinement factor (LCF) characterizes the strength of a microcavity's standing-wave electric field at the location of the quantum wells (see Appendix B) and is depicted together with the reflectivity spectrum, the surface as well as the edge photoluminescence (PL) in Fig. 1(d).

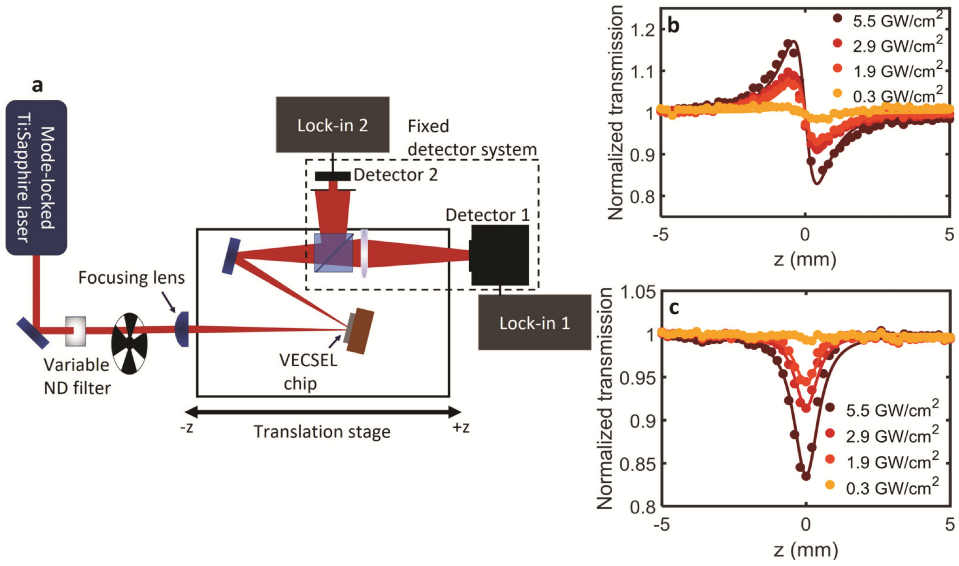

Fig. 2. Experimental Z-scan setup and data: Different neutral-density (ND) filters are used to systematically vary the incident probe power on the VECSEL chip. The sample is translated through the focus of the 150-fs pulsed probe beam, which is chopped and analyzed by two detectors using a lock-in scheme. (b) Exemplary Z-scan measurements at 955 nm for different peak probe intensities irradiated at an angle of 20° are shown, with the corresponding open scan recorded by detector 1 (c). The solid lines are the respective fits to the measurement data according to the models from [8].

For Z-scan measurements, the chip structure was mounted on a piece of copper without any active cooling. A wavelength tunable, mode-locked Ti:Sapphire laser emitting pulses of approximately 150 fs pulse length and a spectral width of about 8 nm was used to probe the chip structure at different center wavelengths around the design wavelength of the gain chip.

Optics EXPRESS

For each center wavelength, the pulse length was determined with a frequency-resolved optical gating (FROG) device and the laser spectrum was monitored with an optical spectrometer.

A lens with 50 mm focal length was used to focus the probe beam down to a spot size radius of 12 µm which was confirmed by a beam profile measurement around the focus of the probe beam. After reflection from the sample and a folding mirror, which were both mounted on a translation stage, a beam splitter and two detectors were used to record the position-dependent transmittance of the probe laser when the sample was moved through the focus of the lens. One detector was covered by a partially closed aperture, which was aligned for maximal transmission. The second detector collected the whole probe beam using a focusing lens. The trace recorded with the first detector will be referred to as closed scan, which is sensitive to, both, nonlinear lensing and nonlinear absorption. The trace recorded with the first detector will be referred to as open scan, which is only sensitive to nonlinear absorption. Following [8], we obtain the final Z-scan curve by dividing the closed scan by the open scan, performing a background subtraction with a low-intensity scan and normalizing to a transmittance of 1 for transmission at positions far away from the focus. Figure 2(b) shows exemplary Z-scan measurements at a center wavelength of 955 nm for different peak probe intensities at 20° angle of incidence together with the respective fits. They show good agreement between model and experiment including an approximately symmetric decrease of peak and valley transmission for decreasing peak probe-power density. The origin of the slight asymmetry of the Z-scan measurements with respect to peak and valley magnitude is not completely understood but might stem from a not-ideal Gaussian probe beam profile or aberrations induced by the focusing lens. The decrease in transmission close to the focus in the open scan (Fig. 2(c)) is attributed to two-photon absorption.

The angle of incidence of the probe beam on the VECSEL chip was varied in the course of the experiment from 10 to 20 and 30°, in order to reveal the influence of the microcavity on the measured nonlinearity. At each angle of incidence, Z-scan measurements were performed for different probe center wavelengths around the chip's design wavelength and varying probe intensities.

4. Experimental results and discussion

In order to determine very accurately the value of nonlinear absorption and refraction in the VECSEL chip, we performed Z-scan measurements for different probe-peak intensities at center wavelengths from 930 to 975 nm. If a refractive (or an absorbing) third-order nonlinearity is present, the nonlinear on-axis phase shift $\Delta\Phi_0$ (or the normalized nonlinear on-axis absorption q_0) will vary linearly with peak probe power density. In such case, the strength of the nonlinearity is proportional to the slope of the nonlinear phase shift (or the normalized nonlinear absorption) with respect to the peak probe power density.

Optics EXPRESS

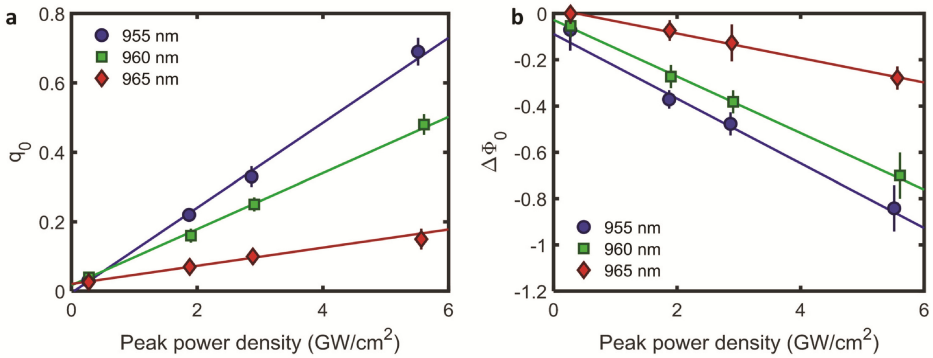

Fig. 3. Coefficients for the extraction of nonlinear absorption and refraction: (a) Normalized nonlinear absorption q_0 and (b) nonlinear on-axis phase shift $\Delta\Phi_0$ as a function of the incident peak probe intensity for different probe center wavelengths irradiated at 20°. The errors for the respective extracted magnitudes represent the fit tolerance and were determined by varying the fit parameter (q_0 or $\Delta\Phi_0$) until the fit model did not match the measurements anymore (similar to [37]).

Figure 3 shows, both, the normalized nonlinear on-axis absorption q_0 (Fig. 3(a)) and the nonlinear on-axis phase shift $\Delta\Phi_0$ (Fig. 3(b)) as a function of the incident peak power density extracted from the open and closed Z-scan curves. The very good agreement with the linear fit shows that measured nonlinear absorption and nonlinear phase shift are indeed mainly caused by a third-order nonlinearity. It is important to note that nonlinear-refractive-index changes caused by two-photon-absorption-generated free carriers would appear as an effective fifth-order nonlinearity [8] causing a deviation from the linear fit. Due to the good agreement to the linear fit, this mechanism can be neglected for our measurements.

Using the relations $\beta = dq_0/dI_0\ 1/L_{eff}$ and $n_2 = d\Delta\Phi_0/dI_0\ 1/(kL_{eff})$, values for the nonlinear absorption β and refraction n_2 can be extracted. These are plotted in Fig. 4 for the incidence angles of 10, 20 and 30°.

Optics EXPRESS

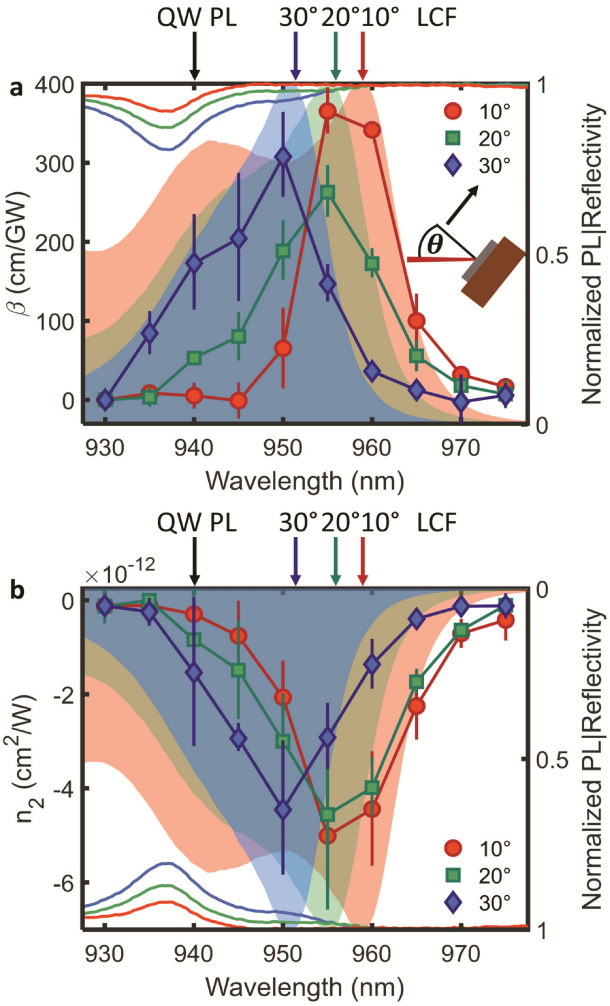

Fig. 4. Wavelength and angle-dependent nonlinear absorption and nonlinear refraction: (a) Nonlinear absorption β and (b) nonlinear refraction n_2 as a function of the wavelength (left axes), measured for the incidence angles of 10, 20 and 30°. The lines between the measurement points may serve as guides to the eyes. Arrows atop the diagram indicate the wavelength of the QW PL (cf. Fig. 1(d)) as well as the different angle-dependent LCF peaks. The corresponding surface PL at given angle of incidence, which is subdue to the microcavity resonance, is plotted in both graphs for comparison (shaded plots) as well as the corresponding reflectivity spectra (line plots), both normalized to 1 and with respect to the right axes. An inset represents the probe geometry with respect to the VECSEL chip. The errors were determined by performing a linear least square fit to the normalized nonlinear absorption q_0 and nonlinear phase shift $\Delta\Phi_0$ as a function of probe intensity (as displayed in Fig. 3) and taking the 95% confidence interval of the fit as error.

For both nonlinear absorption and nonlinear refraction, a strong enhancement of the nonlinearity can be observed at wavelengths between 950 to 960 nm. Strikingly, this corresponds very well to the field enhancement at the QWs due to the microcavity resonance, which is represented by the surface photoluminescence peak at that on-chip angle and is also plotted into Figs. 8(a) and 8(b) for comparison. To verify that the microcavity resonance, i.e. the Fabry-Pérot cavity's filter function, is responsible for this effect, we have performed the measurements for different angles of incidence and find that the peak of the nonlinearity

Optics EXPRESS

spectrum follows the corresponding surface PL spectrum peak for different angles. This unambiguously demonstrates that the microcavity resonance is strongly contributing to the enhancement of the respective nonlinearity. This enhancement takes place slightly below the linear absorption band edge, which can be estimated from the reflectivity spectra plotted in Fig. 4 for comparison. We consider the contribution of the GaAs spacer layer negligible with respect to the contributions of the (InGa)As/Ga(AsP) gain region, as the theoretical nonlinear refractive index of GaAs [29] is in the order of $-6\text{x}10^{-13}$ cm^2/W in the investigated wavelength range and thus significantly smaller than the effective n_2 values measured here. The absolute magnitude of the effective nonlinear refractive index rises up to $5\text{x}10^{-12}$ cm^2/W, which is an order of magnitude larger than reported in [28]. This can be attributed to the fact that the authors did not use a probe wavelength close to the maximum of the microcavity resonance. Moreover, the chip exhibited nearly half the number of QWs compared to our chip design.

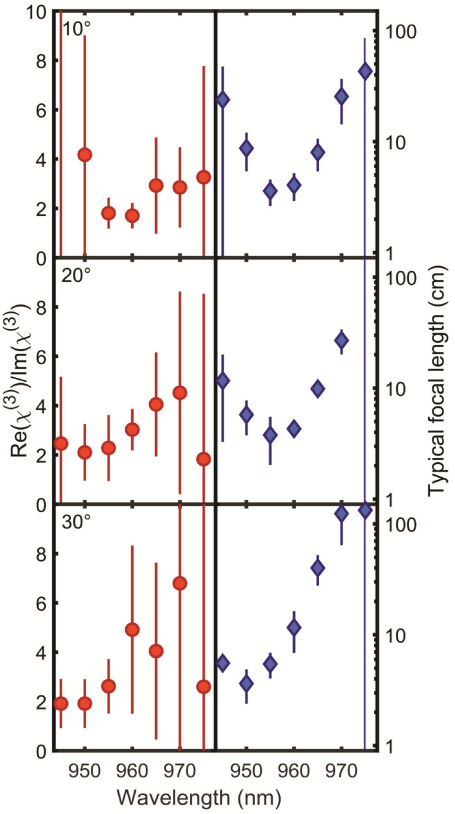

Fig. 5. Ratio of real and imaginary part of the measured third order nonlinearity $\chi^{(3)}$ and typical focal length of a Kerr-lens: The ratio of nonlinear refraction with respect to nonlinear absorption is plotted as a function of the wavelength in the left column of the diagram for the three different angles of incidence. Additionally, the focal length, which would occur in a typically self-mode-locked VECSEL configuration, is plotted here in the right column. The error bars stem from the errors in nonlinear absorption and refraction as depicted in Fig. 4.

The strong tunability of the nonlinearity with the microcavity resonance indicates that the (InGa)As/Ga(AsP) material system, which showed best self-mode-locking behavior so far [21] can be possibly operated in the self-mode-locking regime over a large wavelength range exceeding 10 nm thus supporting both broad-band operation and tunability. This is consistent with the results of [35] for a multiple-quantum-well structure which showed a comparable

Optics EXPRESS

bandwidth of strong nonlinear refraction (up to $8.5\text{x}10^{-10}$ cm^2/W in magnitude) where no microcavity effect was present.

In order to evaluate our measurement results with respect to possible self-mode-locking in VECSELs due to the Kerr effect, we plot the ratio of real and imaginary part of the third-order nonlinearity $\chi^{(3)}$,

$$\frac{\text{Re}(\chi^{(3)})}{\text{Im}(\chi^{(3)})} = \left|\frac{2\Delta\Phi_0}{q_0}\right| = \left|\frac{2kn_2}{\beta}\right|, \tag{2}$$

in Fig. 5 (left axis). This describes how strong nonlinear refraction dominates over nonlinear absorption [8]. We only include wavelengths above 945 nm to cover mostly the laser-relevant wavelength range.

Here, a nearly constant ratio of real and imaginary part of $\chi^{(3)}$ shows that both n_2 and β are equally affected by the cavity-resonance enhancement. In contrast to this, in pure quantum-well structures without any cavity, this ratio varies considerably as a function of the wavelength around the bandgap [35]. However, optical loss by two-photon absorption is quite significant in our measurements when rising up to more than 15% at the highest probe intensity in Fig. 2(c). Nevertheless, this effect might be reduced in a pumped system, in which population inversion is maintained by the typical above-band high-power continuous-wave pumping scheme. Also, longer pulses – typical pulse lengths of self-mode-locked VECSELs are around 1 ps [21,22]– might reduce the occurrence of two-photon absorption [38].

The typical focal length of a Kerr-lens, which would occur in a self-mode-locked VECSEL cavity as reported in [21], with the here measured value of nonlinear refraction is plotted in the same diagram (right axis of Fig. 5). For sub-ps pulses with 1-kW peak power, the focal length of the induced Kerr nonlinearity should be in the order of magnitude of the laser cavity length, which ranges usually between 10 to 30 cm. Our calculated values are between a few cm up to 30 cm and more. This information supports the attribution of the observed self-mode-locking being Kerr-lens mode-locking and is key to designing a cavity where the angle of incidence of the laser mode on the gain chip is, apart from geometric constraints, a free design parameter in a V- or Z-cavity.

5. On the origin of nonlinear lensing and the implications for mode-locking

The respective contributions of FCN and BEKE to the total, measured nonlinearity would define the pulse-shaping mechanism in a Kerr-lens mode-locking scenario due to the different response times. FCN has a slower response time, which is mostly due to the ps relaxation time of excited carriers, compared to BEKE, which can be regarded as instantaneous with respect to fs pulses. Both FCN and BEKE exhibit characteristic dispersions when regarded separately as depicted in Figs. 6(a) and 6(c), with both effects showing strongest changes close to the band gap.

In the theory described by [29], nonlinear refraction is inherently related to nonlinear absorption by the nonlinear Kramers-Kronig relations. Although in most resonant excitation-and-probe scenarios, carrier-related nonlinearities are believed to dominate the third-order nonlinear response [39], bound-electronic contributions even continue to play a role closely above the band gap when no significant excitation or deexcitation of carriers occur [40]. Strong deexcitation of free carriers could be described with an additional use of the Bloch equations. This has been done in [41] and showed that a probe pulse will indeed experience a significant phase shift both from FCN and BEKE with the same order of magnitude when the semiconductor material is excited with a high-intensity pump pulse. These findings have also been supported by comparison to experiments [42].

This indicates that also in mode-locked VECSELs a non-negligible amount of BEKE might be present. The occurrence of two-photon absorption in our measurements, also above the linear absorption edge, further supports this argument as it indicates that probe-power

Optics EXPRESS

densities are sufficiently high to significantly perturb pulse propagation by ultrafast $\chi^{(3)}$ effects, both from its imaginary part resulting in two-photon absorption as well as its real part resulting in nonlinear refraction, which as mentioned already above, are linked by nonlinear Kramers-Kronig relations. It is worth noting that also the authors of [17] attribute their self-mode-locking results with a VECSEL to the ultrafast Kerr effect of bound electrons, without having performed any experimental characterization of the nonlinearity.

However, our measurements did not investigate the effect of cw-pumping, which takes place in actual laser operation. The resulting generation of free carriers, which are probed by the laser pulse and lead to strong stimulated deexcitation of carriers might change the magnitude of the nonlinearity as well as the relative contributions from FCN and BEKE. Preliminary investigations concerning optical pumping and probe-induced nonlinear-refractive-index changes suggest little influence in the absolute value of the nonlinear refraction [28]. The effect of the microcavity resonance on the nonlinearity enhancement revealed by this work will persist in a pumped system.

To ultimately distinguish the possible two contributions from each other, that are the ultrafast bound-electronic Kerr effect (i.e. BEKE) and the non-instantaneous free-carrier nonlinearities (i.e. FCN), time-resolved Z-scan measurements would be required [43]. In addition, the variation of the probe-pulse duration while maintaining equivalent peak powers could provide insight into the nature of the carrier dynamics including the effect of non-equilibrium many-body effects, which become important at sub-ps time-scales [44]. This will be the subject of our future work.

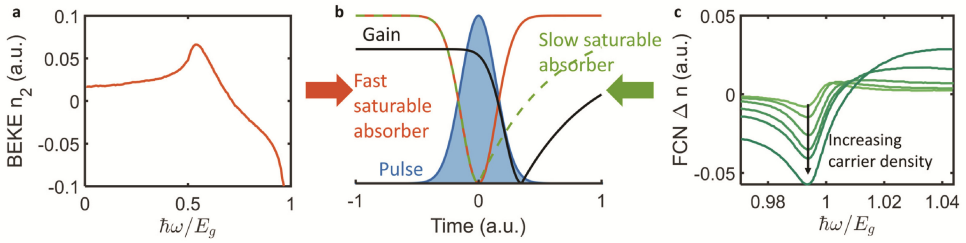

Fig. 6. Illustration of possible saturable absorber mechanisms shaping the pulse: A dominating bound-electronic contribution (BEKE) in the nonlinear response, with its dispersion given in (a) as adapted from [29], would lead to a fast saturable absorber mechanism (red solid line in the schematic time trace of action shown in (b)) similar to traditional Kerr-lens mode-locking. In contrast, a dominating free-carrier-related nonlinear response (FCN), with its dispersion around the band gap given in (c) for different carrier densities as adapted from [30], would lead to slow saturable absorber action (green dashed line in (b)) where pulse formation relies on its combination with fast gain saturation (black solid line in (b)).

If BEKE is the dominating contribution to the nonlinear lensing, self-mode-locking of VECSELs, if caused by nonlinear lensing, would have to be modeled by substituting the slow, highly nonlinear saturable absorber term with a fast saturable absorber term in the common mode-locking model [45] (c.f. Fig. 6(b) on pulse shaping). Additionally, self-phase modulation would have to be incorporated into the model, for which the value of the effective n_2 would be obtained from Z-scan measurements. As a consequence of this, the required group-delay dispersion (GDD) for shortest pulses and stable Kerr-lens mode-locking might differ from the slightly positive GDD values required for optimal SESAM-VECSEL mode-locking [45], which could become a key advantage of self-mode-locked devices towards ultra-short pulse generation after more detailed investigations triggered by the findings reported here.

In contrast, FCN might act as a slow saturable absorber with timescales similar to SESAMs and correspondingly similar mode-locking characteristics. It is important to point out that this would not be due to real saturable absorption occurring in the gain chip. Instead, the refractive-index change induced by changes in the excited-carrier densities would lead to

Optics EXPRESS

nonlinear lensing and only lead to some kind of artificial saturable-absorber action (c.f. Fig. 6(b)) when employed in an appropriate cavity, where nonlinear lensing reduces cavity losses, as indicated in Fig. 1(a).

If both effects were present simultaneously with comparable strength, a combined action of slow and fast saturable absorber would have to be incorporated into a mode-locking model. Also, a situation as in soliton mode-locking might occur in this case [3].

A precise knowledge of the different timescales involved in the effective third-order refractive nonlinearity n_2 would ultimately enable one to explain and model the mechanisms behind Kerr-lens induced self-mode-locking, with important implications for future chip designs.

Finally, we note that the above discussion assumed that self-mode-locking is caused by a Kerr-lens in the VECSEL chip supported by the strong nonlinear refractive index measured here. However, the pure existence of a strong nonlinear lens in the gain chip is not a definite proof yet that self-mode-locking is caused by Kerr-lens mode-locking, which would require observation of self-(de)focusing during self-mode-locked operation.

6. Conclusion

We have presented unique, systematic and direct, wavelength-resolved measurements of the effective nonlinear refractive index and nonlinear absorption in a vertical-external-cavity surface-emitting-laser chip using the Z-scan technique. In support of recent self-mode-locking achievements, strong enhancement of the Kerr nonlinearity is observed in the spectral region of the quantum-well band gap in clear correlation to a microcavity effect, which can shape Kerr lensing in the active region significantly. Negative nonlinear refraction up to $5\text{x}10^{-12}$ cm^2/W close to the laser design wavelength is obtained. Our results show that the resonance feature dominates any material-related dispersion of n_2 which might render it exploitable as design element in future Kerr-lens mode-locked VECSEL devices. This would affect the operation wavelength and spectrum of such VECSELs in addition to other known factors, which govern these properties, such as the material-PL/LCF overlap. While two-photon absorption poses a loss channel for lasing operation, the refractive index changes are sufficiently strong to perturb the cavity beam profile in favor of self-mode-locking. Moreover, by comparing our results to existing theories about the nonlinear-refractive-index changes in semiconductors, we believe that the ultrafast electronic Kerr effect contributes significantly to the nonlinearity while the share of free-carrier nonlinearities compared to the amount of the ultrafast Kerr effect yet remains to be investigated for a pumped system. We expect our results to lead to a better understanding of self-mode-locking in VECSELs and to pave the way to reliable, ultra-short, higher-power pulsed semiconductor-laser sources based on this method.

Appendix A

The semiconductor structure used was fabricated by metal-organic vapor-phase epitaxy (MOVPE) in an AIXTRON FT 3x2" closed coupled shower-head reactor using the standard sources trimethyl-gallium, trimethyl-indium, trimethyl-aluminum, arsine and phosphine. Deposition occurred at pressures of 100 mbar on 6° misoriented GaAs substrates. Following a 30 pair AlAs/GaAs DBR the GaAs spacer layer as well as the active region are grown and the whole structure is completed using a GaAs capping layer.

The active region comprises 20 (InGa)As quantum wells grouped into five packages which are separated using (AlGa)As spacer layers. The compressive strain induced by the QWs is mostly compensated by the surrounding tensile-strained Ga(AsP) barriers and the QW packages are placed according to a resonant periodic gain design at the antinodes of the standing wave electric field.

Optics EXPRESS

Appendix B

To calculate the electric-field distribution in the structure for a particular wavelength we use the matrix formalism of [46]. The overlap of the electric field with the position of the quantum wells is then described by the longitudinal confinement factor,

$$\Gamma_z = \frac{1}{N_q} \frac{\sum_q \left| A_q^+ \exp(ik_q z_q) + A_q^- \exp(-ik_q z_q) \right|^2}{\left|A_0^+\right|^2 + \left|A_0^-\right|^2}, \tag{3}$$

where A_q^+ and A_q^- are the forward and backward traveling wave amplitudes of the vector potential of the electric field at the q^{th} quantum well (QW), respectively. k_q is the respective wave vector, N_q the total number of QWs and z_q the position of the q^{th} QW. A_0^+ and A_0^- are the vector potential amplitudes before the first material layer. The matrix formalism is solved for TE-polarization in accordance with the polarization of the probe laser in the experiment.

Appendix C

In order to extract the nonlinear absorption coefficient β, we fit the open scan data with the model from [8],

$$T(z) = \sum_{m=0}^{\infty} \frac{[-q_0(z)]^m}{(m+1/2)^{3/2}}, \tag{4}$$

with $q_0(z) = \beta I(z) L_{eff} = (\beta I_0 L_{eff})/(1 + z^2/z_0^2)$ being the normalized nonlinear on-axis absorption and $I(z) = I_0/(1 + z^2/z_0^2)$ the z-dependent peak-probe power density as a function of z and I_0, L_{eff} and z_0 being the on-axis peak probe power density, the effective length of the sample and the Rayleigh length of the focused probe beam, respectively. The effective length $L_{eff} = (1-\exp(-\alpha_0 L))/L$ takes into account the different strength of linear absorption α_0 at different wavelengths. The total length L is here the accumulated thickness of the different material layers including the penetration depth into the DBR and taking into account the double-pass through the chip with the respective angle of incidence. This leads to lengths L from 4.4 to 5.1 µm for angles of incidence from 10 to 30°. Saturable absorption, which becomes important above the linear absorption edge at wavelengths below 950 nm is phenomenologically included to the model applied on the open-scan data by adding the simple model for saturable absorption in transmission,

$$T_{sat}(z) = 1 - \frac{\alpha_0}{1 + \frac{I(z)}{I_s}}, \tag{5}$$

to Eq. (4).

Here, α_0 is again the linear absorption at the respective center wavelength of the probe laser spectrum, and I_s the saturation intensity which is determined by the fit. Equation (5) is normalized to 1 at the edges of the scan, added to Eq. (4) and subtracted by 1 to align the total open-scan fit function to a transmission of 1 for z positions far away from the focus. An exemplary fit of an open scan at 940 nm for 20° angle of incidence is displayed in Fig. 7(a). The resulting normalized nonlinear absorption (the positive one is attributed to two-photon absorption) exhibits a good linear trend as shown in Fig. 7(b), thus validating our method.

Optics EXPRESS

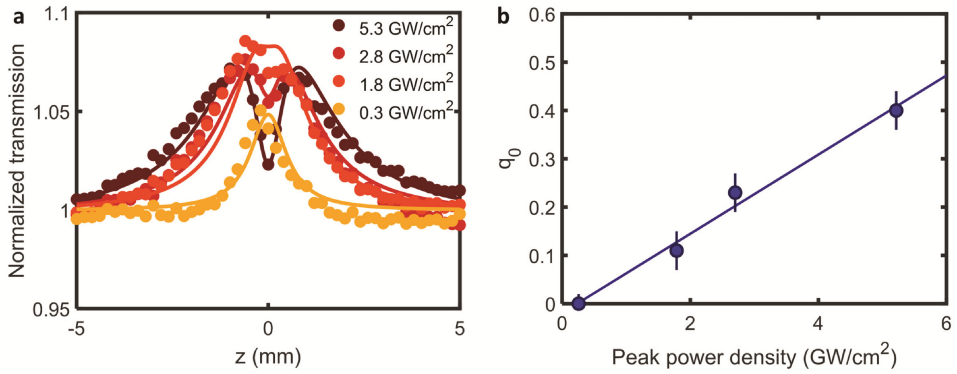

Fig. 7. Example of extraction of normalized nonlinear absorption in the presence of saturable absorption: (a) Open scan at 940 nm and 30° angle of incidence for different probe powers. The fit (solid line) is obtained as described in Appendix C using I_s = 0.2 GW/cm^2 and α_0 = 1.2x10^{-5} m^{-1} for all probe intensities. (b) Resulting nonlinear on-axis absorption as a function of the peak probe density with linear fit (solid line).

We extract the nonlinear phase shift $\Delta\Phi_0$ from the Z-scans by fitting the normalized transmission to the simple model from [8],

$$T(z) = 1 - \frac{4\Delta\Phi_0 \frac{z}{z_0}}{((\frac{z}{z_0})^2 + 9)((\frac{z}{z_0})^2 + 1)}, \quad (6)$$

where $\Delta\Phi_0 = kn_2I_0L_{eff}$ is the nonlinear on-axis phase shift induced by the effective nonlinear refractive index n_2. The sign of the nonlinear phase shift can be easily determined by the position of peak and valley in the Z-scan trace around the focus, which in our measurements always leads to a negative, thus defocusing, nonlinearity.

Appendix D

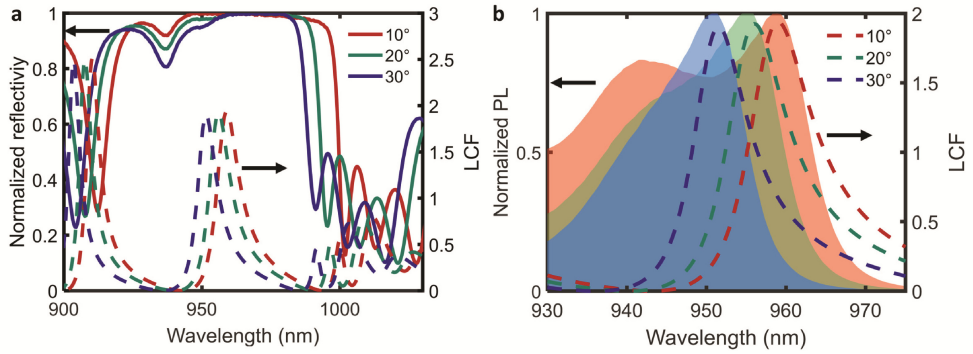

Fig. 8. Angle-dependent chip characterization: (a) Measured reflectivity spectra for different angles of incidence (solid lines, left axis) as well as calculated longitudinal confinement factor (LCF) for the same angles (dashed lines, right axis). (b) Zoom on the longitudinal confinement factor (dashed lines) around the relevant wavelength range in comparison to the measured surface photoluminescence (PL) at the same angles (shaded areas).

The angle-dependent characteristics of the Bragg reflector and the resonant-periodic-gain structure are displayed in Fig. 8. Figure 8(a) shows the full stopband of the DBR for different angles of incidence together with the corresponding calculated longitudinal confinement factors. For an increasing angle of incidence, both the stopband and the cavity resonance experience a significant blue shift.

Optics EXPRESS

The surface PL spectra in the Fig. 8(b) (the same as in Figs. 4(a) and 4(b)) are recorded by placing the collection optics (collimating and focusing lens aligned in a lens tube) at the respective angle of incidence with respect to the gain chip and by fiber coupling the signal to an optical spectrum analyzer. These spectra correspond well with the respective calculated longitudinal confinement factors, thus, validating the use of the surface PL for determining the spectral position of the microcavity resonance.

Appendix E

To estimate the uncertainty in the determination of the fit parameter q_0 or $\Delta\Phi_0$, we vary them in Eqs. (4) and (6) until there is a significant deviation from the measurement data. Upper and lower bounds are taken as equally spaced from the fit. An example of the limiting cases is displayed in Figs. 9(a) and 9(b) for open scan and Z-scan of Fig. 2 (shown in (a) and (b), respectively). The bounds of q_0 and $\Delta\Phi_0$ are then taken into account in a weighted linear least square fit where the weights are the inverse of the respective variances meaning they are proportional to the inverse of the square of the error bounds. The resulting fits are plotted in Fig. 9. The subsequent error of the value of nonlinear refraction n_2 or β as displayed in Fig. 4 is then the 95% confidence interval of this fit.

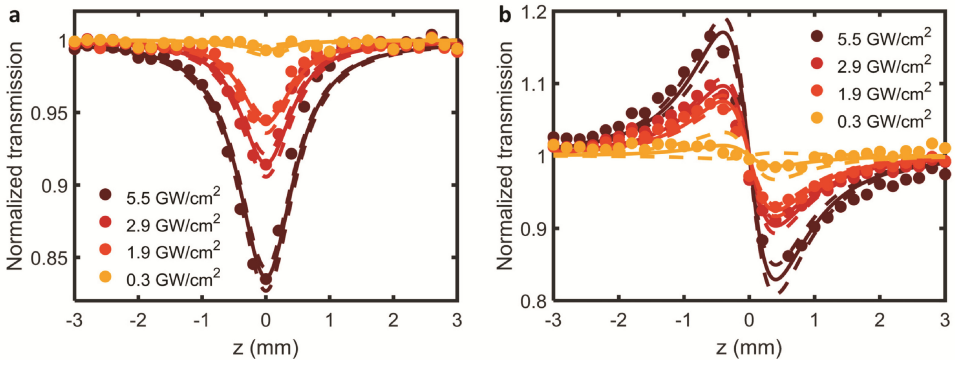

Fig. 9. Measurement data with fit model as well as manually-determined symmetrical upper and lower bounds of the fit: This is a zoom of Fig. 2(b) and 2(c). (a) Open scan and (b) Z-scan with fit (solid line) and upper and lower limit of the respective fits (dashed lines) for the estimation of the data-evaluation uncertainties.

Funding

Deutsche Forschungsgemeinschaft (DFG), Grant No. RA2841/1-1.

Acknowledgments

The authors thank S.W. Koch and M. Gaafar for helpful discussions and O. Mohiuddin as well as M. Alvi for technical assistance.

References

1. E. Yüce, G. Ctistis, J. Claudon, J.-M. Gérard, and W. L. Vos, "Optimal all-optical switching of a microcavity resonance in the telecom range using the electronic Kerr effect," Opt. Express **24**(1), 239–253 (2016).
2. E. W. Van Stryland, Y. Y. Wu, D. J. Hagan, M. J. Soileau, and K. Mansour, "Optical limiting with semiconductors," J. Opt. Soc. Am. B **5**(9), 1980–1988 (1988).
3. F. X. Kärtner, I. D. Jung, and U. Keller, "Soliton mode-locking with saturable absorbers," IEEE J. Sel. Top. Quantum Electron. **2**(3), 540–556 (1996).
4. T. Herr, V. Brasch, J. D. Jost, C. Y. Wang, N. M. Kondratiev, M. L. Gorodetsky, and T. J. Kippenberg, "Temporal solitons in optical microresonators," Nat. Photonics **8**(2), 145–152 (2014).
5. M. J. Moran, C. Y. She, and R. L. Carman, "Interferometric Measurements of the Nonlinear Refractive-Index Coefficient Relative to CS2 in Laser-System-Related Materials," IEEE J. Quantum Electron. **11**(6), 259–263 (1975).
6. D. Weaire, B. S. Wherrett, D. A. B. Miller, and S. D. Smith, "Effect of low-power nonlinear refraction on laser-

Optics EXPRESS

beam propagation in InSb," Opt. Lett. **4**(10), 331–333 (1979).
7. R. Adair, L. L. Chase, and S. A. Payne, "Nonlinear refractive-index measurements of glasses using three-wave frequency mixing," J. Opt. Soc. Am. B **4**(6), 875–881 (1987).
8. M. Sheik-Bahae, A. A. Said, T. H. Wei, D. J. Hagan, and E. W. Van Stryland, "Sensitive Measurement of Optical Nonlinearities Using a Single Beam," IEEE J. Quantum Electron. **26**(4), 760–769 (1990).
9. H. Zhang, S. Virally, Q. Bao, L. K. Ping, S. Massar, N. Godbout, and P. Kockaert, "Z-scan measurement of the nonlinear refractive index of graphene," Opt. Lett. **37**(11), 1856–1858 (2012).
10. N. Vermeulen, D. Castelló-Lurbe, M. Khoder, I. Pasternak, A. Krajewska, T. Ciuk, W. Strupinski, J. Cheng, H. Thienpont, and J. Van Erps, "Graphene's nonlinear-optical physics revealed through exponentially growing self-phase modulation," Nat. Commun. **9**(1), 2675 (2018).
11. X. Zheng, Y. Zhang, R. Chen, X. Cheng, Z. Xu, and T. Jiang, "Z-scan measurement of the nonlinear refractive index of monolayer WS(2)," Opt. Express **23**(12), 15616–15623 (2015).
12. D. E. Spence, P. N. Kean, and W. Sibbett, "60-fsec pulse generation from a self-mode-locked Ti:sapphire laser," Opt. Lett. **16**(1), 42–44 (1991).
13. S. T. Cundiff, W. H. Knox, E. P. Ippen, and H. A. Haus, "Frequency-dependent mode size in broadband Kerr-lens mode locking," Opt. Lett. **21**(9), 662–664 (1996).
14. U. Keller, "Recent developments in compact ultrafast lasers," Nature **424**(6950), 831–838 (2003).
15. U. Morgner, F. X. Kärtner, S. H. Cho, Y. Chen, H. A. Haus, J. G. Fujimoto, E. P. Ippen, V. Scheuer, G. Angelow, and T. Tschudi, "Sub-two-cycle pulses from a Kerr-lens mode-locked Ti:sapphire laser," Opt. Lett. **24**(6), 411–413 (1999).
16. Y. F. Chen, Y. C. Lee, H. C. Liang, K. Y. Lin, K. W. Su, and K. F. Huang, "Femtosecond high-power spontaneous mode-locked operation in vertical-external cavity surface-emitting laser with gigahertz oscillation," Opt. Lett. **36**(23), 4581–4583 (2011).
17. A. R. Albrecht, Y. Wang, M. Ghasemkhani, D. V. Seletskiy, J. G. Cederberg, and M. Sheik-Bahae, "Exploring ultrafast negative Kerr effect for mode-locking vertical external-cavity surface-emitting lasers," Opt. Express **21**(23), 28801–28808 (2013).
18. L. Kornaszewski, G. Maker, G. P. A. Malcolm, M. Butkus, E. Rafailov, and C. J. Hamilton, "SESAM-free mode-locked semiconductor disk laser," Laser Photonics Rev. **6**(6), L20–L23 (2012).
19. M. Gaafar, C. Möller, M. Wichmann, B. Heinen, B. Kunert, A. Rahimi-Iman, W. Stolz, and M. Koch, "Harmonic self-mode-locking of optically pumped semiconductor disc laser," Electron. Lett. **50**(7), 542–543 (2014).
20. R. Bek, M. Großmann, H. Kahle, M. Koch, A. Rahimi-Iman, M. Jetter, and P. Michler, "Self-mode-locked AlGaInP-VECSEL," Appl. Phys. Lett. **111**(18), 182105 (2017).
21. M. Gaafar, P. Richter, H. Keskin, C. Möller, M. Wichmann, W. Stolz, A. Rahimi-Iman, and M. Koch, "Self-mode-locking semiconductor disk laser," Opt. Express **22**(23), 28390–28399 (2014).
22. M. Gaafar, D. A. Nakdali, C. Möller, K. A. Fedorova, M. Wichmann, M. K. Shakfa, F. Zhang, A. Rahimi-Iman, E. U. Rafailov, and M. Koch, "Self-mode-locked quantum-dot vertical-external-cavity surface-emitting laser," Opt. Lett. **39**(15), 4623–4626 (2014).
23. K. G. Wilcox and A. C. Tropper, "Comment on SESAM-free mode-locked semiconductor disk laser," Laser Photonics Rev. **7**(3), 422–423 (2013).
24. M. A. Gaafar, A. Rahimi-Iman, K. A. Fedorova, W. Stolz, E. U. Rafailov, and M. Koch, "Mode-locked Semiconductor Disk Lasers," Adv. Opt. Photonics **8**(3), 370–400 (2016).
25. A. Rahimi-Iman, M. Gaafar, C. Möller, M. Vaupel, F. Zhang, D. Al-nakdali, K. A. Fedorova, W. Stolz, E. U. Rafailov, and M. Koch, "Self-Mode-Locked Vertical-External-Cavity Surface-Emitting Laser," in *Proc. SPIE 9734, Vertical External Cavity Surface Emitting Lasers (VECSELs) VI, 97340M* (2016).
26. A. H. Quarterman, M. A. Tyrk, and K. G. Wilcox, "Z-scan measurements of the nonlinear refractive index of a pumped semiconductor disk laser gain medium," Appl. Phys. Lett. **106**(1), 011105 (2015).
27. E. A. Shaw, A. H. Quarterman, A. P. Turnbull, T. Chen Sverre, C. R. Head, A. C. Tropper, and K. G. Wilcox, "Nonlinear Lensing in an Unpumped Antiresonant Semiconductor Disk Laser Gain Structure," IEEE Photonics Technol. Lett. **28**(13), 1395–1398 (2016).
28. A. H. Quarterman, S. Mirkhanov, C. J. C. Smyth, and K. G. Wilcox, "Measurements of nonlinear lensing in a semiconductor disk laser gain sample under optical pumping and using a resonant femtosecond probe laser," Appl. Phys. Lett. **109**(12), 121113 (2016).
29. M. Sheik-Bahae, D. C. D. Hutchings, D. J. Hagan, and E. W. Van Stryland, "Dispersion of bound electron nonlinear refraction in solids," IEEE J. Quantum Electron. **27**(6), 1296–1309 (1991).
30. Y. H. Lee, A. Chavez-Pirson, S. W. Koch, H. M. Gibbs, S. H. Park, J. Morhange, A. Jeffery, N. Peyghambarian, L. Banyai, A. C. Gossard, and W. Wiegmann, "Room-temperature optical nonlinearities in GaAs," Phys. Rev. Lett. **57**(19), 2446–2449 (1986).
31. A. A. Said, M. Sheik-Bahae, D. J. Hagan, T. H. Wei, J. Wang, J. Young, and E. W. Van Stryland, "Determination of bound-electronic and free-carrier nonlinearities in ZnSe, GaAs, CdTe, and ZnTe," J. Opt. Soc. Am. B **9**(3), 405–414 (1992).
32. M. Sheik-Bahae, D. J. Hagan, and E. W. Van Stryland, "Dispersion and band-gap scaling of the electronic Kerr effect in solids associated with two-photon absorption," Phys. Rev. Lett. **65**(1), 96–99 (1990).
33. S. H. Park, J. F. Morhange, A. D. Jeffery, R. A. Morgan, A. Chavez-Pirson, H. M. Gibbs, S. W. Koch, N. Peyghambarian, M. Derstine, A. C. Gossard, J. H. English, and W. Weigmann, "Measurements of room-

Optics EXPRESS

temperature band-gap-resonant optical nonlinearities of GaAs/AlGaAs multiple quantum wells and bulk GaAs," Appl. Phys. Lett. **52**(15), 1201–1203 (1988).
34. A. M. Fox, A. C. Maciel, M. G. Shorthose, J. F. Ryan, M. D. Scott, J. I. Davies, and J. R. Riffat, "Nonlinear excitonic optical absorption in GaInAs/InP quantum wells," Appl. Phys. Lett. **51**(1), 30–32 (1987).
35. L. Brzozowski, E. H. Sargent, A. S. Thorpe, and M. Extavour, "Direct measurements of large near-band edge nonlinear index change from 1.48 to 1.55 μm in InGaAs/InAlGaAs multiquantum wells," Appl. Phys. Lett. **82**(25), 4429–4431 (2003).
36. R. Liu, Y. Shu, G. Zhang, J. Sun, X. Xing, B. Pi, J. Yao, Z. Wang, and J. Xu, "Study of nonlinear absorption in GaAs/AlGaAs multiple quantum wells using the reflection Z-scan," Opt. Quantum Electron. **39**(14), 1207–1214 (2007).
37. M. Reichert, H. Hu, M. R. Ferdinandus, M. Seidel, P. Zhao, T. R. Ensley, D. Peceli, J. M. Reed, D. A. Fishman, S. Webster, and D. J. Hagan, "Temporal, spectral, and polarization dependence of the nonlinear optical response of carbon disulfide," Optica **1**(6), 436–445 (2014).
38. C. G. E. Alfieri, D. Waldburger, S. M. Link, E. Gini, M. Golling, G. Eisenstein, and U. Keller, "Optical efficiency and gain dynamics of modelocked semiconductor disk lasers," Opt. Express **25**(6), 6402–6420 (2017).
39. D. N. Christodoulides, I. C. Khoo, G. J. Salamo, G. I. Stegeman, and E. W. Van Stryland, "Nonlinear refraction and absorption: mechanisms and magnitudes," Adv. Opt. Photonics **2**(1), 60–200 (2010).
40. M. Sheik-Bahae and E. W. Van Stryland, "Ultrafast nonlinearities in semiconductor laser amplifiers," Phys. Rev. B Condens. Matter **50**(19), 14171–14178 (1994).
41. J. Mørk and A. Mecozzi, "Theory of the ultrafast optical response of active semiconductor waveguides," J. Opt. Soc. Am. B **13**(8), 1803–1816 (1996).
42. J. Mørk, A. Mecozzi, and C. Hultgren, "Spectral effects in short pulse pump-probe measurements," Appl. Phys. Lett. **68**, 449–541 (1995).
43. J. Wang, M. Sheik-Bahae, A. A. Said, D. J. Hagan, and E. W. Van Stryland, "Time-resolved Z-scan measurements of optical nonlinearities," J. Opt. Soc. Am. B **11**(6), 1009–1017 (1994).
44. J. Hader, M. Scheller, A. Laurain, I. Kilen, C. Baker, J. V. Moloney, and S. W. Koch, "Ultrafast non-equilibrium carrier dynamics in semiconductor laser mode-locking," Semicond. Sci. Technol. **32**(1), 013002 (2016).
45. R. Paschotta, R. Häring, A. Garnache, S. Hoogland, A. C. Tropper, and U. Keller, "Soliton-like pulse-shaping mechanism in passively mode-locked surface-emitting semiconductor lasers," Appl. Phys. B **75**(4-5), 445–451 (2002).
46. A. C. Tropper and S. Hoogland, "Extended cavity surface-emitting semiconductor lasers," Prog. Quantum Electron. **30**(1), 1–43 (2006).

Microcavity-enhanced Kerr nonlinearity in a vertical-external-cavity surface-emitting laser: erratum

C. Kriso, S. Kress, T. Munshi, M. Grossmann, R. Bek, M. Jetter, P. Michler, W. Stolz, M. Koch, and A. Rahimi-Iman, accepted in Optics Express (2021)

Abstract We correct a mistake in [Opt. Express 27,11914-11929 (2019)] when calculating the focal length of the Kerr lens with the measured values of the nonlinear refractive index n_2 and parameters of a prototypical self-mode-locking VECSEL cavity. We therefore update Fig. 5 of the original publication. The new calculation yields a significantly larger value of the Kerr lens focal length leading to a smaller perturbation of the cavity beam profile.

DOI: 10.1364/OE.435077
URL: https://doi.org/10.1364/OE.435077

Author's contributions:

I noticed the error in the calculation of the focal length, corrected the calculation and wrote the Erratum with the support of A. Rahimi-Iman and in accordance with the other coauthors.

Microcavity-enhanced Kerr nonlinearity in a vertical-external-cavity surface-emitting laser: erratum

CHRISTIAN KRISO,[1,*] SASCHA KRESS,[1] TASNIM MUNSHI,[1] MARIUS GROSSMANN,[2] ROMAN BEK,[2] MICHAEL JETTER,[2] PETER MICHLER,[2] WOLFGANG STOLZ,[1] MARTIN KOCH,[1] AND ARASH RAHIMI-IMAN[1,†]

[1]*Faculty of Physics and Materials Sciences Center, Philipps-Universität Marburg, D-35032 Marburg, Germany*
[2]*Institut für Halbleiteroptik und Funktionelle Grenzflächen, Universität Stuttgart, D-70569 Stuttgart, Germany*
**christian.kriso@physik.uni-marburg.de*
†a.r-i@physik.uni-marburg.de

Abstract: We correct a mistake in [Opt. Express 27, 11914-11929 (2019)] when calculating the focal length of the Kerr lens with the measured values of the nonlinear refractive index n_2 and parameters of a prototypical self-mode-locking VECSEL cavity. We therefore update Fig. 5 of the original publication. The new calculation yields a significantly larger value of the Kerr lens focal length leading to a smaller perturbation of the cavity beam profile.

To provide an estimation of the nonlinear focal strength of a possible Kerr lens in a VECSEL cavity given through the chip itself, the focal length of the Kerr lens is correctly calculated here using $f = w_0^2/(4n_2I_0d)$, with w_0 being the Gaussian beam radius on the VECSEL chip, d its effective length (thickness) and I_0 the peak irradiance (after Ref. [1], with on-axis index change n_2I_0 at that nonlinear element). The parameters w_0 and I_0 are extracted from the self-mode-locked cavity in Ref. [2] as 210 µm and 85.7 MW/cm^2, respectively. The latter value is calculated by $I_0 = 2P_{peak}/(\pi w_0^2 t)$ where P_{peak} is the pulse peak power measured outside the cavity as 950 W and $t = 0.016$ is the transmittance of the outcoupling mirror.

With this new calculation we obtain a minimum focal length of the Kerr lens between 5-6 m as plotted in the corrected Fig. 5 of the original publication below. This is significantly larger than the length of a typical VECSEL cavity. To provide an accordingly updated view on the assumed perturbation strength, we use the ABCD matrix formalism and model the Kerr lens as described in Ref. [3]. Taking the maximum nonlinear refractive index measured in Ref. [4], we correspondingly yield a maximum beam width reduction in the order of a few 0.1 % (a few per mill) in the cavity of Ref. [2]. We conclude that, therefore, achieving Kerr-lens mode-locking in such VECSEL cavities with a rather large mode spot size on the gain chip might be more delicate than previously thought. Yet, in VECSEL cavities operated close to the stability limit and with a smaller mode spot size on the gain chip, such as reported in Ref. [5], obtaining Kerr-lens mode-locking remains well imaginable with the sign and magnitude of the nonlinear refractive index measured in Ref. [4], from which one can yield a beam width modulation of a few percent.

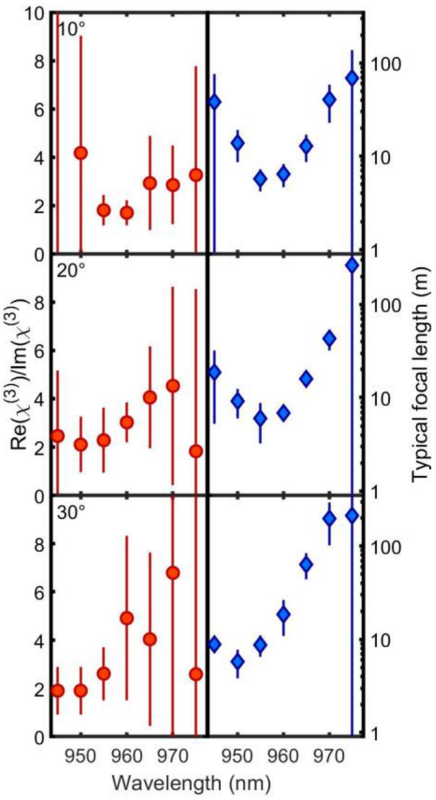

Fig. 1. Ratio of real and imaginary part of the measured third order nonlinearity $\chi^{(3)}$ and typical focal length of a Kerr-lens: The ratio of nonlinear refraction with respect to nonlinear absorption is plotted as a function of the wavelength in the left column of the diagram for the three different angles of incidence. Additionally, the focal length, which would occur in a typically self-mode-locked VECSEL configuration, is plotted here in the right column. The error bars stem from the errors in nonlinear absorption and refraction as depicted in Fig. 4 of the original publication.

References

1. M. Sheik-Bahae, A. A. Said, D. J. Hagan, M. J. Soileau, and E. W. Van Stryland, "Nonlinear refraction and optical limiting in thick media," Opt. Eng. **30**, 1228–1235 (1991).
2. M. Gaafar, P. Richter, H. Keskin, C. Möller, M. Wichmann, W. Stolz, A. Rahimi-Iman, and M. Koch, "Self-mode-locking semiconductor disk laser," Opt. Express **22**, 28390–28399 (2014).
3. V. Magni, G. Cerullo, and S. De Silvestri, "ABCD matrix analysis of propagation of gaussian beams through Kerr media," Opt. Commun. **96**, 348–355 (1993).
4. C. Kriso, S. Kress, T. Munshi, M. Großmann, R. Bek, M. Jetter, P. Michler, W. Stolz, M. Koch, and A. Rahimi-Iman, "Microcavity-enhanced Kerr nonlinearity in a vertical-external-cavity surface-emitting laser," Opt. Express **27**, 11914–11929 (2019).
5. A. R. Albrecht, Y. Wang, M. Ghasemkhani, D. V. Seletskiy, J. G. Cederberg, and M. Sheik-Bahae, "Exploring ultrafast negative Kerr effect for mode-locking vertical external-cavity surface-emitting lasers," Opt. Express **21**, 28801 (2013).

Wavelength- and pump-power dependent nonlinear refraction and absorption in a semiconductor disk laser

C. Kriso, S. Kress, T. Munshi, M. Grossmann, R. Bek, M. Jetter, P. Michler, W. Stolz, M. Koch, and A. Rahimi-Iman, IEEE Photonics Technology Letters 32, 85-88 (2020)

Abstract We characterize both nonlinear refraction and absorption in a vertical-external-cavity surface-emitting laser (VECSEL) as a function of pump irradiance over the whole range of lasing wavelengths. We observe an approximately linear decrease in magnitude for both nonlinear refraction and nonlinear absorption with optical pumping when the thermally induced shift of the lasing wavelength is considered. Our results are of particular significance for understanding self-modelocking of VECSELs which might be driven by nonlinear lensing.

DOI: 10.1109/LPT.2019.2957875
URL: `https://doi.org/10.1109/LPT.2019.2957875`

Author's contributions:

A. Rahimi-Iman initiated the investigation of nonlinear lensing in VECSELs. S. Kress built the first version of the Z-scan setup. I extended and improved the setup with the help of T. Munshi. W. Stolz provided a sample that was used to extensively test and improve the setup. M. Grossmann, R. Bek, M. Jetter and P. Michler provided the sample that was used for the measurements presented in this paper. I performed the measurements and analyzed the data. The manuscript was mainly written by me, with contributions from A. Rahimi-Iman, and was revised by the other coauthors. M. Koch and A. Rahimi-Iman supervised the work.

Wavelength and pump-power dependent nonlinear refraction and absorption in a semiconductor disk laser

C. Kriso, S. Kress, T. Munshi, M. Grossmann, R. Bek, M. Jetter, P. Michler, W. Stolz, M. Koch, and A. Rahimi-Iman

***Abstract*—We characterize both nonlinear refraction and absorption in a vertical-external-cavity surface-emitting laser (VECSEL) as a function of pump irradiance over the whole range of lasing wavelengths. We observe an approximately linear decrease in magnitude for both nonlinear refraction and nonlinear absorption with optical pumping when the thermally induced shift of the lasing wavelength is considered. Our results are of particular significance for understanding self-modelocking of VECSELs which might be driven by nonlinear lensing.**

***Index Terms*—Nonlinear refractive index, mode-locked semiconductor lasers, VECSELs, Z-scan**

[a]C. Kriso, S. Kress, T. Munshi, W. Stolz, M. Koch and A. Rahimi-Iman are with the Department of Physics and Materials Sciences Center, Philipps-Universität Marburg, 35032 Marburg, Germany (corresponding authors: christian.kriso@physik.uni-marburg, a.r-i@physik.uni-marburg.de).

M. Grossmann, R. Bek, M. Jetter, and P. Michler are with the Institut für Halbleiteroptik und Funktionelle Grenzflächen, Universität Stuttgart, 70569 Stuttgart, Germany.

I. Introduction

MODELOCKED vertical-external-cavity surface-emitting-lasers (VECSELs) have attracted much interest due to the high peak powers that can be achieved at GHz frequencies, rendering them very well suited for use in frequency combs and multi-photon imaging [1], [2]. Conventional modelocking of VECSELs typically relies on saturable absorbers as nonlinear elements, which passively modulate the loss in the laser cavity to generate ultrashort pulses [3]. Thereby, sub-100-fs pulses [4], [5] and pulses with peak powers of several kWs [6] have been generated.

Although these results show the success of saturable absorber modelocking, a saturable absorber – nowadays also implemented as an additional semiconductor structure integrated into the sub-cavity of the gain chip (the concept is referred to as MIXSEL [7]) – presents a significant complication of cavity or gain chip design and imposes restrictions on the operation wavelength. Moreover, semiconductor saturable absorber mirrors (SESAMs) suffer from degradation when exposed to high-power, ultra-short pulses, a phenomenon not completely understood yet but preventing long-term operation of ultrafast SESAM-modelocked VECSELs [8].

In light of these intrinsic drawbacks and unresolved issues, an alternative modelocking technique known as "self-modelocking" might enable further peak power scaling of modelocked VECSELs when better understood and optimized [9], [10]. In self-modelocked operation, the VECSEL emits ultrashort pulses without the use of a saturable absorber. Up to now, there exist several reports of self-modelocked VECSELs for different cavity designs and material systems [11]–[14]. It has been suggested that nonlinear lensing might drive these VECSELs into modelocking [13]. However, nonlinear lensing or refraction at resonant wavelengths in an inverted semiconductor system presents an intricate physical problem as complex carrier effects are superposed with the ultrafast electronic Kerr effect [15].

There have been several experimental investigations on nonlinear refraction in VECSELs provoked by recent self-modelocking demonstrations [16]–[18]. These investigations found such a strong nonlinear refraction in VECSEL gain chips to conclude that nonlinear-lens modelocking might indeed be a viable explanation for self-modelocking. Nonlinear lensing is a direct result of nonlinear refraction.

To further deepen our understanding of nonlinear refraction in VECSELs, we recently conducted Z-scan measurements of nonlinear refraction and absorption for several probe wavelengths around resonance. We found that the microcavity resonance in the gain chip strongly shapes the nonlinearity rendering it angle tunable [19]. These investigations were carried out without optical pumping. To investigate the influence of optical pumping, we perform here extensive characterization of nonlinear refraction in a VECSEL gain chip as a function of probe wavelength and continuous-wave (cw) pump irradiance. By probing a gain chip of the (InGa)As/Ga(AsP) material system, which was used in most self-modelocking demonstrations, we consider our results as highly relevant for understanding and improving self-modelocked operation in VECSELs.

II. Chip Characteristics and Measurement Setup

The epitaxial design of the gain chip is described in Ref. [19]. For lasing, the chip is mounted with an intracavity silicon carbide (4H SiC) heat spreader of 350 µm thickness onto a copper heat sink. Fig. 1 shows the power curve and the optical spectra of the gain chip in laser operation for a linear cavity with a highly reflective outcoupling mirror. Here, optical pumping with an 808 nm fiber-coupled diode laser was applied with a pump spot diameter on the chip of around 400 µm. To calculate

the pump irradiance for a given pump power we assume a flat top beam for the extraction of the pump spot radius on the gain chip. Also, all pump irradiances provided in this letter are net pump irradiances, that is the reflected pump power is subtracted from the total incident pump power and divided by the pump spot area.

The aim of our experiments is to probe the complex, effective third-order susceptibility $\chi^{(3)}$ of the gain chip in conditions similar to laser operation. $\chi^{(3)}$ contains the effective nonlinear refractive index n_2 and the nonlinear absorption coefficient β defined as $\Delta n=n_2 I_0$ and $\Delta\alpha=\beta I_0$, where Δn and $\Delta\alpha$ are the total, time-averaged nonlinear refractive index and absorption changes, respectively, and I_0 is the on-axis peak irradiance of the probe pulse. In the case of non-instantaneous nonlinearities, these relations are only an approximation whose validity has to be checked afterwards by confirming a linear dependency of refractive index and absorption change with incident power irradiance.

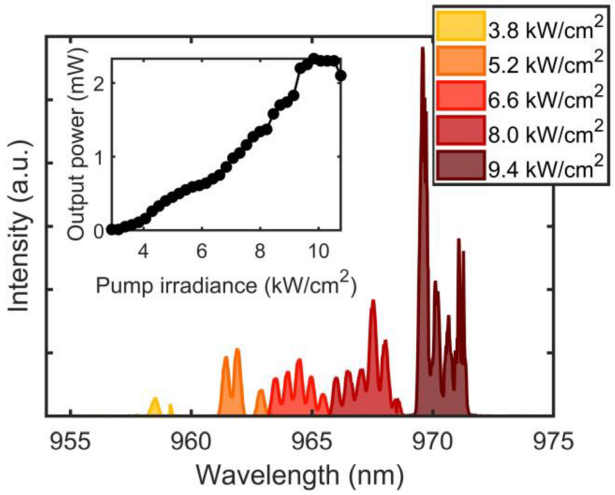

Fig. 1. Laser spectra of investigated VECSEL gain chip for different pump irradiances at 18°C heat sink temperature. The fringes in the spectrum are caused by the intracavity heat spreader's filter function. The inset shows a power curve at 18°C heat sink temperature.

The experimental setup for the subsequent investigations is shown in Fig. 2. It applies the Z-scan technique in reflection geometry [20]. A wavelength-tunable, modelocked Ti:sapphire laser is used to probe the nonlinear response of the gain chip over its whole lasing wavelength range. A fraction of the probe beam is split off and analyzed by a frequency-resolved optical-gating (FROG) device to confirm clean modelocked operation and determine the pulse length, which is important for the peak power calculation. The pulse length has been around 150 fs for all probe wavelengths. A neutral-density filter wheel is used to perform Z-scans systematically for different power densities to confirm the third-order nonlinear response. The probe beam is then focused with a lens of 30 mm focal length on the gain chip on the translation stage. The copper heat sink with gain chip is temperature stabilized with a Peltier element and subsequent water cooling. All Z-scan measurements have been performed at a heat sink temperature of 18°C. For optical pumping of the gain chip, the collimation and focusing optics of a fiber-coupled 808 nm diode laser are mounted on the stage and its output is aligned onto the probe spot. The pump spot diameter is 400 µm as used in the laser characterization. The probe-spot diameter in the focus is approximately 16 µm and thus significantly smaller. This guarantees that we monitor indeed the charge carrier density dependency of nonlinear refraction and absorption in the chip by assuming an approximately homogeneous spatial charge carrier density profile even outside the focus of the probe beam.

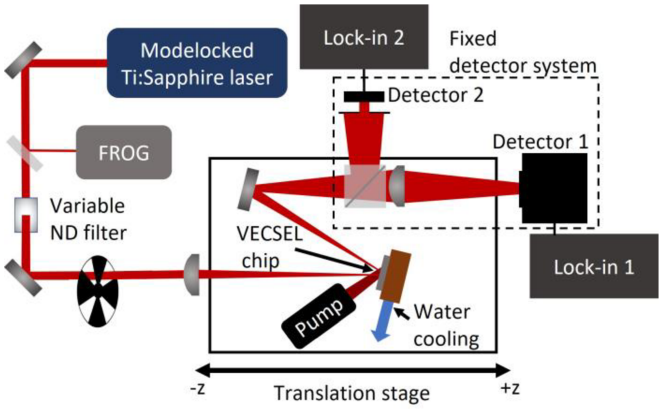

Fig. 2. Experimental Z-scan setup based on a wavelength-tunable, modelocked Ti:sapphire laser with FROG for pulse monitoring. The detector system, which is mounted off the stage, analyses the transmission as a function of the stage position with a partially closed and a fully open detector. Here, a cw pump laser allows the variation of the charge carrier density in the VECSEL chip.

Example Z-scan measurement results are displayed in Fig. 3. These scans have been recorded at a probe wavelength of 955 nm without optical pumping. The extraction follows the procedure as described in Ref. [19]. For the extraction of n_2, we use the relation $T_{pv}=0.406(1-S)^{0.25}|\Delta\Phi_0|$ [20] to relate the transmission difference T_{pv} of the Z-scan to the nonlinear on-axis phase shift $\Delta\Phi_0$. S is the power transmission ratio of the partially closed detector with respect to the open detector. By fitting $\Delta\Phi_0$ as a function of probe irradiance with a linear relationship, we deduce the nonlinear refractive index including the uncertainty as displayed in Fig. 4b.

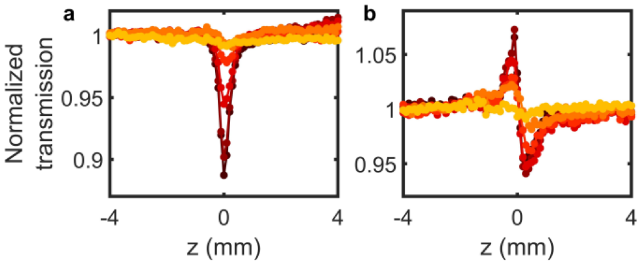

Fig. 3. Example Z-scan measurements at 955 nm without optical pumping. (a) Open aperture and (b) refractive-type Z-scan measurements for various peak probe irradiances (0.5 GW/cm^2, 4.3 GW/cm^2, 7.0 GW/cm^2, 13.5 GW/cm^2, 18.2 GW/cm^2, 19.2 GW/cm^2 from orange to black). A low irradiance background scan has been subtracted from all measurements. The Z-scans in (b) have been obtained by dividing the closed aperture Z-scan by the open aperture Z-scan to eliminate the effect of nonlinear absorption in (b).

III. Experimental results and discussion

Fig. 4a and b show the extracted values of nonlinear absorption and refraction of the gain chip as a function of the incident pump irradiance and probe wavelengths. Performing measurements without optical pumping before and after a pump-power series allows to assume the absence of any chip damage due to optical pumping. To evaluate the effect of the intracavity SiC heat spreader, we performed supplementary Z-scan measurements of only the heat spreader in transmission at around 955 nm probe wavelengths. This yields a positive nonlinear refractive index of the SiC heat spreader material of around $(1.6\pm0.4)\times10^{-15}$ cm^2/W. The positive nonlinear phase shift of the heat spreader counteracts the negative contributions from the gain chip in our measurements, which probe the average nonlinear phase shift of the bonded chip. To obtain only the nonlinear refraction of the gain chip in Fig. 4b, we have subtracted the estimated contribution of the positive nonlinear phase shift due to the heat spreader from the total measured nonlinear phase shift. However, as the standing field amplitude in the heat spreader is not known, the absolute value of n_2 in Fig. 4b is determined with a systematic uncertainty of $\pm3.6\times10^{-13}$ cm^2/W for all measurement points. This also includes the uncertainty of the nonlinear refractive index of SiC in our measurement. We have not included the systematic uncertainty in the individual error bars used in Fig. 5, as it does not affect the relative trend of the pump-dependent chip n_2 but would only lead to a constant offset for all values. Also, we cannot completely exclude thermal effects from our n_2 measurements. However, as the thermally-induced nonlinear refractive index change in GaAs and AlAs—representative for the gain chip materials—is positive around 1µm [21], the negative Kerr- and free-carrier-based nonlinearities are assumed to be the dominating effects. Moreover, we are particularly interested in the relative pump-dependent trends, which are not influenced by probe-induced thermal heating of the sample.

Figs. 4a and b show the nonlinear absorption coefficient β and nonlinear refractive index n_2, respectively, as a function of pump irradiance and probe wavelength.

When extracting the pump irradiance-dependent change of β and n_2, one has to consider that the laser spectrum red-shifts with increased pump irradiance as depicted in Fig. 1 due to heating of the chip.

In order to obtain the nonlinear optical properties of the gain chip at the lasing wavelength, which changes with increasing probe irradiance, we interpolate the β and n_2 values in Fig. 4 by the pump irradiance-dependent wavelength shift obtained from the laser spectra in Fig. 1, which are plotted at the bottom of Figs. 4a and b, respectively. In Figs. 5a and b, we then plot the interpolated β and n_2 as a function of pump irradiance, respectively. They specify the nonlinear absorption and refraction that become effective during laser operation.

Nonlinear absorption (Fig. 5a) decreases approximately linearly with increasing pump irradiance. The reduction of nonlinear absorption with increased carrier injection is consistent with the results of Ref. [22], where the change of absorption is attributed to the shift of the quasi-Fermi levels due to the quadratic Stark effect. Nonlinear refraction (Fig. 5b) also decreases in magnitude for increasing pump irradiance while remaining negative over the whole pump irradiance range.

Both, the ultrafast Kerr effect as well as carrier nonlinearities might contribute to the nonlinear refractive index [19].

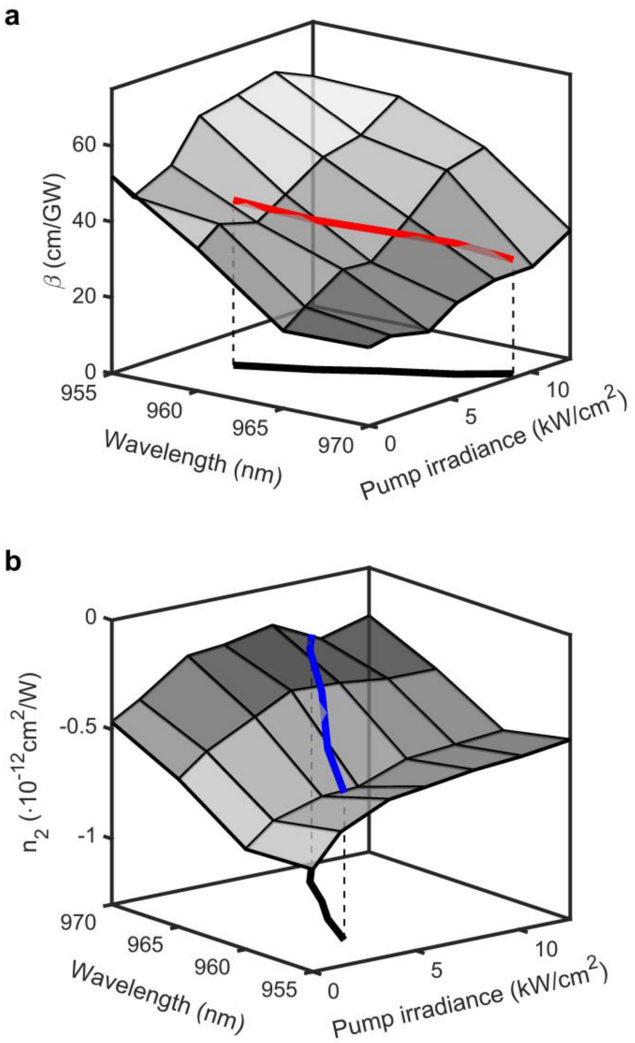

Fig. 4. (a) Nonlinear absorption β and (b) refraction n_2 as a function of net pump irradiance and probe wavelengths. The vertices represent actual measurement data. Note that the n_2 values contain an absolute uncertainty of $\pm3.6\times10^{-13}$ cm^2/W. The black line in the bottom of the figures displays the pump irradiance-dependent wavelength shift of the laser wavelength extracted from the spectra in Fig. 1. The red and blue lines are then the interpolated β and n_2 at these wavelengths and pump irradiances, respectively.

Comparing our results to investigations on nonlinearities in semiconductor optical amplifiers, we find that the decreasing trend of a negative n_2 with increasing pump irradiance matches well the theory of Sheik-Bahae and van Stryland [22] who calculate the dispersion of n_2 by Kramers-Kronig relations of nonlinear absorption changes in the presence of gain. The effective nonlinear refractive index of around -5×10^{-12} cm^2/W calculated for InGaAsP is around 5 times larger in magnitude than our values. The difference might be explained by the near antiresonant characteristics of the gain chip investigated here. Experiments have obtained similar values, with Ref. [23]

reporting values of a fast nonlinear refractive index between -3x10^{-12} cm^2/W and -2x10^{-12} cm^2/W.

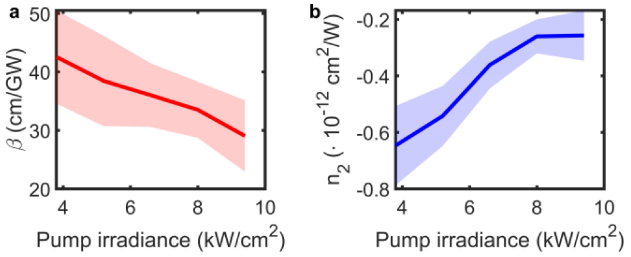

Fig. 5: (a) Nonlinear absorption β and (b) nonlinear refraction n_2 as a function of the pump irradiance, interpolated for lasing-relevant wavelengths as depicted in the diagram of Fig. 4. The shaded error bars are interpolated from individual errors of the data points in Fig. 4. These errors were obtained by fitting the normalized nonlinear absorption q_0 and the nonlinear phase shift Φ_0 as a linear function of peak probe irradiance according to Ref. [19] and taking the 95 % confidence bounds as error bars.

A comparison to Z-scan measurements at resonant wavelengths for a pumped VECSEL chip in Ref. [18] shows a similar trend for n_2 at small pump irradiances. For larger pump irradiances, the n_2 values fluctuate but stay within a range of -7x10^{-13} cm^2/W to -4.5x10^{-13} cm^2/W which is in good agreement with our results. The different trend of n_2 for larger pump irradiances might stem from the fact that the measurements in Ref. [18] have all been performed at a single wavelength and thus do not take into account the thermally induced band gap change as our results in Fig. 5 do.

The relatively strong change of n_2 with pump irradiance might complicate the design of a cavity of a stable, nonlinear-lens-modelocked VECSEL as the focal length of the nonlinear lens appears to strongly depend on the pump irradiance. This might also explain the results of Ref. [10], in which only for very specific, nearly discrete pump irradiances stable self-modelocking could be obtained.

IV. Conclusion

We presented comprehensive measurements of nonlinear absorption and refraction in a VECSEL chip with particular focus on its pump irradiance dependency at the laser wavelengths. Both, nonlinear absorption and refraction decrease with increasing pump irradiance which is consistent with prior investigations of resonant refractive index changes in semiconductor optical amplifiers and VECSELs. Our results might help to understand better the phenomenon of self-modelocking in VECSELs and will potentially facilitate their future design and application.

Acknowledgment

The authors acknowledge funding by the German Research Foundation under Grant No. DFG:RA2841/1-1, and thank M. Obaid for technical assistance.

References

[1] D. Waldburger *et al.*, “Tightly locked optical frequency comb from a semiconductor disk laser,” *Opt. Express*, vol. 27, no. 3, pp. 1786–1797, 2019.

[2] F. F. Voigt *et al.*, “Multiphoton in vivo imaging with a femtosecond semiconductor disk laser,” *Biomed. Opt. Express*, vol. 8, no. 7, p. 3213, 2017.

[3] M. A. Gaafar, A. Rahimi-Iman, K. A. Fedorova, W. Stolz, E. U. Rafailov, and M. Koch, “Mode-locked Semiconductor Disk Lasers,” *Adv. Opt. Photonics*, vol. 8, no. 3, pp. 370–400, 2016.

[4] D. Waldburger *et al.*, “High-power 100 fs semiconductor disk lasers,” *Optica*, vol. 3, no. 8, pp. 844–852, 2016.

[5] A. Laurain *et al.*, “Modeling and experimental realization of modelocked VECSEL producing high power sub-100 fs pulses,” *Appl. Phys. Lett.*, vol. 113, p. 121113, 2018.

[6] K. G. Wilcox, A. C. Tropper, H. E. Beere, D. A. Ritchie, B. Heinen, and W. Stolz, “4.35 kW peak power femtosecond pulse mode-locked VECSEL for supercontinuum generation,” *Opt. Express*, vol. 21, no. 2, pp. 1599–1605, 2013.

[7] D. J. H. C. Maas *et al.*, “Vertical integration of ultrafast semiconductor lasers,” *Appl. Phys. B Lasers Opt.*, vol. 497, pp. 493–497, 2007.

[8] S. Addamane, D. Shima, A. Laurain, H. Chan, G. Balakrishnan, and J. V Moloney, “Degradation mechanism of SESAMs under intense ultrashort pulses in,” *Proc. SPIE 10515*, vol. VECSELS VI, no. February, 2018.

[9] L. Kornaszewski, G. Maker, G. P. A. Malcolm, M. Butkus, E. Rafailov, and C. J. Hamilton, “SESAM-free mode-locked semiconductor disk laser,” *Laser Photonics Rev.*, vol. 6, pp. 20–23, 2012.

[10] M. Gaafar *et al.*, “Harmonic self-mode-locking of optically pumped semiconductor disc laser,” *Electron. Lett.*, vol. 50, no. 7, pp. 542–543, 2014.

[11] M. Gaafar *et al.*, “Self-mode-locking semiconductor disk laser,” *Opt. Express*, vol. 22, no. 23, pp. 28390–28399, 2014.

[12] M. Gaafar *et al.*, “Self-mode-locked quantum-dot vertical-external-cavity-surface-emitting laser,” *Opt. Lett.*, vol. 39, no. 15, pp. 4623–4626, 2014.

[13] A. R. Albrecht, Y. Wang, M. Ghasemkhani, D. V. Seletskiy, J. G. Cederberg, and M. Sheik-Bahae, “Exploring ultrafast negative Kerr effect for mode-locking vertical external-cavity surface-emitting lasers,” *Opt. Express*, vol. 21, no. 23, pp. 28801–28808, 2013.

[14] R. Bek *et al.*, “Self-mode-locked AlGaInP-VECSEL,” *Appl. Phys. Lett.*, vol. 111, p. 182105, 2017.

[15] D. N. Christodoulides, I. C. Khoo, G. J. Salamo, G. I. Stegeman, and E. W. Van Stryland, “Nonlinear refraction and absorption: mechanisms and magnitudes,” *Adv. Opt. Photonics*, vol. 2, pp. 60–200, 2010.

[16] A. H. Quarterman, M. A. Tyrk, and K. G. Wilcox, “Z-scan measurements of the nonlinear refractive index of a pumped semiconductor disk laser gain medium,” *Appl. Phys. Lett.*, vol. 106, p. 011105, 2015.

[17] E. A. Shaw *et al.*, “Nonlinear Lensing in an Unpumped Antiresonant Semiconductor Disk Laser Gain Structure,” *IEEE Photonics Technol. Lett.*, vol. 28, no. 13, pp. 1395–1398, 2016.

[18] A. H. Quarterman, S. Mirkhanov, C. J. C. Smyth, and K. G. Wilcox, “Measurements of nonlinear lensing in a semiconductor disk laser gain sample under optical pumping and using a resonant femtosecond probe laser,” *Appl. Phys. Lett.*, vol. 109, p. 121113, 2016.

[19] C. Kriso *et al.*, “Microcavity-enhanced Kerr nonlinearity in a vertical-external-cavity surface-emitting laser,” *Opt. Express*, vol. 27, no. 9, pp. 11914–11929, 2019.

[20] M. Sheik-Bahae, A. A. Said, T. H. Wei, D. J. Hagan, and E. W. Van Stryland, “Sensitive Measurement of Optical Nonlinearities Using a Single Beam,” *IEEE J. Quantum Electron.*, vol. 26, pp. 760–769, 1990.

[21] J. Talghader and J. S. Smith, “Thermal dependence of the refractive index of GaAs and AlAs measured using semiconductor multilayer optical cavities Thermal dependence of the refractive index of GaAs and AlAs measured using semiconductor multilayer optical cavities,” *Appl. Phys. Lett.*, vol. 66, pp. 335–337, 1994.

[22] M. Sheik-Bahae and E. W. Van Stryland, “Ultrafast nonlinearities in semiconductor laser amplifiers,” *Phys. Rev. B*, vol. 50, no. 19, pp. 171–178, 1994.

[23] K. L. Hall, A. M. Darwish, E. P. Ippen, U. Koren, and G. Raybon, “Femtosecond index nonlinearities in InGaAsP optical amplifiers,” *Appl. Phys. Lett.*, vol. 62, no. 12, pp. 1320–1322, 1993.

Probing the ultrafast gain and refractive index dynamics of a VECSEL

C. Kriso, T. Bergmeier, N. Giannini, A. R. Albrecht, M. Sheik-Bahae, S. Benis, S. Faryadras, E. W. Van Stryland, D. J. Hagan, M. Koch, G. Mette, and A. Rahimi-Iman, submitted to Applied Physics Letters, arXiv:2106.13664 (2021)

Abstract Typically, strong gain saturation and gain dynamics play a crucial role in semiconductor laser mode-locking. While there have been several investigations of the ultrafast gain dynamics in vertical-external-cavity surface-emitting lasers (VECSELs), little is known about the associated refractive index changes. Yet, such refractive index changes do not only have a profound impact on the pulse formation process leading to self-phase modulation, which needs to be compensated by dispersion, but they are also of particular relevance for assessing the feasibility of Kerr-lens mode-locking of VECSELs. Here, we measure both refractive index as well as gain dynamics of a VECSEL chip using the ultrafast beam deflection method. We find that, in contrast to the gain dynamics, the refractive index dynamics is dominated by an instantaneous (∼100 fs) and a very slow component (∼100 ps). The time-resolved measurement of nonlinear refraction allows us to predict a pulse-length dependent, effective nonlinear refractive index $n_{2,eff}$, which is shown to be negative and in the order of 10^{-16} m^2/W for short pulse lengths (∼100 fs) . It becomes positive for large excitation fluences and large pulse lengths (few ps). These results agree with some previous reports of self-mode-locked VECSELs for which the cavity design and pulse properties determine sign and strength of the nonlinear refractive index when assuming Kerr-lens mode-locking.

URL: `https://arxiv.org/abs/2106.13664`

Author's contributions:

I had the idea to perform the time-resolved measurements of nonlinear refraction of a VECSEL with the ultrafast beam deflection method. N. Giannini, A. R. Albrecht and M. Sheik-Bahae provided the sample. I performed the Z-scan measurements under the supervision of E. W. Van Stryland and D. J. Hagan. I performed the beam deflection measurements with strong support from T. Bergmeier and G. Mette. I analyzed the data with the help of S. Benis and S. Faryadras. The manuscript was mainly written by me, with contributions from A. Rahimi-Iman, and was revised by the other coauthors. M. Koch and A. Rahimi-Iman supervised the work.

Probing the ultrafast gain and refractive index dynamics of a VECSEL

C. Kriso,[1, a)] T. Bergmeier,[1] N. Giannini,[2] A. R. Albrecht,[2] M. Sheik-Bahae,[2] S. Benis,[3] S. Faryadras,[3] E. W. Van Stryland,[3] D. J. Hagan,[3] M. Koch,[1] G. Mette,[1] and A. Rahimi-Iman[1, b)]

[1)]*Department of Physics and Material Sciences Center, Philipps-Universität Marburg, Renthof 5, 35032 Marburg, Germany*

[2)]*Department of Physics and Astronomy, University of New Mexico, 210 Yale Blvd. NE, Albuquerque, New Mexico 87131, USA*

[3)]*CREOL, The College of Optics and Photonics, University of Central Florida, Orlando, FL 32816, USA*

(Dated: 25 June 2021)

Typically, strong gain saturation and gain dynamics play a crucial role in semiconductor laser mode-locking. While there have been several investigations of the ultrafast gain dynamics in vertical-external-cavity surface-emitting lasers (VECSELs), little is known about the associated refractive index changes. Yet, such refractive index changes do not only have a profound impact on the pulse formation process leading to self-phase modulation, which needs to be compensated by dispersion, but they are also of particular relevance for assessing the feasibility of Kerr-lens mode-locking of VECSELs. Here, we measure both refractive index as well as gain dynamics of a VECSEL chip using the ultrafast beam deflection method. We find that, in contrast to the gain dynamics, the refractive index dynamics is dominated by an instantaneous (∼100 fs) and a very slow component (∼100 ps). The time-resolved measurement of nonlinear refraction allows us to predict a pulse-length dependent, effective nonlinear refractive index $n_{2,eff}$, which is shown to be negative and in the order of $10^{-16}\ m^2/W$ for short pulse lengths (∼100 fs) . It becomes positive for large excitation fluences and large pulse lengths (few ps). These results agree with some previous reports of self-mode-locked VECSELs for which the cavity design and pulse properties determine sign and strength of the nonlinear refractive index when assuming Kerr-lens mode-locking.

Ultrashort-pulse mode-locking and frequency combs have emerged as a major topic in semiconductor laser research, and state-of-the-art semiconductor disk laser systems (or VECSELs) are under development that utilize passive mode-locking with various applications in mind such as spectroscopy, biomedicine, nonlinear optics and many more.[1–3] Mostly optically-pumped, VECSELs combine flexible wavelength design of the gain chip, high optical output powers and excellent beam quality.[4–6] The external cavity allows to further functionalize the laser emission, for example to achieve single-frequency generation or nonlinear frequency conversion by inserting optical filters or nonlinear crystals into the cavity, respectively.[7,8]

Mode-locking can routinely be achieved by inserting semiconductor-saturable absorber mirrors (SESAMs) into the cavity with the possibility of obtaining ultrashort pulses in the sub-100 fs regime as well as peak powers of several kilowatts.[9–11]

In this context, recently also saturable-absorber-free mode-locking, usually referred to as "self-mode-locking", has received considerable attention and has been demonstrated by several groups.[12–16] These results remain subject of ongoing debate within the community concerning what the driving mechanisms behind this phenomenon are, and whether those truly lead to a mode-locked state of the laser.[17–19] Both, mode-locking by a four-wave-mixing nonlinearity in the gain chip[19] and Kerr-lens mode-locking have been discussed as possible explanations.[14] In particular, the latter hypothesis triggered considerable efforts to characterize the nonlinear refractive index of the gain chip under realistic conditions, i.e. using probe irradiances and excitation fluences comparable to how they occur in a mode-locked VECSEL.[20–24] However, most of these investigations have been performed using pulse lengths of only a few hundreds of femtoseconds. Yet, pulses generated by self-mode-locked VECSELs usually are longer, that is in the few-ps regime down to sub-ps pulse durations.[18] Therefore, considering the strong gain dynamics of semiconductor lasers, which intrinsically affects the refractive index of the gain chip, such nonlinear lensing investigations so far have not provided a very accurate picture of the nonlinear refractive index of the gain chip. Time-resolved measurements of the refractive index dynamics of a VECSEL would therefore allow us to obtain a more realistic estimate of the strength of nonlinear lensing in VECSELs. Beyond this, it would allow us to obtain insight into the phase dynamics that affects a short pulse in VECSEL mode-locking. In phenomenological modeling of pulse formation, this is usually taken into account by introducing a constant, the linewidth enhancement factor, which relates gain changes to phase changes.[25,26] However, this is a strongly simplifying assumption and therefore the full knowledge of the refractive index dynamics might improve modeling significantly.

In this work, we measure the time-resolved nonlinear optical response of a gain chip using the recently developed ultrafast beam-deflection technique.[27] This uniquely enables us to simultaneously acquire gain as well as refractive index dynamics. Moreover, we validate the results by additional Z-scan measurements well known from effective nonlinear lensing characterization of materials without temporal resolution.[28]

Our pump-probe setup, including a prepulse for excitation

[a)]Electronic mail: christian.kriso@physik.uni-marburg.de
[b)]Electronic mail: a.r-i@physik.uni-marburg.de

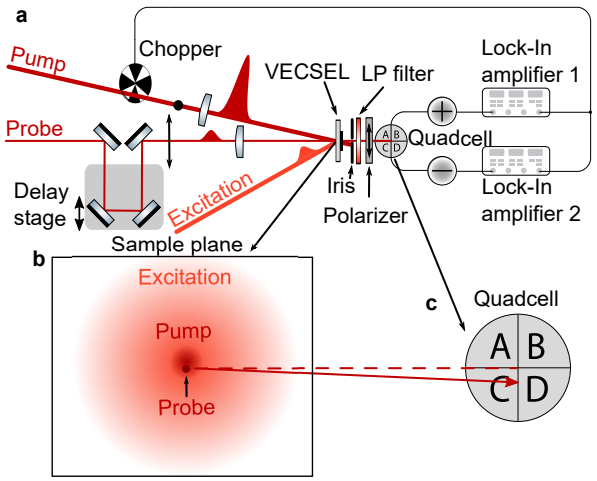

FIG. 1. (a) Beam-deflection setup for measuring time-resolved transmission and refractive index changes of the VECSEL. A prepulse (at 780 nm), arriving 100 ps before the pump-probe measurement (at 1150 nm) takes place, excites the sample. Two lock-in amplifiers are used to measure simultaneously the sum ("+") and difference ("-") signal of the segmented detector ("Quadcell"). (b) View on the sample (VECSEL) surface displaying the approximate size ratio and relative position of the spots of excitation as well as pump and probe beam. (c) The pump-induced refractive index change in the sample will lead to a deflection of the probe beam that will be detected by a non-zero difference signal between the upper and lower half of the segmented detector.

of the sample, is displayed in Fig. 1(a). Here, the probe spot is overlapped with the pump spot on the sample in a way that it sits exactly on the position of the largest slope of the Gaussian-shaped intensity profile of the pump as shown in Fig. 1(b) (which requires that the probe spot diameter is considerably smaller than the pump at the position of the sample). Consequently, the refractive index changes induced by the pump in the sample will lead to a deflection of the probe which is proportional to the refractive index change of the sample and can be detected by a segmented photodetector. In our scheme, we use lock-in detection to measure both pump-induced transmission changes by recording the sum-signal of the segmented detector and pump-induced deflection changes by recording the difference signal of the segmented detector. When varying the delay between pump and probe pulse, we can record time-resolved changes of transmission and deflection. For the beam deflection measurements, we used a 200 kHz femtosecond laser system (Light Conversion Carbide) pumping two optical parametric amplifiers (OPAs). With one OPA (Orpheus-F), we generated pulses at a center wavelength of 1163 nm and, with another OPA (Orpheus-N-2H), pulses at a center wavelength of 780 nm. The latter is used to excite the sample with a prepulse arriving at the sample about 100 ps before the pump-probe measurement takes place. For the pump-probe measurements, a filter with center wavelength of 1150 nm and a bandwidth of 25 nm was used to align the laser spectrum with respect to the photoluminesence of the VECSEL sample (shown in the Supplementary Material). The pump and probe beams are obtained by splitting the 1150 nm laser beam with a 90:10-beam splitter. A half-wave plate and calcite polarizers are used to ensure good orthogonal polarization of pump and probe with respect to each other. The probe beam is attenuated by neutral-density filters in order to prevent detector saturation. To block the pump from reaching the detector, an iris and a polarizer are used which only transmit the probe. The half width (HW)$1/e^2$ of the probe beam at its focus and of the pump spot at the same position is 29 µm and 97 µm, respectively. Both, the pump-induced transmission and deflection signal scale approximately linearly when increasing the pump irradiance, as was verified with reference samples (see the Supplementary Material). The spot size of the excitation is made a lot larger (with a HW1/e^2 of about 500 µm on the chip) to ensure an approximately homogeneous sample excitation at the area where the pump-probe measurement takes place. A long-pass filter is inserted after the sample to prevent the excitation beam at 780 nm from scattering into the detector.

The VECSEL sample used in this investigation consists of a resonant periodic gain structure of 10 InGaAs quantum wells separated by GaAsP barriers for strain compensation, and was grown by metalorganic chemical vapor deposition (MOCVD). Two InGaP layers of approximately 190 nm thickness surround the structure for charge carrier confinement. The sample used here is a distributed Bragg reflector (DBR)-free VECSEL or membrane external-cavity surface emitting laser (MECSEL). The GaAs growth substrate is etched away and the structure is van-der-Waals-bonded onto a 350 μm thick 4H-SiC heat spreader. MECSELs have been shown to exhibit an extraordinarily large wavelength tuning range and excellent thermal properties.[29–31] In this work, it enables us to conduct the beam deflection measurements in transmission geometry rather than in reflection which greatly simplifies the experiment.

In the following, we investigate beam deflection measurements for different excitation fluences ranging from 1.1 µJ to 21.2 µJ and a fixed pump peak irradiance (1 GW/cm^2). Figure 2(a) and (b) show the normalised pump-induced transmission changes $\Delta T/T$ and the deflection changes $\Delta E/E$ as a function of the delay between pump and probe pulse, respectively. Transmission changes ΔT are normalized with respect to the total signal of the probe in the absence of the pump, T, and deflection changes ΔE are normalized with respect to $E = T + \Delta T$, which also takes into account the transmission changes of the probe during the deflection measurement.

When the sample is only weakly excited, the probe pulse experiences first an increase of transmission before decaying back to a transmission change of close to zero. The deflection signal experiences a very fast negative response and subsequently a rather constant negative deflection signal over the few-ps time scale. Negative deflection corresponds to a negative refractive index change.

When the sample is strongly excited, the probe experiences first a strong decrease in transmission and subsequently a recovery to a slightly negative transmission change. This offset from zero transmission change at longer times indicates that the pump beam experiences net gain. Note that the

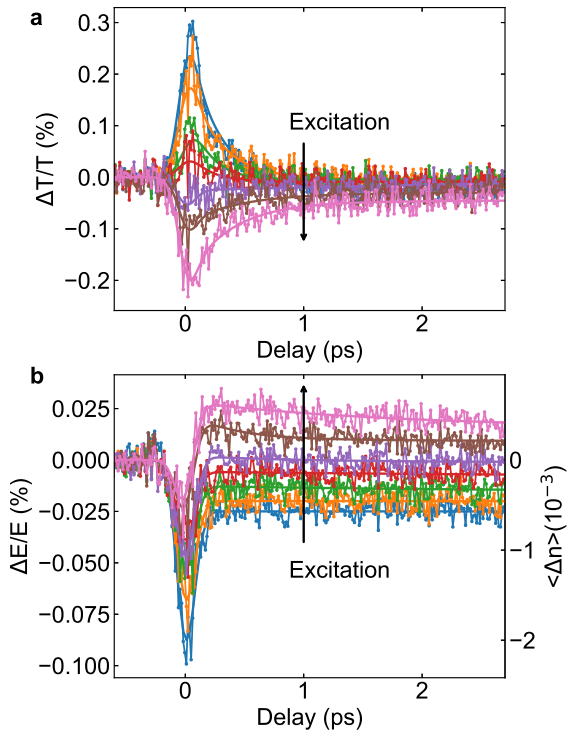

FIG. 2. (a) Normalized probe transmission and (b) deflection of VECSEL for a pump irradiance of 1 GW/cm^2 and various excitation fluences (1.1 µJ/cm^2, 2.8 µJ/cm^2, 6.0 µJ/cm^2, 8.7 µJ/cm^2, 10.2 µJ/cm^2, 13.0 µJ/cm^2 and 21.2 µJ/cm^2 in the direction of the arrow). The probe beam experiences increased transmission when the pump experiences absorption and opposite behavior in the case of gain. The solid line displays the model used to fit the data (Eq. 2). The right axis in (b) displays the refractive index change averaged over the width of the cross-correlation of pump and probe pulse (∼180 fs FWHM) that corresponds to the measured deflection.

probe beam will experience increased absorption when the pump experiences gain and opposite behavior in the case of absorption.[32] The deflection signal becomes positive for long time scales and large excitation fluences.
Both, transmission and deflection measurements can be modeled by a response function of the form,

$$R(t) = (b_0 e^{-\frac{t}{\tau_0}} + b_1 e^{-\frac{t}{\tau_1}})\theta(t) + b_2\delta(t), \qquad (1)$$

where $\theta(t)$ and $\delta(t)$ are the Heaviside and Dirac delta function, respectively. The time constant τ_0 models the non-instantaneous response of the sample consisting of carrier cooling in the absorption regime and carrier heating in the gain regime that occur with a time constant of several hundreds of fs. The time constant τ_1 is usually in the order of magnitude of hundreds of ps or few ns and describes carrier relaxation or refilling.[33] The instantaneous response described by the Dirac delta function models both contributions from two-photon absorption or the ultrafast Kerr effect as well as relaxation of the excited carriers into a Fermi-Dirac distribution in the absorption regime or filling of the spectral holes in the gain regime, which is too fast to be resolved by the measurement conducted with a pump and probe pulse with a full-width at half maximum (FWHM) of 130 fs, respectively.

This response function is fitted to the experimental traces by

$$\frac{\int_{-\infty}^{+\infty}\int_{-\infty}^{+\infty} R(t-t')I_{pu}(t')dt' I_{pr}(t-\tau)dt}{\int_{-\infty}^{+\infty} I_{pr}(t)dt}. \qquad (2)$$

Here, I_{pu} and I_{pr} represent the intensity envelope of the pump and probe pulse, respectively.

When fitting the pump-probe measurement of the transmission changes with Eqs. 1 and 2 one obtains a time constant τ_0 of 300-400 fs for carrier cooling, i.e. when the sample is in the absorption regime and only weakly excited. This corresponds to values measured in Ref.[34]. When the sample is strongly excited, this time constant increases slightly to 400-500 fs, corresponding to the time the carrier-distribution heats up to the lattice temperature. In comparison to the measurement of Ref.[35], the ultrafast gain recovery also contains a pronounced instantaneous component (∼100 fs) for large excitation fluences.

Interestingly, the effect of carrier cooling/heating, i.e. the component with a sub-ps time constant, is not very strong in the measurement of the deflection signal (Fig. 2(b)), as that signal mostly consists of an ultrafast (∼100 fs) and a very slow component (∼100 ps). In contrast to measurements of semiconductor optical amplifiers, the instantaneous negative decrease of the refractive index reduces significantly with increased excitation fluence, while otherwise the trend is similar.[32,36]

The time-resolved deflection measurement can be mapped to the refractive index change averaged over the length of the probe pulse, $<\Delta n(\tau)>$, where τ represents the delay between pump and probe pulse. This is done by comparing the deflection signal of the VECSEL to the deflection signal of a reference sample (SiC) with a known nonlinear refractive index n_2 (see the Supplementary Material for more details of this procedure). The right axis of Fig. 2(b) displays the corresponding $<\Delta n(\tau)>$ for the measurement of the VECSEL sample. The response function, obtained by fitting $<n(\tau)>$ to Eq. 2, can be used to calculate the effective nonlinear refractive index $n_{2,eff}$. This quantity describes the nonlinear refractive index that would be seen by a single beam propagating through the sample, for example when performing a Z-scan measurement, and depends on the pulse length. It relates to the total refractive index change by $\Delta n = n_{2,eff} I$, with I being the irradiance of the single beam. It can be calculated by[37]

$$n_{2,eff} = \frac{\int_{-\infty}^{+\infty}\int_{-\infty}^{+\infty} R(t-t')I(t')dt' I(t)dt}{\int_{-\infty}^{+\infty} I^2(t)dt}. \qquad (3)$$

Here, $I(t)$ is the intensity pulse envelope of the single beam. Fig. 3(a) shows the excitation-dependent $n_{2,eff}$ calculated from various deflection measurements with different pump irradiances for a pulse length of 1 ps. One can see that $n_{2,eff}$ is similar for all pump irradiances, being around $-6{\cdot}10^{-16}$ m^2/W for no excitation and increasing to slightly positive values of around $+2{\cdot}10^{-16}$ m^2/W for large excitation

fluences. The fact that $n_{2,eff}$, calculated for 1 ps, is approximately independent of the pump irradiance demonstrates the third-order character of the nonlinearity for both the instantaneous (∼100 fs) and the slower component (∼1 ps).

In addition to the beam deflection measurements, Z-scan measurements were performed on the unexcited sample, which yield an $n_{2,eff}$ of $-1.2{\cdot}10^{-16}$ m^2/W. This corresponds in sign and order of magnitude to the $n_{2,eff}$ of around $-3{\cdot}10^{-16}$ m^2/W calculated from the beam deflection measurements with the Z-scan pulse length of 121 fs. Furthermore, the trend of the refractive index change with increasing excitation was measured by Z-scan and is compared in Fig. 3(b) to the beam deflection measurement with relatively good agreement of both measurements. For details of the measurement of the excitation-induced refractive index change $\delta\Delta n$, we refer to the Supplementary Material. Also, we note that both the order of magnitude of $n_{2,eff}$ and the trend with increasing excitation correspond to previous measurements of nonlinear refraction in VECSELs as well as theoretical investigations.[21–24,38]

We proceed to calculate the pulse-length dependent $n_{2,eff}$ for several excitation fluences as shown in Fig. 3(c). It can be seen that, for low excitation fluences, $n_{2,eff}$ is negative for all pulse lengths and increases strongly in magnitude for pulse lengths larger than 1 ps. This is a consequence of the nearly constant refractive index change at longer delays as shown in Fig. 2(b). In contrast, for large excitation fluences, $n_{2,eff}$ changes sign from negative to positive when going to pulse lengths beyond 1000 fs.

It is interesting to compare the trend of the pulse-width-dependent, as well as the excitation-dependent, effective nonlinear refractive index with previous observations of self-mode-locking in VECSELs. In Ref.[14], self-mode-locking in a V-cavity was shown to possibly originate from a negative nonlinear refractive index in the order of 10^{-16} m^2/W. Interestingly, when increasing the pump power, the measured pulse width decreased from >1 ps to <500 fs which probably guarantees a negative effective nonlinear refractive index over the whole excitation range as shown by our investigations.

In Ref.[39], self-mode-locking was reported for a linear cavity. The insertion of a slit in front of the outcoupling mirror allows only assuming Kerr-lens mode-locking with a nonlinear lens of positive focal length. As the pulse length obtained in this experiment was 3.5 ps, a positive Kerr lens is indeed expected and thus the assumption of Kerr-lens mode-locking caused by a nonlinear refractive index in the order of 10^{-16} cm^2/W is justified.

Beyond assessing the feasibility of Kerr-lens mode-locking of VECSELs, transient nonlinear refractive index changes generally play a crucial role in modeling pulse formation of VECSELs as it causes chirped pulses. In the semi-classical approach used in Refs.[25,26] to model SESAM-mode-locking of VECSELs, the refractive index change induced by the changes in carrier occupation is modeled by the so-called linewidth-enhancement factor α, that relates transient pulse phase changes $\Delta\varphi(t)$ to the time-dependent gain $g(t)$,[25]

$$\Delta\varphi(t) = -\alpha g(t)/2. \tag{4}$$

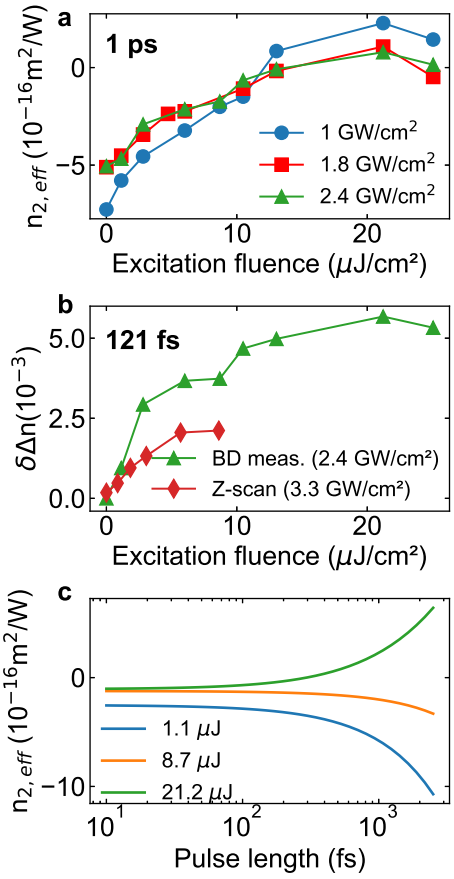

FIG. 3. (a) Effective, excitation-dependent, nonlinear refractive index $n_{2,eff}$ calculated for a pulse length (FWHM) of 1 ps and several pump peak irradiances. (b) Excitation-induced refractive index change $\delta\Delta n$ obtained from a Z-scan measurement conducted with a peak irradiance of 3.3 GW/cm^2 and a pulse length (FWHM) of 121 fs and the beam deflection measurement performed with 2.4 GW/cm^2 pump peak irradiance. (c) Calculated $n_{2,eff}$ as a function of the pulse length (FWHM) for different excitation fluences and a pump peak irradiance of 1 GW/cm^2. The calculation of $n_{2,eff}$ (Eq. 3) is based on the fitted response function of the nonlinear refractive index change.

However, our measurements show that the refractive index dynamics, which directly translates to the pulse phase changes via $\Delta\varphi(t) = k\Delta n(t)$, with k being the wave vector, differs significantly in shape and relative contributions of components with different time scales from the gain dynamics. Therefore, it appears useful to incorporate the response function of the refractive index measured here into pulse simulations for more realistic modeling instead of using the phenomenological parameter α.

In conclusion, we have probed both the gain and refractive index dynamics of a VECSEL chip under conditions similar to laser operation. Our results allow us to retrieve the response function of the refractive index change and to predict a pulse-length dependent effective nonlinear refractive index, which is negative and in the order of 10^{-16} m^2/W for sub-ps pulse lengths but becomes positive for large excitation

fluences and ps pulse lengths. These findings support the assumption of Kerr-lens mode-locking for some self-mode-locking results obtained with VECSELs. Additionally, our results might improve modeling of pulse formation in VECSELs by providing the time-resolved refractive index response of a VECSEL in the gain regime that could be directly incorporated into pulse-shaping simulations instead of a constant linewidth-enhancement factor.

See the Supplementary Material for further information about the VECSEL characterization and additional beam deflection as well as Z-scan measurements

The authors thank U. Höfer for providing the 200 kHz laser system. C.K. thanks all members of the Nonlinear Optics group at CREOL for outstanding support and useful discussions during his visit and acknowledges financial support by the Deutscher Akademischer Austauschdienst (DAAD). G.M. and T.B. gratefully acknowledge funding by the Deutsche Forschungsgemeinschaft (DFG) via Project-ID 223848855-SFB 1083 and GRK 1782. This work was funded by the DFG through project grants DFG RA 2841/1-1 and DFG RA 2841/1-3. This work was performed, in part, at the Center for Integrated Nanotechnologies, an Office of Science User Facility operated for the U.S. Department of Energy (DOE) Office of Science by Los Alamos National Laboratory (Contract 89233218CNA000001) and Sandia National Laboratories (Contract DE-NA-0003525).

DATA AVAILABILITY

The data that support the findings of this study are available from the corresponding author upon reasonable request.

[1] S. M. Link, D. J. H. C. Maas, D. Waldburger, and U. Keller, "Dual-comb spectroscopy of water vapor with a free-running semiconductor disk laser," Science **356**, 1164–1168 (2017).

[2] F. F. Voigt, F. Emaury, P. Bethge, D. Waldburger, S. M. Link, S. Carta, A. van der Bourg, F. Helmchen, and U. Keller, "Multiphoton in vivo imaging with a femtosecond semiconductor disk laser," Biomedical Optics Express **8**, 3213–3231 (2017).

[3] R. Bek, S. Baumgärtner, F. Sauter, H. Kahle, T. Schwarzbäck, M. Jetter, and P. Michler, "Intra-cavity frequency-doubled mode-locked semiconductor disk laser at 325 nm," Optics Express **23**, 19947–19953 (2015).

[4] M. Kuznetsov, F. Hakimi, R. Sprague, and A. Mooradian, "High-power (>0.5-W CW) diode-pumped vertical-external-cavity surface-emitting semiconductor lasers with circular TEM_{00} beams," IEEE Photonics Technology Letters **9**, 1063–1065 (1997).

[5] A. Rahimi-Iman, "Recent advances in VECSELs," Journal of Optics **18**, 093003 (2016).

[6] M. Guina, A. Rantamäki, and A. Härkönen, "Optically pumped VECSELs : review of technology and progress," Journal of Physics D: Applied Physics **50**, 383001 (2017).

[7] F. Zhang, B. Heinen, M. Wichmann, C. Möller, B. Kunert, A. Rahimi-iman, W. Stolz, and M. Koch, "A 23-watt single-frequency vertical-external-cavity surface-emitting laser," Optics Express **22**, 12817–12822 (2014).

[8] M. Scheller, J. M. Yarborough, J. V. Moloney, M. Fallahi, M. Koch, and S. W. Koch, "Room temperature continuous wave milliwatt terahertz source," Optics Expres **18**, 27112–27117 (2010).

[9] D. Waldburger, S. M. Link, M. Mangold, C. G. E. Alfieri, E. Gini, M. Golling, B. W. Tilma, and U. Keller, "High-power 100 fs semiconductor disk lasers," Optica **3**, 844–852 (2016).

[10] A. Laurain, I. Kilen, J. Hader, A. R. Perez, P. Ludewig, W. Stolz, G. Balakrishnan, S. W. Koch, and J. V. Moloney, "Modeling and experimental realization of modelocked VECSEL producing high power sub-100 fs pulses," Applied Physics Letters **113**, 121113 (2018).

[11] K. G. Wilcox, A. C. Tropper, H. E. Beere, D. A. Ritchie, B. Heinen, and W. Stolz, "4.35 kw peak power femtosecond pulse mode-locked VECSEL for supercontinuum generation," Optics Express **21**, 1599–1605 (2013).

[12] Y. F. Chen, Y. C. Lee, H. C. Liang, K. Y. Lin, K. W. Su, and K. F. Huang, "Femtosecond high-power spontaneous mode-locked operation in vertical-external cavity surface-emitting laser with gigahertz oscillation," Optics Letters **36**, 4581–4583 (2011).

[13] L. Kornaszewski, G. Maker, G. P. Malcolm, M. Butkus, E. Rafailov, and C. J. Hamilton, "SESAM-free mode-locked semiconductor disk laser," Laser and Photonics Review **6**, 20–23 (2012).

[14] A. R. Albrecht, Y. Wang, M. Ghasemkhani, D. V. Seletskiy, J. G. Cederberg, and M. Sheik-Bahae, "Exploring ultrafast negative Kerr effect for mode-locking vertical external-cavity surface-emitting lasers," Optics Express **21**, 28801–28808 (2013).

[15] M. Gaafar, P. Richter, H. Keskin, C. Möller, M. Wichmann, W. Stolz, A. Rahimi-Iman, and M. Koch, "Self-mode-locking semiconductor disk laser," Optics Express **22**, 28390–28399 (2014).

[16] R. Bek, M. Großmann, H. Kahle, M. Koch, A. Rahimi-Iman, M. Jetter, and P. Michler, "Self-mode-locked AlGaInP-VECSEL," Applied Physics Letters **111**, 182105 (2017).

[17] K. G. Wilcox and A. C. Tropper, "Comment on SESAM-free mode-locked semiconductor disk laser," Laser and Photonics Reviews **423**, 422–423 (2013).

[18] M. A. Gaafar, A. Rahimi-Iman, K. A. Fedorova, W. Stolz, E. U. Rafailov, and M. Koch, "Mode-locked Semiconductor Disk Lasers," Advances in Optics and Photonics **8**, 370–400 (2016).

[19] E. Escoto and G. Steinmeyer, "Pseudo Mode-Locking," Proc. SPIE 11263, Vertical External Cavity Surface Emitting Lasers (VECSELs) X **11263**, 1–3 (2020).

[20] A. H. Quarterman, M. A. Tyrk, and K. G. Wilcox, "Z-scan measurements of the nonlinear refractive index of a pumped semiconductor disk laser gain medium," Applied Physics Letters **106**, 011105 (2015).

[21] E. A. Shaw, A. H. Quarterman, A. P. Turnbull, T. Chen Sverre, C. R. Head, A. C. Tropper, and K. G. Wilcox, "Nonlinear Lensing in an Unpumped Antiresonant Semiconductor Disk Laser Gain Structure," IEEE Photonics Technology Letters **28**, 1395–1398 (2016).

[22] A. H. Quarterman, S. Mirkhanov, C. J. Smyth, and K. G. Wilcox, "Measurements of nonlinear lensing in a semiconductor disk laser gain sample under optical pumping and using a resonant femtosecond probe laser," Applied Physics Letters **109**, 121113 (2016).

[23] C. Kriso, S. Kress, T. Munshi, M. Großmann, R. Bek, M. Jetter, P. Michler, W. Stolz, M. Koch, and A. Rahimi-Iman, "Microcavity-enhanced Kerr nonlinearity in a vertical-external-cavity surface-emitting laser," Optics Express **27**, 11914–11929 (2019).

[24] C. Kriso, S. Kress, T. Munshi, M. Grossmann, R. Bek, M. Jetter, P. Michler, W. Stolz, M. Koch, and A. Rahimi-Iman, "Wavelength and Pump-Power Dependent Nonlinear Refraction and Absorption in a Semiconductor Disk Laser," IEEE Photonics Technology Letters **32**, 85–88 (2020).

[25] R. Paschotta, R. Häring, A. Garnache, S. Hoogland, A. C. Tropper, and U. Keller, "Soliton-like pulse-shaping mechanism in passively mode-locked surface-emitting semiconductor lasers," Applied Physics B: Lasers and Optics **75**, 445–451 (2002).

[26] O. D. Sieber, M. Hoffmann, V. J. Wittwer, M. Mangold, M. Golling, B. W. Tilma, T. Südmeyer, and U. Keller, "Experimentally verified pulse formation model for high-power femtosecond VECSELs," Applied Physics B: Lasers and Optics **113**, 133–145 (2013).

[27] M. R. Ferdinandus, H. Hu, M. Reichert, Z. Wang, D. J. Hagan, and E. W. Stryland, "Beam deflection measurement of time and polarization resolved nonlinear refraction," Optics Letters **38**, 3518–3521 (2013).

[28] M. Sheik-Bahae, A. A. Said, T. H. Wei, D. J. Hagan, and E. W. Van Stryland, "Sensitive Measurement of Optical Nonlinearities Using a Single Beam," IEEE Journal of Quantum Electronics **26**, 760–769 (1990).

[29] Z. Yang, A. R. Albrecht, J. G. Cederberg, and M. Sheik-Bahae, "Optically pumped DBR-free semiconductor disk lasers," Optics Express **23**, 2419–2421 (2015).

[30]H. Kahle, C. M. N. Mateo, U. Brauch, P. Tatar-Mathes, R. Bek, M. Jetter, T. Graf, and P. Michler, "Semiconductor membrane external-cavity surface-emitting laser (MECSEL)," Optica **3**, 1506–1512 (2016).

[31]Z. Yang, D. Follman, A. R. Albrecht, P. Heu, N. Giannini, G. D. Cole, and M. Sheik-Bahae, "16 W DBR-free membrane semiconductor disk laser with dual-SiC heatspreader," Electronics Letters **54**, 430–432 (2018).

[32]K. Hall, J. Mark, E. Ippen, and G. Eisenstein, "Femtosecond gain dynamics in InGaAsP optical amplifiers," Applied Physics Letters **56**, 1740–1742 (1990).

[33]J. Mork and A. Mecozzi, "Response function for gain and refractive index dynamics in active semiconductor waveguides," Applied Physics Letters **65**, 1736–1738 (1994).

[34]C. G. E. Alfieri, D. Waldburger, S. M. Link, E. Gini, M. Golling, G. Eisenstein, and U. Keller, "Optical efficiency and gain dynamics of modelocked semiconductor disk lasers," Optics Express **25**, 2719–2721 (2017).

[35]C. Baker, M. Scheller, S. W. Koch, A. R. Perez, W. Stolz, R. Jason Jones, and J. V. Moloney, "In situ probing of mode-locked vertical-external-cavity-surface-emitting lasers," Optics Letters **40**, 5459–5462 (2015).

[36]J. Mork, A. Mecozzi, and C. Hultgren, "Spectral effects in short pulse pump-probe measurements," Applied Physics Letters **68**, 449–451 (1995).

[37]M. Reichert, H. Honghua, M. R. Ferdinandus, M. Seidel, P. Zhao, T. R. Ensley, D. Peceli, J. M. Reed, D. A. Fishman, S. Webster, D. J. Hagan, and E. W. Van Stryland, "Temporal, spectral, and polarization dependence of the nonlinear optical response of carbon disulfide," Optica **1**, 436–445 (2014).

[38]M. Sheik-Bahae and E. Van Stryland, "Ultrafast nonlinearities in semiconductor laser amplifiers," Physical Review B **50**, 171–178 (1994).

[39]A. Rahimi-Iman, M. Gaafar, C. Möller, M. Vaupel, F. Zhang, D. Al-nakdali, K. A. Fedorova, W. Stolz, E. U. Rafailov, and M. Koch, "Self-Mode-Locked Vertical-External-Cavity Surface-Emitting Laser," in *Proc. SPIE 9734, Vertical External Cavity Surface Emitting Lasers (VECSELs) VI, 97340M* (2016).

Supplementary Material: Probing the ultrafast gain and refractive index dynamics of a VECSEL

C. Kriso[1], T. Bergmeier[1], N. Giannini[2], A. R. Albrecht[2], M. Sheik-Bahae[2], S. Benis[3], S. Faryadras[3], E. W. Van Stryland[3], D. J. Hagan[3], M. Koch[1], G. Mette[1], and A. Rahimi-Iman[1]

[1]Department of Physics and Material Sciences Center, Philipps-Universität Marburg, Renthof 5, 35032 Marburg, Germany
[2]Department of Physics and Astronomy, University of New Mexico, 210 Yale Blvd. NE, Albuquerque, New Mexico 87131, USA
[3]CREOL, The College of Optics and Photonics, University of Central Florida, Orlando, FL 32816, USA

June 25, 2021

1 Sample properties and pump/probe laser spectrum

We used white-light transmission spectroscopy to characterize the absorption properties of the VECSEL sample. The result is displayed in Fig. 1(a). Below 800 nm, nearly all light gets absorbed while, at the lasing wavelength of 1150 nm, the transmission amounts to nearly 60%. The fringe-pattern on top of the absorption spectrum is due to the Fabry-Pérot effect of the SiC substrate (350 μm thickness). Also displayed in Fig. 1 is the sample photoluminescence (PL) when excited with a pulsed laser at 775 nm and which indicates the lasing wavelength. It can be seen that the peak of the PL spectrum overlaps very well with the spectrum of the pump and probe pulses used for the beam deflection measurements.

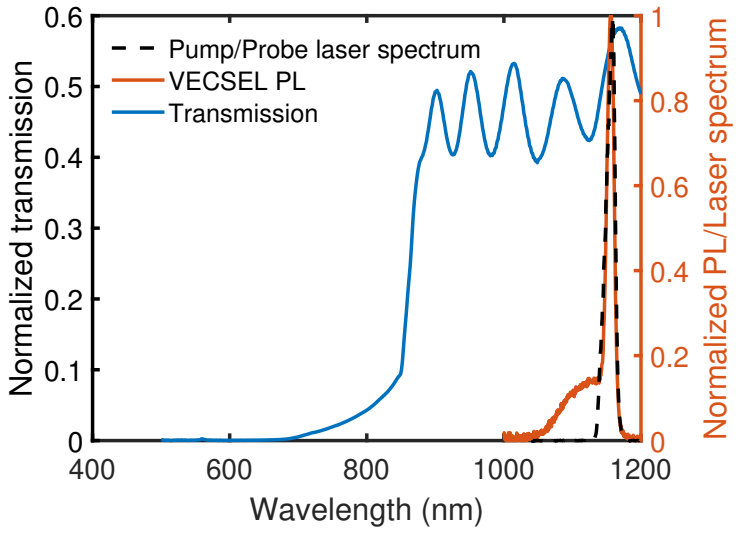

Supplementary Figure 1: Transmission and photoluminescence (PL) spectrum of VECSEL sample (left and right axis, respectively), as well as laser spectrum of pump and probe beam (right axis).

2 Reference beam deflection measurements of GaAs and SiC

We performed beam deflection measurements with reference samples to assure that both the transmission and the deflection amplitude scale linearly with increasing pump irradiance for a sample exhibiting an ultrafast $\chi^{(3)}$ nonlinearity. These measurements had been performed directly before the measurements on the VECSEL sample that are shown in the main text. Therefore, the alignment was identical and the pump-probe wavelength was also centered at 1150 nm. For the transmission measurement, we used a 600 μm thick GaAs wafer piece. Figure 2(a) shows measured transmission data for several pump peak irradiances. When the amplitude of the Gaussian fit to these experimental curves is plotted as a function of the pump peak irradiance (Fig. 2(b)), we see a good linear trend as expected for a sample exhibiting only two-photon absorption. Also, the pulse width can be estimated from these measurements as approximately 130 fs (FWHM). Figure 2(c) shows deflection measurements of the 350 μm thick 4H-SiC sample used as substrate of the VECSEL sample. Here as well, it can be seen that the deflection amplitude obtained from a Gaussian fit to the measurement data scales approximately linearly with pump peak irradiance (Fig. 2(d)). Thus, we can map the deflection of the probe beam to pump-induced refractive index changes of the sample. The slope of the linear interpolation function (0.03) in Fig. 2(d) provides the conversion factor between deflection and refractive index change. With the nonlinear refractive index of SiC as the reference material ($n_2(SiC)$) and the thickness of both SiC and VECSEL sample known ($L(SiC)$ and $L(VECSEL)$, respectively), one can map the deflection changes $\frac{\Delta E}{E}(VECSEL)$ to a refractive index change averaged over the width of the cross-correlation of pump and probe pulse,

$$< \Delta n(VECSEL) >= \frac{\Delta E}{E}(VECSEL) \cdot \frac{n_2(SiC)}{0.03} \cdot \frac{L(SiC)}{L(VECSEL)}. \quad (1)$$

Here, $L(SiC)$=350 μm, $L(VECSEL)$=2.3 μm and $n_2(SiC)$=+4.5x10^{-19} m^2/W, which was obtained from Z-scan measurements (see Section 3 of the Supplementary M) and matches coarsely theoretical predictions of being approximately +1x10^{-18} m^2/W [1].

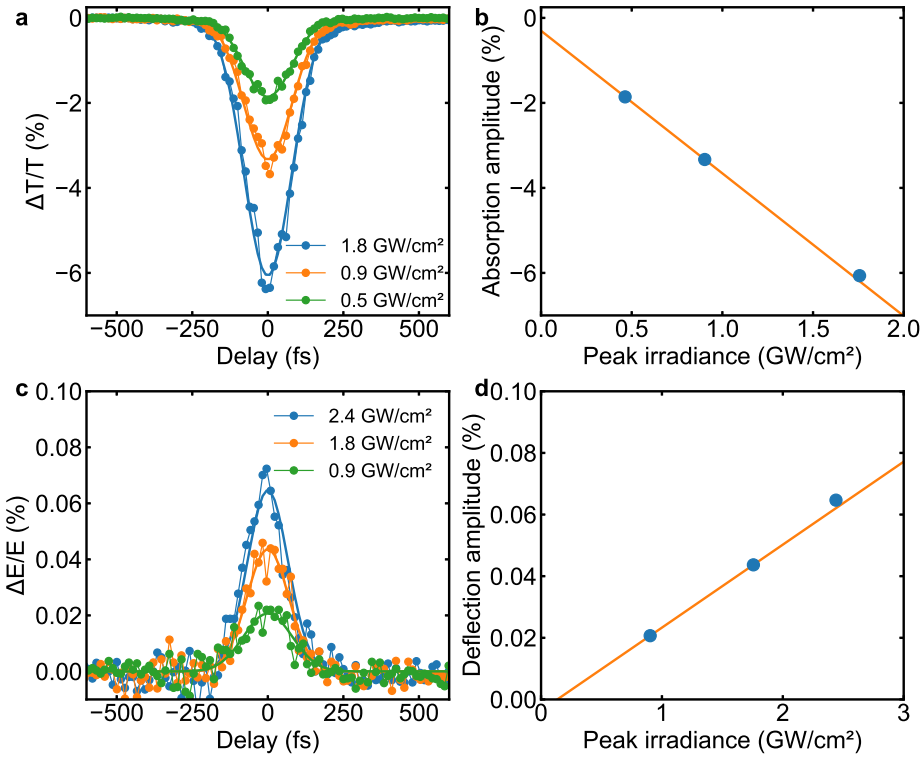

Supplementary Figure 2: (a) Normalized pump-probe transmission measurements of a 600 μm thick GaAs sample conducted at 1150 nm pump/probe wavelength for various pump peak irradiances. The solid lines describe a fit to the two-photon absorption dip with a Gaussian function. (c) Normalized pump-probe deflection measurements of a 350 μm thick 4H-SiC sample conducted at 1150 nm pump/probe wavelength for various pump peak irradiances. The solid lines describe a fit to the normalized deflection change with a Gaussian function. (b) and (d) plot the amplitude of the Gaussian fit curves from (a) and (c) as a function of the pump peak irradiance. Orange lines represent linear fits to the corresponding data points.

3 Beam deflection measurements at pump peak irradiances of 1.8 and 2.4 GW/cm^2

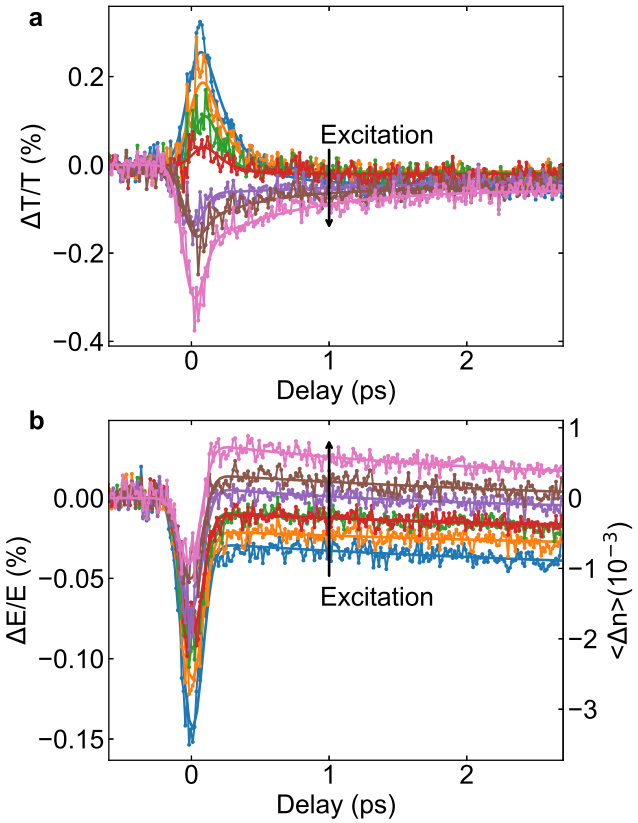

Supplementary Figure 3: (a) Normalized probe transmission and (b) deflection of the VECSEL for a pump peak irradiance of 1.8 GW/cm^2 and various excitation fluences (1.1 µJ/cm^2, 2.8 µJ/cm^2, 4.7 µJ/cm^2, 6.0 µJ/cm^2, 10.5 µJ/cm^2, 13.0 µJ/cm^2 and 21.2 µJ/cm^2 in the direction of the arrow). The solid line represents the model used to fit the data (Eq. 2 of the main text). The right axis in (b) displays the mean refractive index change time-averaged over the width of the cross-correlation of pump and probe pulse (∼180 fs) that corresponds to the measured deflection.

Figures 3 and 4 show the beam deflection experiments performed for the sample at pump peak irradiances of 1.8 GW/cm^2 and 2.4 GW/cm^2, respectively. These measurements are used to calculate the effective nonlinear refractive index $n_{2,eff}$ in Fig. 3(a) of the main text.

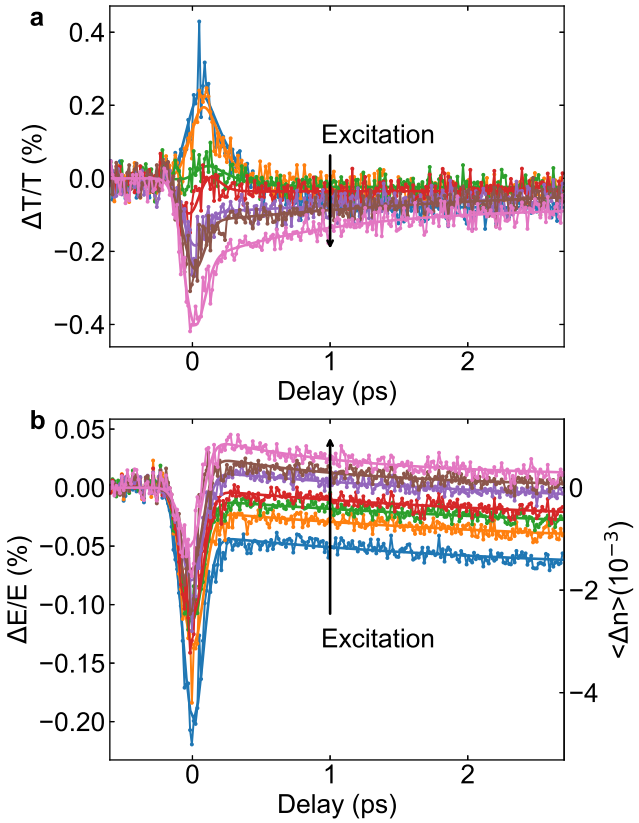

Supplementary Figure 4: (a) Normalized probe transmission and (b) deflection of the VECSEL for a pump peak irradiance of 2.4 GW/cm^2 and various excitation fluences (1.1 µJ/cm^2, 2.8 µJ/cm^2, 6.0 µJ/cm^2, 8.7 µJ/cm^2, 10.5 µJ/cm^2, 13.0 µJ/cm^2 and 21.2 µJ/cm^2 in the direction of the arrow). The solid line represents the model used to fit the data (Eq. 2 of the main text). The right axis in (b) displays the mean refractive index change time-averaged over the width of the cross-correlation of pump and probe pulse (∼180 fs) that corresponds to the measured deflection.

4 Z-scan measurements of VECSEL chip and SiC substrate

In addition to the degenerate beam deflection measurements, we performed Z-scan measurements (after Ref. [2]) of the here employed VECSEL sample in transmission geometry. These measurements can then be directly compared to the effective nonlinear refractive index $n_{2,eff}$ calculated from the beam deflection measurements for the pulse length corresponding to that of the Z-scan experiment. Figure 5(a) and (b) show Z-scan measurements of the nonlinear absorption and nonlinear refraction, respectively, for various peak irradiances. By fitting these experimental data with the model functions detailed in Ref. [2], one obtains a nonlinear absorption coefficient $\beta = 32{\cdot}10^{-11}$ m^2/W and an effective nonlinear refractive index $n_{2,eff} = -1.2{\cdot}10^{-16}$ m^2/W. Here, the pulse length of the probe beam used in the Z-scan measurement is around 121 fs (FWHM). These pulses are generated by an optical parametric amplifier (OPA) that is driven by a 1 kHz amplifier system. The output of the OPA is filtered by the same 1150 nm bandpass filter that is used for the beam deflection measurements in the main text.

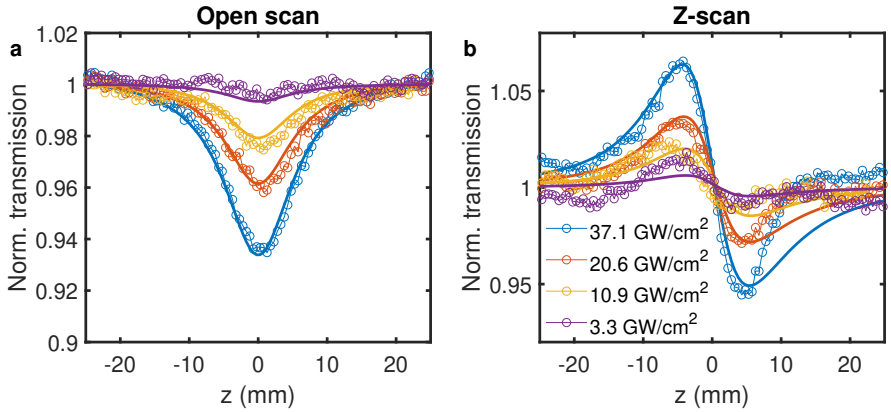

Supplementary Figure 5: (a) Open scan (measuring nonlinear absorption) and (b) Z-scan (measuring nonlinear refraction) of the bare VECSEL chip with fit functions (solid lines) for various peak irradiances of the probe beam (1150 nm). Accordingly, the effect of the SiC substrate has been subtracted from the measured data.

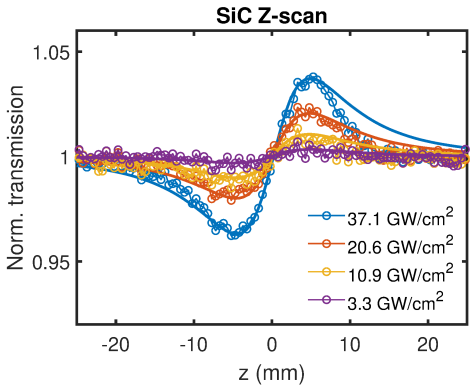

Supplementary Figure 6: Similarly performed Z-scan measurement of the VECSEL-attached SiC substrate at 1150 nm, yielding a nonlinear refractive index n_2 of $+4.5\text{x}10^{-19}$ m^2/W.

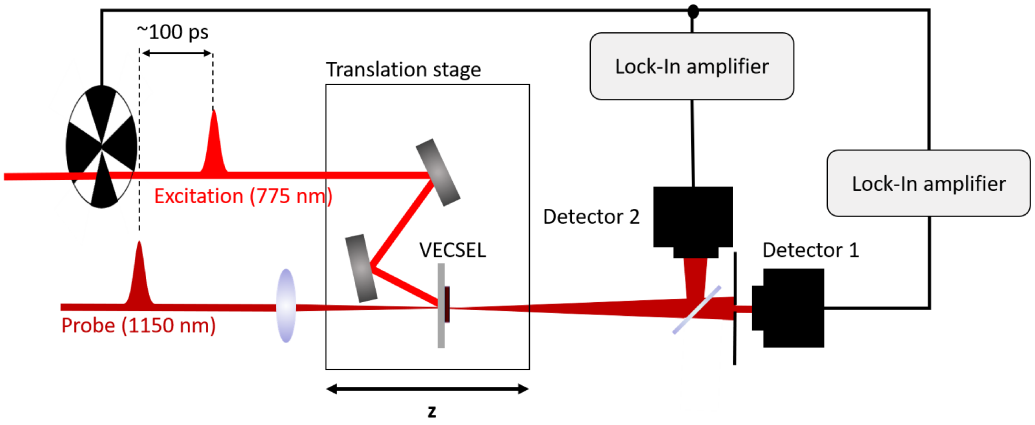

Supplementary Figure 7: Z-scan setup for the measurement of excitation-induced refractive index changes.

In order to account for the effect of the SiC substrate, onto which the VECSEL chip is bonded, Z-scan measurements with the same probe irradiance were performed for both the SiC-mounted VECSEL, which necessarily includes the effect of the SiC substrate in all transmission measurements, as well as only the SiC substrate. When the measured data for SiC is substracted from the data obtained for the VECSEL, (performed with the same irradiance and alignment) only the nonlinear optical properties of the bare VECSEL chip without SiC attachment can be obtained. Such measurements are shown in Fig. 5 for several probe peak irradiances.

Figure 6 shows Z-scan measurement data for the SiC substrate which yield a nonlinear refractive index of $n_2 = +4.5{\cdot}10^{-19}$ m^2/W. This value is used as reference for the beam deflection measurements (see Section 2 of the Supplement). One should note here that the Z-scan measurements are significantly less sensitive than the beam deflection measurements [2, 3]. Correspondingly this makes it difficult to measure the effect of optically exciting the sample for those probe irradiances, which are somehow comparable to typical intracavity peak irradiances experienced by mode-locked VECSELs. In order to overcome this problem, we use lock-in detection to measure only the excitation-induced changes of the refractive index of the sample. The corresponding setup is shown in Fig. 7. A laser beam at 775 nm is aligned in parallel with the probe beam at 1150 nm, and therefore also to the direction of movement of the translation stage. The radius of the 775 nm beam on the sample is made much larger than the radius of the 1150 nm beam at the off-focus position of the Z-scan to ensure that the probe beam experiences an approximately spatially homogeneous excitation of the sample.

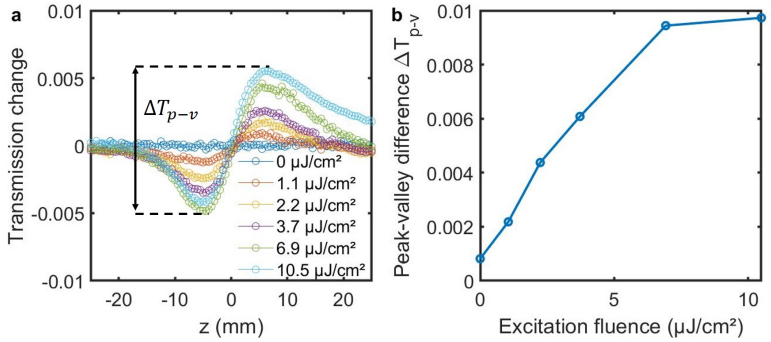

Supplementary Figure 8: (a) Transmission changes of VECSEL Z-scans with a probe peak irradiance of 3.3 GW/cm^2 for different excitation fluences. (b) Peak-to-valley difference of the experimental data in (a) as a function of the excitation fluence.

The resulting Z-scan measurements are displayed in Fig. 8(a) for a peak probe irradiance of 3.3 GW/cm^2. While the excitation-induced refractive index change is obviously zero for no excitation, it becomes positive for increasing excitation fluence. The peak-to-valley difference of the excitation-induced Z-scan measurement ΔT_{p-v} is plotted in Fig. 8(b) as a function of the excitation fluence. It saturates for fluences of around 10 $\mu J/\text{cm}^2$. ΔT_{p-v} can be related to the excitation-induced refractive index change
$\delta\Delta n =< \Delta n_{excited} > - < \Delta n_{unexcited} >$ by [2]

$$\delta\Delta n \approx \frac{\Delta T_{p-v}}{0.406kL(VECSEL)}, \tag{2}$$

where k is the wavenumber of the probe beam. This quantity can be compared to the beam deflection measurements. For this, we calculate the effective nonlinear refractive index $n_{2,eff}$ from the response function, retrieved by the beam deflection measurements, for the Z-scan pulse length of 121 fs and obtain the refractive index change by $< \Delta n >= n_{2,eff} I_0$, with I_0 being the peak irradiance of the pump beam in the beam deflection measurements. Subtracting from this quantity the refractive index change at zero excitation yields $\delta\Delta n$. The comparison of $\delta\Delta n$ obtained from Z-scan and beam deflection is shown in Fig. 3(b) of the main document.

References

[1] F. De Leonardis, R. A. Soref, and V. M. Passaro, "Dispersion of nonresonant third-order nonlinearities in Silicon Carbide," *Scientific Reports*, vol. 7, p. 40924, 2017.

[2] M. Sheik-Bahae, A. A. Said, T. H. Wei, D. J. Hagan, and E. W. Van Stryland, "Sensitive Measurement of Optical Nonlinearities Using a Single Beam," *IEEE Journal of Quantum Electronics*, vol. 26, no. 4, pp. 760–769, 1990.

[3] M. R. Ferdinandus, H. Hu, M. Reichert, Z. Wang, D. J. Hagan, and E. W. Stryland, "Beam deflection measurement of time and polarization resolved nonlinear refraction," *Optics Letters*, vol. 38, no. 18, pp. 3518–3521, 2013.

Signatures of a frequency-modulated comb in a VECSEL

C. Kriso, A. Barua, O. Mohiuddin, C. Möller, A. Ruiz-Perez, W. Stolz, M. Koch, and A. Rahimi-Iman, Optica 8, 458-463 (2021)

Abstract Optical frequency combs based on mode-locked lasers have revolutionized many areas of science and technology, such as precision metrology, optical frequency synthesis, and telecommunications. In recent years, a particular kind of frequency comb has been observed in edge-emitting semiconductor lasers where the phase difference between longitudinal laser modes is fixed but not zero. This results in a linearly chirped output in the time domain with nearly constant intensity. Here, by using coherent beatnote spectroscopy, we show that such a comb regime can also exist in vertical-external-cavity surface-emitting lasers, as evidenced for a specific part of the laser spectrum. Our findings may not only lead to a better understanding of the physics of frequency-modulated combs but also enable comb applications with hig hoptical power per comb line and flexible emission wavelengths.

DOI: 10.1364/OPTICA.418061
URL: `https://doi.org/10.1364/OPTICA.418061`

Author's contributions:

I had the initial idea of using SWIFTS to investigate self-mode-locking and FM comb generation in VECSELs. I built the SWIFTS setup and performed and analyzed the measurements. A. Barua and O. Mohiuddin built the dispersion measurement setup and performed the GDD measurements with support from me. C. Möller provided the matrix program that was used to calculate the GDD. A. Ruiz-Perez and W. Stolz provided the VECSEL chip. The manuscript was mainly written by me, with contributions from A. Rahimi-Iman, and was revised by the other coauthors. M. Koch and A. Rahimi-Iman supervised the work.

optica

Signatures of a frequency-modulated comb in a VECSEL

Christian Kriso,* Avijit Barua, Obaid Mohiuddin, Christoph Möller, Antje Ruiz-Perez, Wolfgang Stolz, Martin Koch, and Arash Rahimi-Iman

Department of Physics and Material Sciences Center, Philipps-Universität Marburg, Renthof 5, 35032 Marburg, Germany
**Corresponding author: christian.kriso@physik.uni-marburg.de*

Received 18 December 2020; revised 14 February 2021; accepted 15 February 2021 (Doc. ID 418061); published 1 April 2021

Optical frequency combs based on mode-locked lasers have revolutionized many areas of science and technology, such as precision metrology, optical frequency synthesis, and telecommunications. In recent years, a particular kind of frequency comb has been observed in edge-emitting semiconductor lasers where the phase difference between longitudinal laser modes is fixed but not zero. This results in a linearly chirped output in the time domain with nearly constant intensity. Here, by using coherent beatnote spectroscopy, we show that such a comb regime can also exist in vertical-external-cavity surface-emitting lasers, as evidenced for a specific part of the laser spectrum. Our findings may not only lead to a better understanding of the physics of frequency-modulated combs but also enable comb applications with high optical power per comb line and flexible emission wavelengths.

https://doi.org/10.1364/OPTICA.418061

1. INTRODUCTION

An optical frequency comb consists of equidistantly spaced laser lines. What distinguishes it from a free-running multi-mode laser is the fact that there exists a fixed phase relationship between adjacent longitudinal modes oscillating in the laser resonator. This guarantees that the frequency spacing between different modes does not change with time. Historically, such mode locking has been achieved by the use of strongly intensity-dependent elements in the laser cavity where saturable absorption provides a coupling mechanism between laser modes, which typically results in ultrashort pulses in the time domain and can be understood as in-phase synchronization of laser modes [1,2]. However, frequency-comb generation in a semiconductor laser can also occur in the absence of a saturable absorber [3,4]. In this case, it is understood that the beating of different laser modes leads to oscillations of the carrier density in the gain medium at multiples of the repetition frequency (corresponding to longitudinal mode spacing), which in turn again couple with the laser modes. This provides a locking mechanism that can compensate for dispersion and noise that otherwise prevent equidistance and phase coherence of the modes, respectively. These combs have been primarily observed in interband and quantum cascade lasers, which have a short gain recovery time compared to the cavity round trip time, as a slow gain medium with a long gain recovery time cannot respond efficiently to fast intermode beating and thus results in negligible mode coupling [5]. However, also in interband diode lasers, where the round trip time is typically somewhat smaller than the carrier lifetime of around 1 ns, this effect has been observed in a variety of material systems [2,6,7]. This has been supported by recent theoretical work that suggests that comb formation is principally determined by the interplay of group delay dispersion (GDD) and carrier-induced refractive index changes leading to soliton-like states with a characteristic linear chirp or frequency modulation (FM) in the time domain [8,9].

Optically pumped semiconductor disk lasers or vertical-external-cavity surface-emitting lasers (VECSELs) can be passively mode-locked by use of a semiconductor-saturable-absorber mirror (SESAM) with ultrashort pulse emission down to the sub-100 fs regime [10,11], and even saturable-absorber-free mode locking was discussed [12–15]. Whether this class of lasers supports FM combs similar to their edge-emitting counterparts remains an exciting question to address, as both types of semiconductor lasers differ in some aspects fundamentally. The mode spacing (i.e., free spectral range), which relates directly to the cavity round trip time, is typically an order of magnitude smaller, in the few gigahertz range. This provides a setting where gain recovery time and round trip time are very similar. Also, the spatial hole burning process of a Fabry–Perot cavity, which triggers multi-mode operation in edge-emitting lasers, is absent in VECSELs, as gain-contributing quantum wells (QWs) overlap only at nearly discrete positions in the sample structure with the standing optical field. In addition, the typically centimeter-long external resonator leads to the storage of optical power away from the gain medium.

From a practical point of view, FM combs in VECSELs might be useful for dual-comb spectroscopy with high power per comb line and consequently increased SNR of the measurement, as they are unrivaled in terms of output power among semiconductor lasers, reaching more than 100 W in cw operation [16]. Moreover, advanced III-V semiconductor technology enables great flexibility

with respect to the emission wavelength, ranging from the visible to the mid-infrared [17]. Recently, dual-comb spectroscopy with mode-locked VECSELs has been demonstrated [18]. However, when pushing the pulse length below 100 fs, one observes a dramatic decrease in peak and average power [10], which is possibly caused by fundamental non-equilibrium carrier dynamics such as kinetic hole burning [19]. For increased average power and thus more power per comb line, one would have to increase the pulse length, which means generating chirped pulses for a given bandwidth. A frequency-modulated comb, being the extreme case of a maximally linearly chirped "pulse," would lead to quasi-cw operation and thus highest average power. Remarkably, the existence of FM combs in lasers with fast gain media has been explained with the so-called maximum-emission principle, which states that the phase—amplitude relations of the laser modes will organize in a way to extract the maximum amount of power from the gain medium, which corresponds to the FM state [5].

In this work, we investigate whether FM combs can also be supported in VECSELs by using a coherent beatnote spectroscopy technique, referred to as shifted wave interference transform spectroscopy (SWIFTS) [20]. This allows us to directly measure the intermode phase relation of the laser and assess its phase stability (coherence) over the laser spectrum. Our results show that such comb states can indeed exist in VECSELs, and we discuss its spectral and pump-power dependence.

2. SAMPLE PROPERTIES AND EXPERIMENTAL SETUP

For our investigations, we use a VECSEL gain chip, which has been designed for ultra-short pulse emission and low dispersion. To ensure good crystalline quality, the VECSEL layer structure was grown by metal organic vapor phase epitaxy (MOVPE) using an Aixtron AIX 2600 G3 reactor. The active laser structure consists of four double (GaIn)As QWs with surrounding Ga(AsP) strain-compensating barriers. Each QW pair was placed around a maximum of the longitudinal optical field. The distributed Bragg reflector contains 23.5 (AlGa)AlGaAs mirror pairs with $\lambda/4$ layers for a VECSEL lasing wavelength at 980 nm and additional 13 pairs for a pump wavelength at 808 nm to increase pump efficiency. The final GaAs layer is for phase matching and oxidation protection. The detailed chip structure and layer composition are provided in Supplement 1.

We have performed measurements with a white-light Michelson interferometer to determine the GDD of the sample [21]. As can be seen in Fig. 1(a), the GDD at the lasing frequencies around 303 THz is flat and lower than 500 fs^2 in magnitude as expected for an anti-resonant design, i.e., a design that suppresses a strong microcavity resonance for optimized broadband operation at the cost of reduced gain [22]. Also, the measured dispersion is close to the calculated dispersion obtained by transfer-matrix simulations of the layered chip structure. More details on the dispersion measurement and calculation are provided in Supplement 1.

For laser operation, we mount the chip on a temperature-controlled copper heat sink and construct a simple linear cavity of approximately 9 cm length with an output mirror of 100 mm radius of curvature, minimized dispersion and 0.6% outcoupling rate. The chip is pumped with a fiber-coupled 808 nm multimode diode laser and the pump-spot diameter is adjusted to 200 µm to match the fundamental transverse mode on the chip. The temperature of the heat sink is kept at 18°C throughout all investigations.

To investigate whether the modes of the laser are phase-stable and locked, we use the SWIFTS technique, which resolves the beatnote coherently over the laser spectrum by use of a Michelson interferometer [20]. A sketch of our experimental setup is shown in Fig. 1(b). Part of the laser light is branched off into a fast photodiode while the other part is sent into a home-built Michelson interferometer, the output of which is recorded by another fast photodiode. The signal of both photodiodes is subsequently amplified (by around 25 dB) and mixed down with a local oscillator (LO) with a frequency of 1.58 GHz, which is close to the fundamental beatnote frequency of 1.6 GHz. The downconverted signal of the first photodiode is again amplified (by around 30 dB) to serve as a reference signal for a fast lock-in amplifier (SR844, Stanford Research Systems). The downconverted signal of the fast photodiode after the Michelson interferometer is taken as signal input. Consequently, the lock-in amplifier serves as a phase-sensitive detector, which records two interferograms when the arm of the Michelson interferometer is scanned. One interferogram, $X(\tau)$, corresponds to the in-phase component with respect to the reference signal, and the other interferogram, $Y(\tau)$, corresponds to the quadrature (90° shifted) component. It can be shown (see Supplement 1) that, by Fourier transforming these interferograms with respect to the interferometer delay, the intermode phase difference (SWIFTS phase) can be retrieved by $\arg(X(\omega) - iY(\omega))$, where $X(\omega)$ and $Y(\omega)$ are the complex spectra of $X(\tau)$ and $Y(\tau)$, respectively [2,20]. The magnitude of the combined spectra, the SWIFTS intensity spectrum $|X(\omega) - iY(\omega)|$, indicates over which spectral regions the modes are locked. By comparing this

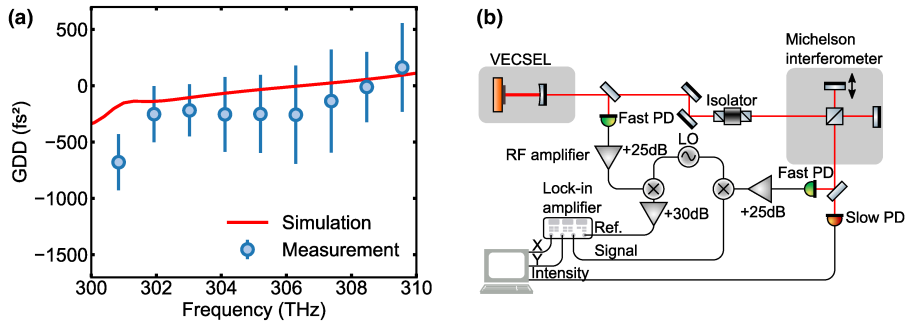

Fig. 1. (a) Measured and simulated group delay dispersion (GDD) of the investigated sample. The error bars indicate the standard deviation when averaging over 997 subsequent measurements/interferograms. (b) Experimental setup used for coherent beatnote spectroscopy. PD, photodiode; LO, local oscillator.

spectrum to the normal intensity spectrum obtained by Fourier transforming the interferogram recorded by a slow photodiode, one can assess which parts of the spectrum are phase coherent, and to what degree. When the shapes of both spectra match exactly, the emission consists of perfectly phase-coherent and equidistant laser modes.

3. EXPERIMENTAL RESULTS

A first indicator of phase locking in a laser is provided by a narrow RF beatnote. Figure 2(a) shows the fundamental RF beatnote measured at 1.6 GHz with a 25 GHz photodiode at an optical pump power of 3.7 W. The 3 dB width of the beatnote is approximately 2.2 kHz. The noise pedestal is nearly 30 dB below the peak. Figure 2(b) displays the envelope of the raw interferograms recorded with the slow photodiode and the SWIFTS setup. The regular intensity interferogram exhibits a maximum at zero delay of the interferometer. The beating on the envelope is caused by the two-color operation of the laser. One notices that the envelope beatings of the intensity interferograms and the SWIFTS interferograms are phase shifted to each other by 180°. This is a consequence of the fact that each lobe (color) exhibits a total intermode phase difference of π [as can be seen in Fig. 2(d)]. A derivation of this relation is provided in Supplement 1. The fact that the laser operates on two spectral lobes is probably a consequence of the anti-resonant design of the gain chip, for which the cavity resonance is designed in a way that there is no strong cavity resonance at one specific wavelength but rather two smaller resonances centered around the maximum material gain (see Supplement 1). In contrast to the intensity interferogram, both SWIFTS interferograms show a characteristic minimum at zero delay. This minimum is attributed to the presence of FM in the laser [3] and can be understood by regarding the intermode beating as complex phasors that cancel each other out when summed up [2]. Finally, Fig. 2(c) shows the retrieved normalized intensity and the two SWIFTS spectra as well as the intermode (SWIFTS) phase for 10 subsequent measurements [Fig. 2(d)]. Interestingly, for the lobe at larger frequencies, the intensity and SWIFTS spectrum match very well, whereas for the lobe at smaller frequencies, the amplitude of the SWIFTS spectrum is considerably smaller than the intensity spectrum and does not span over the whole range towards smaller frequencies. Accordingly, the SWIFTS spectrum is here normalized with respect to the intensity of the higher-frequency lobe. The intermode phase in Fig. 2(d) is well defined wherever the SWIFTS spectrum contains significant intensity. All SWIFTS phase measurements have been aligned with respect to their phase at 303.6 THz. As a result, the phases of the low-frequency lobe will also be aligned, although some phase measurements exhibit an offset of 2π from each other. This is a consequence of the unwrapping procedure and was corrected by shifting the phases at frequencies smaller than 303.3 THz by 2π, so that all phases also match exactly at the low-frequency lobe of the spectrum. Interestingly, while the SWIFTS phases between the lobes are not (well) defined and thus are different for different subsequent measurements, the phase offset between high- and low-frequency lobes is constant for all subsequent measurements, and the total phase difference over both lobes amounts to about 2π as expected for a frequency-modulated comb. As a result of these investigations, we average both the intensity spectrum and SWIFTS (phase) spectra over multiple subsequent measurements in the following investigations. For the SWIFTS phase, we also plot the corresponding standard deviation as error bars to indicate where it is well defined.

To gain further insights into the coherence properties of our laser, we investigate the pump power dependence of the fundamental beatnote, as well as of the intensity and SWIFTS spectra. In Fig. 3(a), the pump-power-dependent evolution of the beatnote at 1.6 GHz is displayed. At 3.2 W pump power, corresponding to an output power of the laser of 111 mW, a detectable but small beatnote close to the noise level is measured. At pump powers ranging from 3.2 to 3.6 W, the beatnote is so small that it cannot be used as a reference for SWIFTS measurements. However, at a pump power of 3.6 W, the beatnote suddenly increases by more than 20 dB in magnitude. Strikingly, this coincides with the separation of the optical spectra in Fig. 3(b) into two lobes. Here, as already observed in Fig. 2(b), the intensity and SWIFTS spectra of the lobe at larger frequencies match perfectly over the pump power range from 3.4 to 4 W corresponding to output powers of 135 to 188 mW. In this range, the lobe at lower frequencies exhibits only partial coherence with nearly no coherence towards the lower frequency side. At a pump power of 4.1 W, the beatnote "explodes" into strong and broad noise pedestals around its peak within the frequency range of

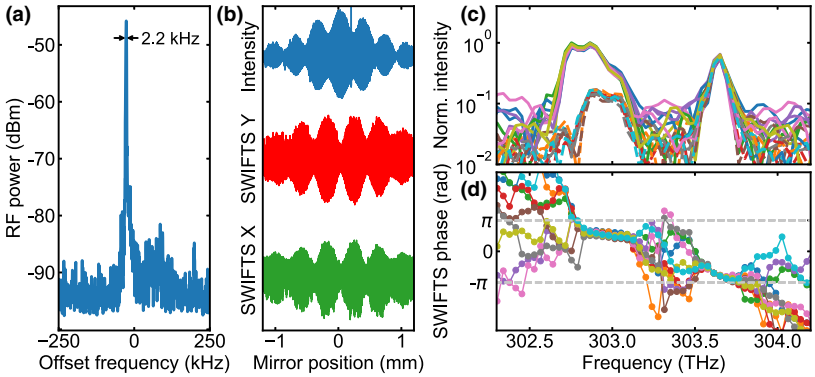

Fig. 2. Coherence characterization of the VECSEL at 3.7 W pump power. (a) Fundamental beatnote at 1.6 GHz recorded with a resolution bandwidth of 1 kHz over a span of 500 kHz. The 3 dB bandwidth is indicated by the arrows. (b) Intensity interferogram recorded with a slow photodiode ("Intensity") and the interferograms of the in-phase ("SWIFTS X") and quadrature component ("SWIFTS Y") of lock-in detection. (c) Magnitude of the Fourier transforms of the intensity interferogram (solid lines) and of the combined SWIFTS interferograms (dashed lines). Ten subsequently recorded measurements are shown. (d) Corresponding frequency-resolved intermode (SWIFTS) phase. The dots indicate the resolution of the measurement and do not represent individual modes.

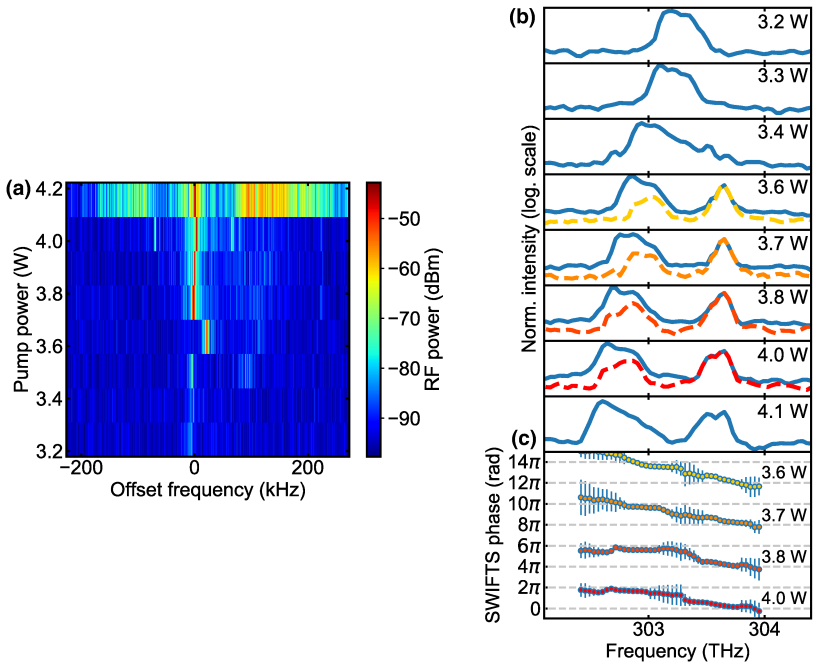

Fig. 3. (a) Pump-power dependence of the beatnote at 1.6 GHz measured with 1 kHz resolution bandwidth and 500 kHz span. (b) Pump-power-dependent intensity spectra (blue solid line) and SWIFTS intensity spectra (dashed line). The respective pump-power value is indicated in each subfigure. All spectra have been obtained by averaging over 10 subsequent measurements. (c) Corresponding SWIFTS phase. The power level is indicated to the right of the phase spectrum. The dots indicate the spectral resolution, and the error bars indicate the standard deviation when averaging over 10 subsequent measurements.

500 kHz. The phase coherence is lost, and the SWIFTS intensity spectrum consequently drops to zero. For larger pump powers, the beatnote remains broad. Thus, no data for pump powers beyond 4.1 W are shown.

All the retrieved intermode (SWIFTS) phases [Fig. 3(c)] show a phase difference of approximately 2π over the total spectrum. Thus, while the phases in-between the lobes are not very well defined and display a large standard deviation when averaging over multiple measurements, the two lobes are not completely decoupled and can still exhibit linearly chirped anti-phase synchronization. This is evidenced by an approximately linear trend of the intermode phase over the laser spectrum and a total phase difference of 2π [2,8,23].

It is worth mentioning that one witnesses here the existence of one higher-order transverse mode with a broad RF line (several tens of kilohertz) in the long-span RF spectrum, as shown in Fig. S3 of Supplement 1 when the photodiode is placed in a way that the contribution from the higher-order transverse mode (TEM_{10}) is detected. Attempts to suppress this mode by reducing the pump spot size on the chip were not successful. In fact, the existence of a higher-order transverse mode seems to coincide with the appearance of a narrow beatnote for the fundamental mode, similar to the behavior observed in Ref. [24]. This might hint to a possible connection between the frequency-modulated comb state we observe here and the self-mode-locking reports for VECSELs, where coherence of the laser emission was evidenced by autocorrelation measurements [14,24]. Nonetheless, we point out that the excellent correspondence of SWIFTS and intensity spectrum for the high-frequency lobe demonstrates that this part of the spectrum must principally consist of phase-locked longitudinal modes of the fundamental mode.

Furthermore, we investigated the effect of suppressing externally the partially incoherent lobe at lower frequencies with an angle-tunable short-pass filter (Semrock TSP01-1116) on the beatnote and SWIFTS interferograms. For a valid comparison, we adjusted the power in front of the photodiode to 2.2 mW for both the investigation with the filter inserted and without a filter (for the measurements in Fig. 2, the power in front of the photodiode was significantly larger). The result is shown in Fig. 4. Without the filter, the fundamental beatnote at 1.59 GHz is below 60 dBm [Fig. 4(a)], and the two SWIFTS interferograms ["X" and "Y" in Fig. 4(b)] show a pronounced minimum at zero delay position. However, when the low-frequency lobe is suppressed with the filter, the beatnote increases by approximately 16 dB, and the SWIFTS interferograms show no minimum at zero delay position anymore. This illustrates nicely the frequency-modulated nature of the laser emission. In the unfiltered case, the phases of the locked longitudinal modes organize in a way to minimize amplitude fluctuations, and therefore, the result is a small beatnote as well as a minimum at zero delay position in the SWIFTS interferograms. Both features result from destructive interference of the intermode beatings. In contrast, when part of the phase-locked laser spectrum is removed by the filter, the remaining intermode beatings will not cancel each other out very well anymore. This explains the strong increase in the magnitude of the beatnote as well as the disappearance of the minima at zero delay position in the SWIFTS interferograms.

The lobe in Fig. 4(f) has a 3 dB width of around 0.13 THz, thus containing more than 82 longitudinal laser modes, which is more than twice the number of modes that have been used in the pioneering first dual-comb spectroscopy experiment with VECSELs [18]. This highlights the importance of our results. Even though not the whole unfiltered laser spectrum is perfectly phase

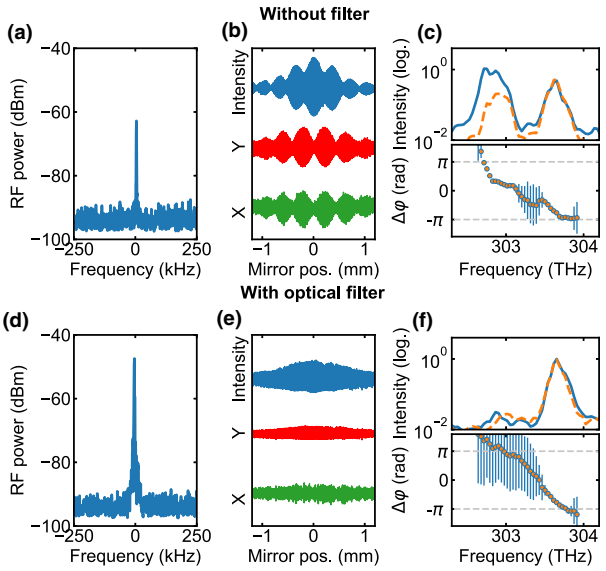

Fig. 4. (a) Fundamental beatnote (measured at 1.59 GHz center frequency with 1 kHz resolution bandwidth and 500 kHz span), (b) intensity and SWIFTS interferograms, and (c) intensity (blue solid line), SWIFTS spectrum (orange dashed line), and SWIFTS phase $\Delta\varphi$ of the unfiltered laser emission at a pump power of 3.2 W (sample spot different from that in Fig. 3 used here). The corresponding measurements with spectral filtering are shown in (d), (e), and (f). For measurement of the fundamental beatnote in (a) and (d), the power in front of the photodiode is adjusted to 2.2 mW in both cases.

locked, a combination of spatial and spectral filtering can render it effectively coherent.

We believe that with a detailed understanding of the locking mechanism, it will be possible in the future to obtain FM combs in VECSELs that are fully coherent over the whole laser spectrum. Then they might provide a very simple and at the same time high-power source for dual-comb spectroscopy. To reach this goal, two open questions need to be addressed in future works: what limits the coherence over a broad spectrum, and what is the optimal amount of GDD in the cavity (see Ref. [8])?

Moreover, FM combs may become a useful alternative to SESAM-mode-locked VECSELs for some applications, particularly in the context of novel material systems targeting new spectral emission wavelengths where SESAM mode locking might be difficult to achieve. An example can be seen in the recently demonstrated type-II VECSELs [25], which have not been SESAM mode locked yet.

4. CONCLUSION

By measuring the intermode phase relation and the phase coherence with the SWIFTS technique, we have demonstrated that a VECSEL can run in a frequency-modulated regime, whereas at the moment, this occurs over a certain part of its spectrum. With an optical filter, the incoherent part can be suppressed, and phase-coherent light is obtained. This establishes optically pumped semiconductor disk lasers as a new platform where the physics of FM combs can be studied. In fact, VECSELs offer unique characteristics such as a very similar gain recovery time and cavity round trip time as well as the absence of spatial hole burning as a driver for multi-mode emission. Given future optimization efforts, it can be anticipated that these comb sources may prove themselves useful for dual-comb spectroscopy in application scenarios where a particular high power per comb line or specific target wavelengths are required.

Funding. Deutsche Forschungsgemeinschaft (DFG RA 2841/1-1, DFG RA 2841/1-3).

Acknowledgment. We thank C. Schindler for expert design of the RF amplifiers and mixers and for useful discussions.

Disclosures. The authors declare no conflict of interests.

Supplemental document. See Supplement 1 for supporting content.

REFERENCES

1. H. A. Haus, "Mode-locking of lasers," IEEE J. Sel. Top. Quantum Electron. **6**, 1173–1185 (2000).
2. J. Hillbrand, D. Auth, M. Piccardo, N. Opacak, G. Strasser, F. Capasso, S. Breuer, and B. Schwarz, "In-phase and anti-phase synchronization in a laser frequency comb," Phys. Rev. Lett. **124**, 023901 (2019).
3. A. Hugi, G. Villares, S. Blaser, H. C. Liu, and J. Faist, "Mid-infrared frequency comb based on a quantum cascade laser," Nature **492**, 229–233 (2012).
4. E. Escoto and G. Steinmeyer, "Pseudo mode-locking," Proc. SPIE **11263**, 1126306 (2020).
5. M. Piccardo, P. Chevalier, B. Schwarz, D. Kazakov, Y. Wang, A. Belyanin, and F. Capasso, "Frequency-modulated combs obey a variational principle," Phys. Rev. Lett. **122**, 253901 (2019).
6. M. W. Day, M. Dong, B. C. Smith, R. C. Owen, G. C. Kerber, T. Ma, H. G. Winful, and S. T. Cundiff, "Simple single-section diode frequency combs," APL Photon. **5**, 121303 (2020).
7. R. Rosales, S. G. Murdoch, R. Watts, K. Merghem, A. Martinez, F. Lelarge, A. Accard, L. P. Barry, and A. Ramdane, "High performance mode locking characteristics of single section quantum dash lasers," Opt. Express **20**, 8649–8657 (2012).
8. N. Opačak and B. Schwarz, "Theory of frequency modulated combs in lasers with spatial hole burning, dispersion and Kerr nonlinearity," Phys. Rev. Lett. **123**, 243902 (2019).
9. D. Burghoff, "Unraveling the origin of frequency modulated combs using active mean-field theory," Optica **7**, 1781–1787 (2020).
10. D. Waldburger, S. M. Link, M. Mangold, C. G. E. Alfieri, E. Gini, M. Golling, B. W. Tilma, and U. Keller, "High-power 100 fs semiconductor disk lasers," Optica **3**, 844–852 (2016).
11. A. Laurain, I. Kilen, J. Hader, A. R. Perez, P. Ludewig, W. Stolz, G. Balakrishnan, S. W. Koch, and J. V. Moloney, "Modeling and experimental realization of modelocked VECSEL producing high power sub-100 fs pulses," Appl. Phys. Lett. **113**, 121113 (2018).
12. L. Kornaszewski, G. Maker, G. P. Malcolm, M. Butkus, E. Rafailov, and C. J. Hamilton, "SESAM-free mode-locked semiconductor disk laser," Laser Photon. Rev. **6**, L20–23 (2012).
13. A. R. Albrecht, Y. Wang, M. Ghasemkhani, D. V. Seletskiy, J. G. Cederberg, and M. Sheik-Bahae, "Exploring ultrafast negative Kerr effect for mode-locking vertical external-cavity surface-emitting lasers," Opt. Express **21**, 28801–28808 (2013).
14. M. Gaafar, P. Richter, H. Keskin, C. Möller, M. Wichmann, W. Stolz, A. Rahimi-Iman, and M. Koch, "Self-mode-locking semiconductor disk laser," Opt. Express **22**, 28390–28399 (2014).
15. M. A. Gaafar, A. Rahimi-Iman, K. A. Fedorova, W. Stolz, E. U. Rafailov, and M. Koch, "Mode-locked semiconductor disk lasers," Adv. Opt. Photon. **8**, 370–400 (2016).
16. B. Heinen, T.-L. Wang, M. Sparenberg, A. Weber, B. Kunert, J. Hader, S. W. Koch, J. V. Moloney, M. Koch, and W. Stolz, "106 W continuous-wave output power from vertical-external-cavity surface-emitting laser," Electron. Lett. **48**, 516–517 (2012).
17. A. Rahimi-Iman, "Recent advances in VECSELs," J. Opt. **18**, 093003 (2016).
18. S. M. Link, D. J. H. C. Maas, D. Waldburger, and U. Keller, "Dual-comb spectroscopy of water vapor with a free-running semiconductor disk laser," Science **356**, 1164–1168 (2017).
19. I. Kilen, J. Hader, J. V. Moloney, and S. W. Koch, "Ultrafast nonequilibrium carrier dynamics in semiconductor laser mode locking," Optica **1**, 192–197 (2014).

20. D. Burghoff, Y. Yang, D. J. Hayton, J.-R. Gao, J. L. Reno, and Q. Hu, "Evaluating the coherence and time-domain profile of quantum cascade laser frequency combs," Opt. Express **23**, 1190–1202 (2015).
21. A. Gosteva, M. Haiml, R. Paschotta, and U. Keller, "Noise-related resolution limit of dispersion measurements with white-light interferometers," J. Opt. Soc. Am. B **22**, 1868–1874 (2005).
22. A. C. Tropper and S. Hoogland, "Extended cavity surface-emitting semiconductor lasers," Prog. Quantum Electron. **30**, 1–43 (2006).
23. M. Singleton, P. Jouy, M. Beck, and J. Faist, "Evidence of linear chirp in mid-infrared quantum cascade lasers," Optica **5**, 948–953 (2018).
24. C. H. Tsou, H. C. Liang, C. P. Wen, K. W. Su, K. F. Huang, and Y. F. Chen, "Exploring the influence of high order transverse modes on the temporal dynamics in an optically pumped mode-locked semiconductor disk laser," Opt. Express **23**, 16339–16347 (2015).
25. C. Möller, C. Fuchs, C. Berger, A. R. Perez, M. Koch, J. Hader, J. V. Moloney, S. W. Koch, and W. Stolz, "Type-II vertical-external-cavity surface-emitting laser with Watt level output powers at 1. 2 μm," Appl. Phys. Lett. **108**, 071102 (2016).

Supplemental document accompanying submission to *Optica*

Title: Frequency-modulated comb in a VECSEL

Authors: Christian Kriso, Avijit Barua, Obaid Mohiuddin, Christoph Möller, ANTJE PEREZ, Wolfgang Stolz, Martin Koch, Arash Rahimi-Iman

Submitted: 18.12.2020 09:25:54

Signatures of a frequency-modulated comb in a VECSEL: supplemental document

1. SAMPLE STRUCTURE

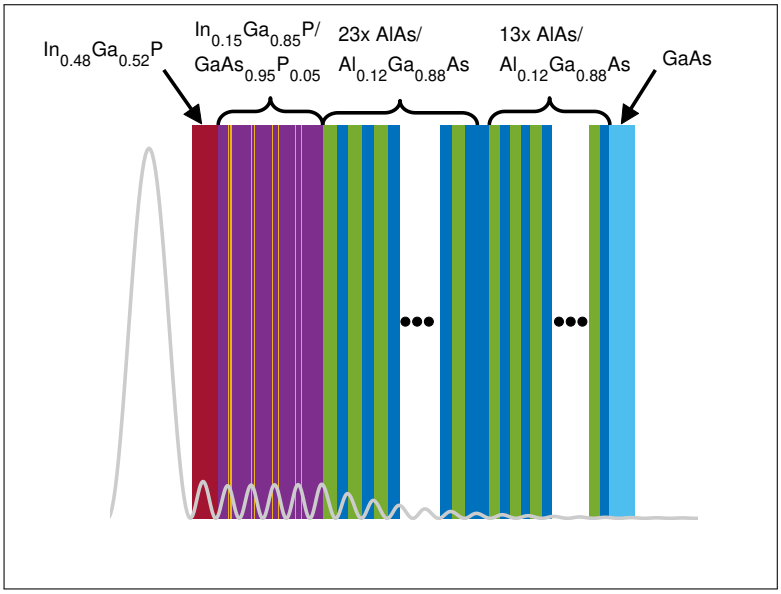

Fig. S1. Sample structure and normalized standing electric field intensity at 303.65 THz (987.3 nm).

2. DISPERSION MEASUREMENT

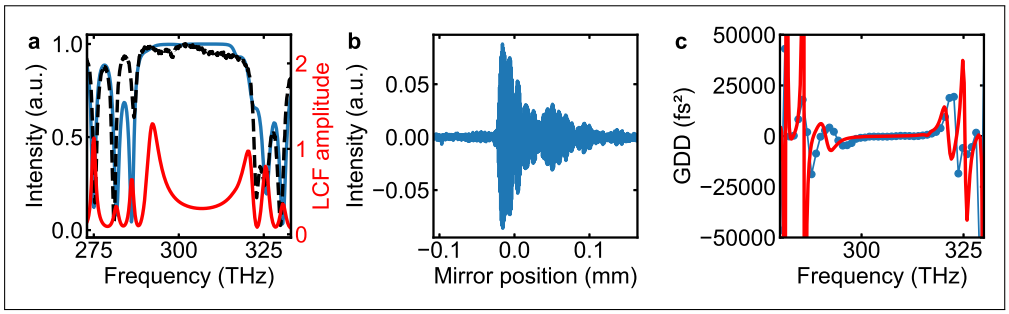

Fig. S2. (a) Calculated (blue solid line) and measured (black dashed line) reflectivity spectrum of the studied VECSEL chip. Additionally, the calculated longitudinal confinement factor (LCF) of the chip's microcavity is shown (red solid line). (b) Exemplary white-light interferogram of the probed VECSEL chip. (c) Measured (blue dots) and calculated (red line) group delay dispersion (GDD).

For the measurement of the group delay dispersion (GDD) of the unpumped VECSEL chip, a home-built white-light interferometer was used, similar to the ones in Refs. [1] and [2]. A He-Ne

laser was used as position reference of the moving mirror, mounted on a mechanical shaker, and spatially overlapped with the white-light from an halogen lamp. After the interferometer, the He-Ne laser and the white light are separated by appropriate dichroic mirrors and recorded each with a photodiode. A fast digitizer card records around 1000 interferograms while the shaker is oscillating. An examplary interferogram is shown in Fig. S2(b). The mirror position has been obtained by taking the zero-crossings of the He-Ne laser interferogram as position reference. The GDD is then obtained by Fourier-transforming it with respect to the delay $\tau = \Delta x/c$, with Δx the mirror position and c the speed of light. The phase of the obtained spectrum is then twice numerically derived with respect to the angular frequency ω which provides the GDD. For averaging, multiple interferograms are interpolated over the same mirror position/delay grid before Fourier-transforming each of them and subsequently averaging the calculated GDD. Finally, the GDD of the balanced interferometer with two metal mirrors (and the sample removed) is recorded to account for the interferometer's transfer function. Figure S2(c) shows the measured dispersion of the sample obtained by averaging over 997 interferograms (blue dots) and shows good correspondence to the calculated dispersion. The calculated dispersion has been obtained by calculating the complex reflectivity spectrum of the sample structure with the transfer matrix formalism detailed in [3] and obtaining the second derivative of the electric field's phase with respect to ω. The calculated and measured reflectivity spectra show good correspondence (see Fig. S2(a)). Also shown in Fig. S2(a) is the calculated longitudinal confinement factor (LCF) that characterizes the overlap of the intensity of the electric field with the quantum wells (see Ref. [3]). It is at its minimum in the spectral region where the laser operates, which yields the desired flat and low dispersion, but reduces the achievable maximum output power of the sample.

3. SWIFTS MEASUREMENT

To understand the working principle of the SWIFTS measurement (see also Refs. [4, 5]), we write the electric field of the laser emission as

$$E(t) = \sum_n E_n e^{i(\omega_n t + \varphi_n)} + c.c., \tag{S1}$$

where E_n is the amplitude, φ_n the phase and ω_n the oscillation frequency of an individual mode n. When detecting this field with a fast photodetector after a Michelson interferometer, which introduces a delay τ in one of its arms, the detected signal becomes

$$\begin{aligned} I(t,\tau) = \frac{1}{2}(E(t)+E(t-\tau))^2 = \frac{1}{2}\sum_{n,m}(E_n E_m e^{i((\omega_n-\omega_m)t+\varphi_n-\varphi_m)} \\ + E_n E_m e^{i((\omega_n-\omega_m)(t-\tau)+\varphi_n-\varphi_m)} + 2E_n E_m e^{i((\omega_n-\omega_m)t+\omega_m\tau+\varphi_n-\varphi_m)}) + c.c., \end{aligned} \tag{S2}$$

where we have omitted any terms with an $e^{i(\omega_n+\omega_m)t}$-dependency, which will not be detected by a photodiode. Equation S2 can be rewritten as

$$I(t,\tau) = \frac{1}{2}\sum_{n,m} E_n E_m e^{i((\omega_n-\omega_m)t+\varphi_n-\varphi_m)}(1 + e^{i(\omega_n-\omega_m)\tau} + 2e^{i\omega_m\tau}) + c.c.. \tag{S3}$$

A slow photodiode will only detect terms with $n = m$, which leads to

$$I(\tau) = \sum_n E_n^2(1 + e^{i\omega_n\tau}) + c.c.. \tag{S4}$$

This interferogram provides the optical intensity spectrum $I(\omega)$ of the laser when Fourier-transformed.

In SWIFTS, the detected signal in Eq. S3 is mixed with an in-phase ($\cos(\omega_0 t)$) and a quadrature signal ($\sin(\omega_0 t)$) at a frequency ω_0. This operation, which is performed by the lock-in amplifier, leads to two signals,

$$X(t,\tau) = \frac{1}{4}\sum_{n,m} E_n E_m (e^{i((\omega_n-\omega_m-\omega_0)t+\varphi_n-\varphi_m)} + e^{i((\omega_n-\omega_m+\omega_0)t+\varphi_n-\varphi_m)})(...) + c.c., \tag{S5a}$$

$$Y(t,\tau) = \frac{i}{4}\sum_{n,m} E_n E_m (e^{i((\omega_n-\omega_m-\omega_0)t+\varphi_n-\varphi_m)} - e^{i((\omega_n-\omega_m+\omega_0)t+\varphi_n-\varphi_m)})(...) + c.c.. \tag{S5b}$$

Only variations in the order of the time constant of the lock-in amplifier will be detected, which means that only $\omega_0 = \omega_n - \omega_m$ will result in a non-zero signal. For the measurement of the phase and coherence of two adjacent modes, $\omega_0 = \omega_{m+1} - \omega_m$ is chosen. Note, however, that the time constant does not set the condition for the equidistance of two laser lines but just blocks lines other than nearest-neighbor in the lock-in detection. The precision of the equidistance assessment is instead determined by the inverse of the total measurement time of the interferogram (around 1 minute in our case) as pointed out in Ref. [5]. Remarkably, this means that the equidistance measurement exhibits sub-Hz precision. In the self-referenced scheme, as done in this work, the frequency ω_0 of the reference signals is directly obtained from the fundamental beatnote of the laser, measured before the Michelson interferometer with another fast photodiode. Note that, as in our case the bandwidth of the lock-in amplifier is lower (200 MHz) than the fundamental repetition rate of the laser (1.6 GHz), we use a local oscillator and RF mixers to down-convert the signals from the fast photodiodes.
After the lock-in detection, Eqs. S5 thus become

$$X(\tau) = \frac{1}{4}\sum_m E_{m+1}E_m e^{i(\varphi_{m+1}-\varphi_m)}(...) + c.c., \tag{S6a}$$

$$Y(\tau) = \frac{i}{4}\sum_m E_{m+1}E_m e^{i(\varphi_{m+1}-\varphi_m)}(...) + c.c.. \tag{S6b}$$

The two SWIFTS interferograms (in-phase and quadrature) can be combined in one complex interferogram,

$$X(\tau) - iY(\tau) = \frac{1}{2}\sum_m E_{m+1}E_m e^{i(\varphi_{m+1}-\varphi_m)}(1 + e^{i\omega_0\tau} + 2e^{i\omega_m\tau}). \tag{S7}$$

One can see that the product of two adjacent mode amplitudes and their phase difference will be resolved over the optical spectrum when the interferograms are Fourier-transformed with respect to the delay τ. Now it is obvious that $\arg(X(\omega) - iY(\omega))$ will provide the intermode phase $\varphi_{m+1} - \varphi_m$. However, the contribution of two adjacent modes to the SWIFTS spectrum $|X(\omega) - iY(\omega)|$ will disappear when their phases fluctuate over time scales of the total measurement time. Thus, the comparison of $|X(\omega) - iY(\omega)|$ with the intensity spectrum $I(\omega)$ provides a measure of coherence (i.e. phase stability) of the laser.

Equations S4 and S7 (or S6) can be used to show that, if for a phase-locked two-color spectrum the intermode phase difference of both colors amounts to π, respectively, with no phase-offset between both colors, the beating of the SWIFTS envelope will be shifted by 180° with respect to the beating envelope of the intensity interferogram. To show this, we assume an idealized spectrum of two lobes of the same width and amplitude, separated by a frequency difference $\Delta\omega$. The electric field of such a spectrum can then be written as

$$E(t) = \sum_n^{N/2} E_0(e^{i(\omega_n t+\varphi_n)} + e^{i((\omega_n+\Delta\omega)t+\varphi_{n+N/2})}) + c.c., \tag{S8}$$

where N is the total number of modes (each lobe contains $N/2$ modes) and all mode amplitudes have been assumed constant (i.e. $E_n = E_0$). With the above-mentioned assumption, the intermode phase is $\Delta\varphi_n = \varphi_{n+1} - \varphi_n = \frac{2\pi}{N}n$, which means $\Delta\varphi_{n+N/2} = \Delta\varphi_n + \pi$.
Consequently, the intensity interferogram in Eq. S4 becomes

$$I(\tau) = \sum_n^{N/2} E_0^2(1 + e^{i\omega_n\tau} + 1 + e^{i(\omega_n+\Delta\omega)\tau}) + c.c. = \sum_n^{N/2} E_0^2(2 + e^{i\omega_n\tau}\underbrace{(1 + e^{i\Delta\omega\tau})}_{\textit{Envelope beating}}) + c.c., \tag{S9}$$

where the term $(1 + e^{i\Delta\omega\tau})$ describes the envelope beating of the interferogram.

Now we take the SWIFTS interferogram in Eq. S7 (we use the complex interferogram and complex electric field here for simpler expressions) and apply the assumptions for the electric

field which leads to

$$X(\tau) - iY(\tau) = \frac{1}{2}\sum_{n}^{N/2} E_0^2(e^{i\Delta\varphi_n}(1 + e^{i\omega_0\tau} + 2e^{i\omega_n\tau}) + e^{i\Delta\varphi_{n+N/2}}(1 + e^{i\omega_0\tau} + 2e^{i(\omega_n+\Delta\omega)\tau})) =$$

$$\frac{1}{2}\sum_{n}^{N/2} E_0^2((e^{i\Delta\varphi_n} + e^{i(\Delta\varphi_n+\pi)})(1 + e^{i\omega_0\tau}) + 2e^{i(\omega_n\tau+\Delta\varphi_n)}\underbrace{(1 + e^{i(\Delta\omega\tau+\pi)})}_{\textit{Envelope beating}}). \quad \text{(S10)}$$

Here, the envelope beating term is $(1 + e^{i(\Delta\omega\tau+\pi)})$, which is phase-shifted by π compared to the beating term of the intensity interferogram. This explains why the envelope beating that we observe in the measured intensity and SWIFTS interferograms is phase-shifted by 180°.

4. LONG-SPAN RF SPECTRA AND HIGHER-ORDER TRANSVERSE MODE

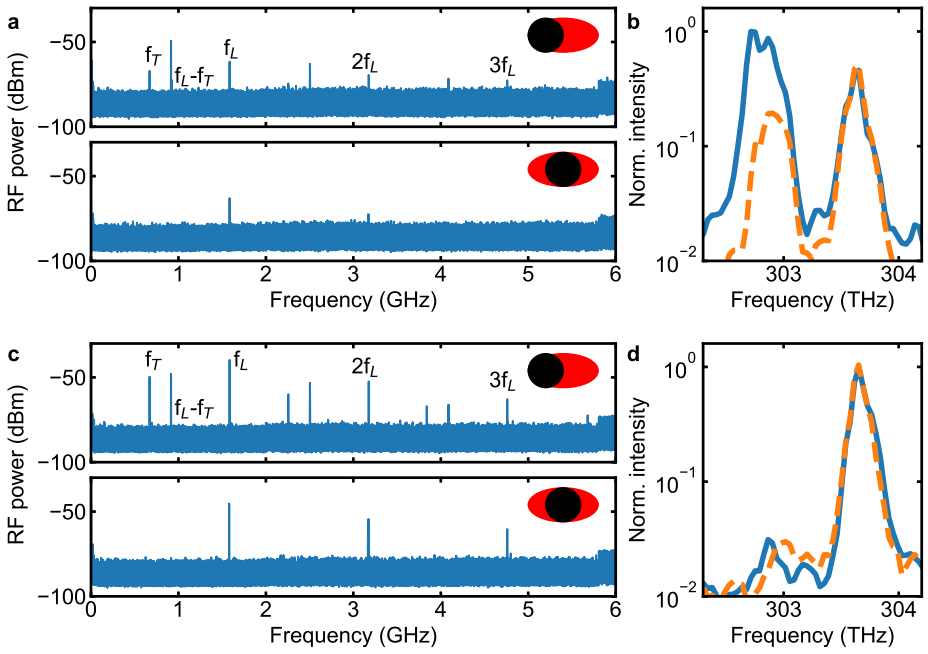

Fig. S3. Effect of spectral and spatial filtering on the long-span RF spectrum at a pump power of 3.2 W. The laser operation point is the same as in Fig. 4 of the main text, the power in front of the photodiode is adjusted to 2.2 mW in the filtered and unfiltered case. (a) RF spectrum (resolution bandwidth 100 kHz) of unfiltered laser emission for two positions of the photodiode with respect to the optical beam, indicated by the sketch in the upper right corner. The red ellipse visualizes the laser beam and the black circle the photodiode. (b) Intensity (blue solid line) and SWIFTS spectrum (orange dashed line) of unfiltered laser emission. (c) RF spectrum (resolution bandwidth 100 kHz) of filtered laser emission for two positions of the photodiode. (d) Intensity (blue solid line) and SWIFTS spectrum (orange dashed line) of filtered laser emission.

Here, we discuss the effect on the long-span RF spectra of filtering the lower lobe of the laser spectrum and show the high-resolution RF spectra of the beatnote of the transverse mode and its mixing product with the longitudinal mode (in the filtered and unfiltered case). These data are complementary to the data in Fig. 4 of the main text (i.e. taken at the same operation point of the laser at 3.2 W pump power). In Fig. S3(a), the long-span RF spectra of the unfiltered laser emission is shown, once for the case when the photodiode mainly captures the higher-order transverse mode (upper graph) and once when the photodiode is positioned in a way to only capture the contribution of the fundamental longitudinal mode (lower graph). The position of

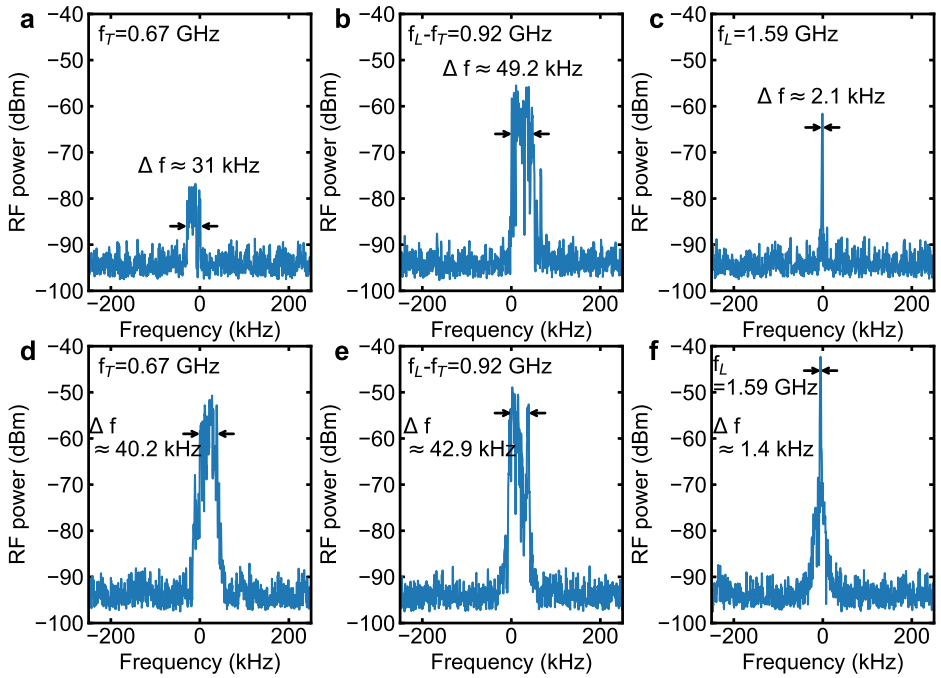

Fig. S4. High-resolution RF beatnotes (1 kHz resolution bandwidth and 500 kHz span) of the transverse mode at frequency f_T=0.67 GHz ((a), (d)), the longitudinal mode at f_L=1.59 GHz ((c), (f)) and the mixing product of the two at f_L-f_T=0.92 GHz ((b), (d)). The 3-dB bandwidth Δf is indicated in each figure with arrows. (a),(b),(c) correspond to the unfiltered case as shown in Fig.S3(a) and (d),(e),(f) correspond to the filtered case as shown in Fig. S3(c).

the photodiode with respect to the TEM_{01} beamprofile is sketched in the corresponding graphs. In the former case, the mixing product at frequency $f_L - f_T$=0.92 GHz dominates the spectrum, in the latter case, no contribution from the higher-order modes can be seen. When the incoherent, low-frequency lobe is suppressed with the short-pass filter, one observes a significant increase of the beatnote, both, for the longitudinal mode and the transverse mode, while the mixing product maintains roughly the same magnitude. Here, the power in front of the photodiode has been adjusted to 2.2 mW in the filtered and unfiltered case to assure comparability. Now, the longitudinal mode exhibits the largest magnitude. Similarly to the unfiltered case, any sign of the higher-order mode disappears when the photodiode is moved to the center of the beam. It is somewhat surprising that also the transverse mode beating increases in magnitude when using the filter. This might be attributed to the fact that it also experiences some phase-locking and anti-phase synchronization (although not as strong as the longitudinal mode). When the spectrum is filtered, the anti-phase synchronization might be partially eliminated and thus the beatnote increases due to increased constructive interference of the intermode beatings. While the SWIFTS measurements did not work with the transverse mode, the width of its beatnote (shown in Fig. S4(a) and(d) for the unfiltered and filtered case, respectively) is 30-40 kHz and thus still narrower than the beatnote of the longitudinal mode when it becomes incoherent for high pump powers (as shown in Fig. 3 of the main text, with a width of hundreds of kHz). Such situation might indicate some weak phase-locking of the transverse mode. Thus, it is difficult to assess whether filtering the low-frequency lobe removes the relative contribution of the higher-order transverse mode from the laser emission just by looking at the relative difference in magnitude of the RF lines. However, the good correspondence of the SWIFTS and optical spectrum for the high-frequency lobe indicates that this is the case, as contributions from the higher-order transverse mode will not be accounted in the SWIFTS measurement that uses the longitudinal mode as reference.

REFERENCES

1. S. Diddams and J.-C. Diels, "Dispersion measurements with white-light interferometry," J. Opt. Soc. Am. B **13**, 1120 (1996).
2. A. Gosteva, M. Haiml, R. Paschotta, and U. Keller, "Noise-related resolution limit of dispersion measurements with white-light interferometers," J. Opt. Soc. Am. B **22**, 1868 (2005).
3. A. C. Tropper and S. Hoogland, "Extended cavity surface-emitting semiconductor lasers," Prog. Quantum Electron. **30**, 1–43 (2006).
4. D. Burghoff, Y. Yang, D. J. Hayton, J.-R. Gao, J. L. Reno, and Q. Hu, "Evaluating the coherence and time-domain profile of quantum cascade laser frequency combs," Opt. Express **23**, 1190 (2015).
5. D. Burghoff, "Some notes on Shifted Wave Interference Fourier Transform Spectroscopy (SWIFTS), 10.13140/RG.2.2.30934.70721," (2018).

Scientific career

Diese Seite enthält persönliche Daten und ist deshalb nicht Bestandteil der Online-Veröffentlichung.

Acknowledgements

First, I would like to thank Prof. Dr. Martin Koch for accepting me as a PhD student in his group, his continuous support, and for sharing advice usually by means of anecdotes from his own scientific career.

I thank Prof. Dr. Wolfgang Stolz for generously providing us with multiple excellent VECSEL chips and for agreeing to be second examiner. Furthermore, I thank Prof. Dr. Stephan Koch and Prof. Dr. Martin Hofmann for joining the examination committee.

I thank Dr. Arash Rahimi-Iman for the many years of fruitful collaboration and supervision as well as the extraordinary level of trust in me, exemplified by employing me on his first own project and giving me nearly complete freedom in the way I do research and the topics I work on. I am particularly grateful for his relentless efforts to obtain funding which resulted in a second funding period of the VECSEL project that allowed me to explore some more projects of my interest and to finish my PhD without strong time constraints.

When I started in Marburg, Christoph Möller, Fan Zhang, Sascha Kress and Stefan Kefer introduced me to the VECSEL activities in Marburg, for which I want to thank them.

None of the work in this thesis would have been possible without the collaborators who provided various kind of samples. In this respect, I thank Roman Bek and Marius Großmann from the Jetter/Michler group at the University of Stuttgart, Antje Ruiz-Perez und Prof. Wolfgang Stolz from NAsPIII/V GmbH, Tobias Haeger and Prof. Thomas Riedl from the University of Wuppertal as well as Alex Albrecht and Prof. Mansoor Sheik-Bahae from the University of New Mexico for samples, discussions, and support.

I would like to thank my students Mohib Alvi, Tasnim Munshi, Obaid Mohiuddin and Avijit Barua for sharing the enthusiasm for our research, their hard work in the lab and their questions that challenged me to think deeper about some topics. I also thank the other members and visitors of the VECSEL group over the past years, Siming Wang, Stefan Mettler, Tianyuan Cao, Pi-Hui Tuan, Ming Gao, Heyang Gouyu and Ksenia Fedorova for creating a friendly and international atmosphere.

Furthermore, I gratefully acknowledge all the other (PhD) students and Postdocs at Renthof (and Lahnberge) for support and discussions, among them Maximilian Schneider, Hilary Masenda, Marina Gerhard, Philipp Richter, Jochen Taiber, Jan Ornik, Manan Shah, Quyet Ngo, Chirag Palekar, Shachi Machar, Mohammed Aly Nouh, Arslan Usman and many more. Particular thanks goes to those who joined regularly for lunch in Mensa when it was still possible. I also thank all those, who joined me for

various outdoor activities and hikes, particularly Manan Shah for becoming my most frequent hiking buddy.

I particularly thank Maximilian Schneider for sharing equipment as well as his extensive experience and knowledge about everything. I thank Marina Gerhard for providing her LaTeX thesis template. I also thank the Heimbrodt as well as the Quantum Quaos group for lending a lot of equipment for my experiments.

I thank Markus Stein for spending two strenuous measurement weeks with me in the amplifier lab, from which I learnt quite a bit more about experimental physics.

I am extremely grateful to Prof. David Hagan and Prof. Eric van Stryland for welcoming me into their group at CREOL. The visit at CREOL was certainly the highlight of my PhD and I greatly enjoyed the time there. I was amazed by the friendliness and helpfulness of all the group members, Sepehr, Sanaz, Natalia, Nick, Scott, Wilbur, Salimeh, Leo and MJ. I not only learnt a lot about nonlinear optics but also about how to do research in a more rigorous and high-quality manner. Furthermore, I thank Bing for driving me around in Orlando and joining me on a road trip through South Florida.

I thank Gerson Mette and Tim Bergmeier for their excellent support with their nice laser system, which allowed me to finally conduct the beam deflection measurements of a VECSEL.

I thank Maya Strobel (and also Anne Ehlers) for taking care of all the administrative issues and purchases. With our large group, this is quite a challenge, but still everything runs smoothly thanks to her.

I thank Rüdiger Rink for help with mechanical constructions and all kind of other problems that one might encounter in an experimental physics lab. His critical questions on every project are key for a solution that nearly always works out very well.

I also thankfully acknowledge the whole team of the electronics workshop for their quick and excellent support with fixing all kind of broken equipment and coming up with brilliant solutions for every problem that can be tackled by electronics. Particularly, I would like to thank Carsten Schindler for constructing the RF amplifiers and mixers, that were essential for the SWIFTS project, and for various discussions about RF electronics and measurements.

It became my hobby and I greatly enjoyed attending various lectures on advanced theoretical physics in Marburg. Therefore, I thank Florian Gebhard, Stephan Koch, Reinhard Noack, Salvatore Manmana and Ermin Malic for their inspiring lectures which spurred my interest in quantum (many-body) physics. I am confident that the acquired knowledge will prove useful in my future research activities.

While research filled a big part of my time in Marburg, I also want to acknowledge those people outside of the lab that made my time here enjoyable. Particularly, I thank everyone at Christliche Gemeinde Marburg for their encouragement, hospitality, and time spent together. The worship and teachings on sunday and the discussions in the bible study group provided a valuable balance to my research activities and helped setting my priorities right. Indeed, while the pursuit of scientific discovery is a

fascinating endeavor, which I am very happy to participate in, it can neither provide ultimate meaning nor a perspective beyond this life. This is what I find in the good news of the bible: “For God so loved the world that he gave his one and only Son, that whoever believes in him shall not perish but have eternal life” (John 3,16).

Finally, I thank my family, particularly my parents, for their support during all stages of my life.